Implicit deformable models for biomedical image segmentation.

Yeo, Si Yong

Yeo, Si Yong (2011) *Implicit deformable models for biomedical image segmentation..* thesis, Swansea University.
http://cronfa.swan.ac.uk/Record/cronfa42416

Implicit Deformable Models for Biomedical Image Segmentation

Si Yong Yeo

A thesis submitted to the College of Engineering
in partial fulfillment of the requirements for
the degree of Doctor of Philosohpy
Swansea University
May 2011

Civil & Computational Engineering Centre
College of Engineering
Swansea University

Swansea University
Prifysgol Abertawe

Abstract

In this thesis, new methods for the efficient segmentation of images are presented. The proposed methods are based on the deformable model approach, and can be used efficiently in the segmentation of complex geometries from various imaging modalities.

A novel deformable model that is based on a geometrically induced external force field which can be conveniently generalized to arbitrary dimensions is presented. This external force field is based on hypothesized interactions between the relative geometries of the deformable model and the object boundary characterized by image gradient. The evolution of the deformable model is solved using the level set method so that topological changes are handled automatically. The relative geometrical configurations between the deformable model and the object boundaries contributes to a dynamic vector force field that changes accordingly as the deformable model evolves. The geometrically induced dynamic interaction force has been shown to greatly improve the deformable model performance in acquiring complex geometries and highly concave boundaries, and give the deformable model a high invariance in initialization configurations. The voxel interactions across the whole image domain provides a global view of the object boundary representation, giving the external force a long attraction range. The bidirectionality of the external force field allows the new deformable model to deal with arbitrary cross-boundary initializations, and facilitates the handling of weak edges and broken boundaries. In addition, it is shown that by enhancing the geometrical interaction field with a nonlocal edge-preserving algorithm, the new deformable model can effectively overcome image noise. A comparative study on the segmentation of various geometries with different topologies from both synthetic and real images is provided, and the proposed method is shown to achieve significant improvements against several existing techniques.

A robust framework for the segmentation of vascular geometries is described. In particular, the framework consists of image denoising, optimal object edge representation, and segmentation using implicit deformable model. The image denoising is based on vessel enhancing diffusion which can be used to smooth out image noise and enhance the vessel structures. The image object boundaries are derived using an edge detection technique which can produce object edges of single pixel width. The image edge information is then used to derive the geometric interaction field for optimal object edge representation. The vascular geometries are segmented using an implict deformable model. A region constraint is added to the deformable model which allows it to easily get around calcified regions and propagate across the vessels to segment the structures efficiently. The presented framework is applied in the accurate segmentation of carotid geometries from medical images.

A new segmentation model with statistical shape prior using a variational approach is also presented in this thesis. The proposed model consists of an image attraction force that propagates contours towards image object boundaries, and a global shape force that attracts the model towards similar shapes in the statistical shape distribution. The image attraction force is derived from gradient vector interactions across the whole image domain, which makes the model more robust to image noise, weak edges and initializations. The statistical shape information is incorporated using kernel density estimation, which allows the shape prior model to handle arbitrary shape variations. It is shown that the proposed model with shape prior can be used to segment object shapes from images efficiently.

Acknowledgements

I would like to thank my advisors, Professor P. Nithiarasu and Dr. I. Sazonov from the School of Engineering for their guidance. Professor Nithiarasu is very knowledgeable in the field of computational modelling and his advices on the areas of numerical methods and bioengineering have been very helpful for the various projects. Dr. Sazonov has been very helpful and his advices on geometric modelling and mathematical formulations have been important in the various projects. I would also like to thank the co-advisor, Dr. X. Xie from the Department of Computer Science. His expertise in the field of image analysis and computer vision, and his advices on image processing and geometric modelling have been very useful. The interactions with my advisors have greatly strengthened my mathematical knowledge and it has been enjoyable doing research with them.

Most importantly, I would like to express my gratitude to my lovely wife and children for their love and support.

Contents

List of Tables

List of Figures

Chapter 1

Introduction

Image segmentation is one of the most important areas in image processing and computer vision. The segmentation of an image can be defined as the partitioning of the image domain Ω into a set of regions $S_i \subset \Omega$ as

$$\Omega = \bigcup_{i}^{n} S_i \tag{1.1}$$

where $S_i \cap S_j = \emptyset$ for $i \neq j$. In general, segmentation is used to extract regions which correspond to objects of interest in the image. The regions of interest can be extracted based on characteristics such as intensity, texture, colour and various information derived from the image.

In recent years, computerized image segmentation has shown to be increasingly important in the area of medical imaging. The accurate delineation of geometries from medical images can allow scientists to visualize and interact with the extracted geometries, and better understand the complex physiological functions of the anatomical structures. Various image segmentation methods have been applied for the visualization, inspection and analysis of anatomical structures from medical images. They have become a useful tool for the quantification of tissue volume, diagnosis of pathologies, surgical planning and biomedical modelling.

This thesis will focus on the formulation of new methods for the robust segmentation of biomedical images. In particular, the proposed methods are based on deformable models, which can be used to extract complex geometries from the images efficiently.

1.1 Challenges in Medical Image Segmentation

Shape segmentation from image data has an important role in applications such as medical image analysis. The segmentation of medical images is an intricate process due to the complexity and variability of anatomical shapes, and the sheer size and quality of image datasets. Medical images are often affected by image noise, sampling artifacts and spatial aliasing, which may cause the boundaries of structures to be indistinct. There are also regions in the image in which multiple tissue types contribute to the intensity of a single pixel or voxel, causing diffused object edges. Another difficulty in delineating structures from medical images is the intensity inhomogeneities that may occur in tissue belonging to the same class or anatomical structure.

There have been applications of simple techniques such as thresholding and region growing in the extraction of 3D objects from volumetric images [2,3]. However, these techniques are very sensitive to noise and intensity inhomogeneities which exist in real images, and often produce leakages and regions which are not contiguous. Statistical approaches [4,5] are also used to identify different tissue structures from medical images. It usually involves manual interaction to segment images in order to obtain a sufficiently large set of training samples. Such strategies are often restricted to problems where there is sufficient prior knowledge about the shape or appearance variations of the relevant structures. Also, the use of the same training set for a large number of image scans may lead to biased results that do not take sufficient consideration of the variability within individuals. Atlas based approaches perform segmentation based on image registration techniques [6], whereby an image can be segmented by finding a transformation that maps a template image to the target image. It is however generally difficult for atlas based techniques to accurately extract complex geometries such as those from volumetric medical images due to the variability of anatomical structures.

Another class of segmentation methods partitions an image into different regions based on energy minimization. These energy based segmentation methods can usually be distinguished as combinatorial methods and variational methods. Graph based approaches [7–9] which are based on combinatorial optimizations can be used to minimize a cost function defined on a discrete set of variables. In this approach, a graph is composed of vertices representing image pixels or voxels, and edges that connect the vertices. The graph edges are assigned some non-negative weights or costs, and a cut is a subset of edges that partition the vertices into disjoint sets. The cost function which can consist of boundary and regional information has to be well defined for graph cuts to provide a globally optimal solution. In addition, the discrete representation of the graphs may produce geometric artifacts, and the algorithm such as [7, 10] has a bias towards cuts with short boundaries.

Deformable models can be an effective alternative approach. They are usually based on a variational framework to minimize an energy functional defined on a continuous contour or surface. They have the ability to adapt to complex shape variations and to incorporate priors to regularize segmentation. They have been widely used in applications such as shape extraction [11–14] and object tracking [15–18]. In these models, curves or surfaces evolve under the influence of both internal and external forces to extract the image object boundaries. Explicit models [19] represent contours and surfaces in their parametric form during deformation. This allows explicit models to track the points on the curves and surfaces across time, and is well suited for real-time applications due to smaller CPU-time requirement. However, explicit models generally have difficulties in dealing with topological changes due to the parameterization of the curves and surfaces. McInerney and Terzopoulos [20] designed topology adaptive, explicit deformable models to handle topological changes that often exist in medical image volumes. This explicit model requires a periodic reparameterization mechanism to deal with complex shapes and changes in topology. This technique however works well only when the model is required to inflate or deflate everywhere, which considerably limits its applications. Several authors [21–23] have also come up with different techniques to handle topological changes. However, these approaches usually involve a set of heuristic algorithms to detect self-intersections and handle splitting and merging of the deforming grid, which can be computationally expensive. Also, these strategies may not work well on structures that consist of complex topologies. Implicit deformable models [11,12] based on the theory of curve evolution and the level set method [24, 25] are introduced to address some of these limitations. In these approaches, the evolution of curves and surfaces are represented implicitly as a level set of a higher-dimensional scalar function and the deformation of the model is based on geometric measures such as the unit normal and curvature. Thus the evolution is independent of the parameterization, and topological changes such as splitting and merging can be handled automatically. In recent years, implicit deformable models have been widely applied in the segmentation of anatomical structures from 3D medical images [26–28].

This thesis presents new methods based on implicit deformable models for image segmentation. It is shown that the new models can be applied to segment object geometries from synthetic and real images efficiently.

1.2 Organization of the Thesis

This thesis presents new models for the efficient segmentation of images. The proposed models are mainly based on the deformable model approach, in which curves and surfaces evolve under the influence of internal and external forces to delineate the shapes of image objects.

In Chapter 2, the various methods for image segmentation are introduced. In particular, popular methods which have been widely used in the segmentation of biomedical images are described.

In Chapter 3, a new deformable model that is based on a geometrically induced vector force is proposed. In particular, the external force field is derived from the interactions between the relative geometries of the deformable model and the image object boundary. The bidirectionality of the external force field allows the deformable model to handle weak object edges. In addition, the new vector force changes dynamically as the deformable model evolves, which allows the deformable model to propagate through boundary concavities and complex geometries. An efficient method to enhance the object edge representation of the geometric interaction field, which provides the deformable model with a great robustness to image noise is used. Several experimental results on both synthethic and real images are presented. A comparative analyis with several methods which consists of image gradient based [13,29,30] and region based methods [1] is presented. The images used in the experiments consist of multiple objects, boundary concavities, complex geometries, diffused object edges and image noise. In the comparative examples, it is shown that the proposed model outperforms the existing methods in terms of convergence to complex geometries and boundary concavities, robustness to noise, handling of intensity inhomogeneity and diffused object edges and invariance to initialization. It is also shown that the new deformable model can be applied for the efficient segmentation of biomedical images.

In Chapter 4, a robust framework for the segmentation of vascular geometries is presented. The approach includes the image denoising, optimal edge detection, and segmentation of the geometries using deformable model. The image smoothing and denoising is based on the vessel enhancing diffusion filter described in [31] which can be used to enhance the geometric structures of the vessel structures. The image object boundaries are derived using the Canny edge detection technique [32]. The object edge information is then used to compute the geometric interaction field which provides a more coherent and global representation of the image object edges. The deformable model based on the geometric interaction force is then used to segment the vessel geometries from the image. In particular, a region constraint is added so that the deformable model can easily get around calcified regions and propagate across the vessels to segment the geometries efficiently. The proposed framework is applied in the segmentation of carotid geometries from medical image datasets. The geometries segmented using the proposed framework are compared against geometries from manual segmentation. It is shown that the proposed framework can be used to segment the vascular geometries accurately.

In Chapter 5, a new variational level set model for image segmentation is proposed. The proposed model consists of an image based energy that propagates contours towards object boundaries, and a shape based energy that attracts the model towards similar shapes in the shape distribution derived from the training set. The segmentation model using a variational framework is formulated so that shape prior information provided by a training set of manually segmented shapes can be easily incorporated into the model. The image based energy consists of a contour smoothing term and an image attraction term based on the interaction of gradient vectors. The shape based energy is defined using a shape distance measure with intrinsic alignment. The shape prior information is incorporated into the model using nonparametric shape distribution, which allows the shape prior model to handle arbitrary shape variations. The training shapes used to derive the shape distribution are represented using signed distance functions. The proposed model is applied for the segmentation of synthetic and real images. It is shown that the proposed model with shape prior can efficiently handle image noise, occlusion, structures with similar intensity and diffused object edges to segment object shapes from the images.

In Chapter 6, a brief summary of the new segmentation models presented in the thesis is given. Some improvements that can be made to the deformable models, and some future directions are also described.

Chapter 2

Image Segmentation Methods

In this chapter, the state-of-the-art approaches to image segmentation are presented. In particular, some of the most popular techniques which have widely used in biomedical image segmentation from various modalities such as computed tomography (CT) and magnetic resonance (MR) imaging are introduced. The methods described can be categorized into thresholding, region growing technique, watershed technique, classification, clustering, graph based approaches, atlas based approaches, and deformable models.

2.1 Thresholding

The gray levels or intensity values of pixels or voxels belonging to a particular object in an image are typically different from those of other objects or the background in the image. Therefore group of pixels or voxels with similar intensity values can often be classified as belonging to the same object in an image. One of the simplest ways to partition an image based on the intensity of pixels or voxles is by setting a threshold on image intensities. Image thresholding creates a binary partition of the image intensities i.e. pixels with intensities greater than the threshold value are grouped into one object class and all other pixels into another object class.

Threshold values are often selected manually based on the inspection of the image histogram. There are also automated techniques such as the Otsu's method [33] for selecting the optimal threshold value from the image histogram. A particular category of thresholding techniques selects the threshold value based on the profile of the histogram. Some of these methods calculate the convex hull of the histogram [34] and select the threshold based on the deepest concavity points. Another method to select a suitable threshold is to carry out a peak analysis [35,36] of the histogram which can be done using convolution with smoothing and differencing kernels. However, image histograms are often noisy, thus causing many local minima and maxima, and substantial smoothing is often required to partition the modes.

There have been various applications of thresholding techniques in the segmentation of medical images. In [37], the trabecular bone is segmented based on a threshold value selected using structural and connectivity information of the bone estimated from the image using a range of threshold values. In [38], changes in the volume fraction of the segmented trabecular bone were measured for different threshold values. The optimal threshold value corresponding to the minimum change in volume fraction was then selected to segment the trabecular bone from MR images. An isosurface algorithm was applied in [39] to reconstruct the geometry of the vascular model from binary images of vessels segmented using a simple thresholding technique. The nasal cavity geometries in [40,41] were also segmented from CT images using image thresholding.

Thresholding is a simple technique for segmenting images in which different structures have contrasting pixel intensities. The main limitation of thresholding is that it considers only the intensity, and does not take into account the relationships between the pixels and spatial characteristics of the image. It is sensitive to noise and inhomogeneous intensity which are often present in medical images. It can therefore easily include extraneous pixels or miss some isolated pixels within the region, and often produce pixel groups which are not contiguous.

Recently, locally adaptive thresholding techniques have been developed to deal with the limitations of global thresholding. In these approaches, the threshold value is calculated at each pixel based on some local statistics or parameters of the pixel neighborhood. In [42,43], the local mean and standard deviation of the pixel neighborhood are used for adaptive thresholding. Another group of authors [44,45] consider the local contrast and compares the intensity of a pixel with neighboring pixel intensities. Local adaptive thresholding has been used in the segmentation of the trabecular bone structure from peripheral quantitative CT images [46], and in the segmentation of carotid artery from MR angiography images [47]. Such techniques are often based on the assumption that pixel intensities vary about some mean value, which is often not the case in medical images. Also, substantial amount of image smoothing is often required to reduce the effects of image noise for local thresholding techniques.

Thresholding is often used together with other techniques in a sequence of image extraction processes. For example in [48,49], the geometries of biomedical structures are segmented using thresholding and mathematical morphology [50]. A more detailed description on thresholding techniques is provided in [51,52].

2.2 Region Growing

The region growing techniques are used for extracting regions in an image which are connected according to certain homogeneity criterion such as image intensity, color and texture. It is based on the assumption that pixels or voxels which are in close proximity and having similar characteristics are likely to belong to the same object in an image. Region growing is often combined with other segmentation methods for the delineation of small, simple structures [53,54] in medical images. A rough approximation of blood vesseels in the form of binary images were first generated by thresholding the MR angiography data, followed by a thinning process to get the skeletonization of the geometry, which is then used to initialize the region growing process in [55]. In [56], fuzzy c-means is used to estimate the parameters of the Gaussian mixture model which is used to describe the local region characteristics of medical images. These parameters are then used to construct the homogeneity criterion for the region growing process. Morphological filtering is then applied to the images. In [57], a mesh model is first created from a rough approximation of the object's geometry extracted using a region growing algorithm, and then used as the initial surface of a deformable model for refining the extracted geometry.

Region growing techniques usually start from some user-selected seed points (usually within region of interest) to extract an image structure by incrementally adding neighboring points to the region based on some predefined criterion. At each iteration, the pixels or voxels neighboring the selected region are evaluated to determine if they should be considered as part of the region. If the pixels or voxels meet the homogeneity criterion, they are appended to the selected region and the iteration process continues until no similar pixels or voxels are added to the region.

Region growing algorithms vary depending on the homogeneity criterion used, the type of connectivity used to determine neighboring pixels, and the strategy used to visit neighboring pixels. The region can be set to grow until an image edge is met or until the difference between the selected pixel intensity and the average intensity of the region exceeds a tolerance value.

Region growing methods can produce well-defined object boundaries if the intensity variation within the region of interest (ROI) is small. However, in vascular structures that consist of long and narrow regions, even slow intensity changes can prevent the iterative process from adding more similar pixels. This lead to the development of locally adaptive region growing algorithms, which are designed to segment image objects with inhomogeneous intensity. A new region growing approach based on local cube tracking was used in [58] to segment vascular structures from CT and MR angiography images. This technique constrains the image object extraction process to each local cube so as to deal with the intensity variation in the image domain.

It is not a simple task to reconstruct the geometry of blood vessels accurately from medical images due to the range of the intensity variation. In order to facilitate an accurate segmentation of blood vessels by region growing techniques, the homogeneity criterion should be adaptable to the local characteristics in each ROI. Sekiguchi et al. [59] designed a branch-based region growing method in which the region growing process is performed on one branch at a time, thus allowing the homogeneity criterion to be optimized according to the local image characteristics.

In recent years, the concept of fuzzy analogies has also been incorporated to region growing segmentation [60–62]. It is based on the fact that medical images are inherently inhomogeneous and the image object is extracted by defining a group of pixels that exhibits a global hanging togetherness (fuzzy connectedness). The approach is to construct a fuzzy map of connectedness of every pixel and their relations with the user-specified seeds in the ROI.

Although spatial information is considered, region growing techniques can often lead to holes and over-segmentation due to noise and variations in image intensities. Also, partial-volume effects can cause different regions to become connected. It is also difficult for region growing techniques to extract narrow and long regions due to the sensitivity to image noise or low image resolution.

2.3 Watershed

The watershed transform [63, 64] is derived from the field of mathematical morphology. In this approach, the image is interpreted as a landscape or topographic surface, with the pixel intensity representing the elevation of the topographic surface. Consider water on the landscape flowing towards regions with local minima, the watersheds are the lines that partition these regions. In this way, the image is partitioned into homogeneous regions with the watersheds defining the boundaries of the regions. The watershed transform [65] was used in [66, 67] to extract the geometry of the carotid. The watershed transform tends to be sensitive to noise and often produces over segmentation. It is also difficult for the watershed technique to extract thin structures and weak object edges.

2.4 Classification

Image classifiers [68] are supervised methods that can be used to partition a feature space derived from an image into different categories based on a set of training data. Typical features of an image are pixel intensity, local gradient, density, color, and distance from landmark. Multiple or n number of features can be placed together to form a feature vector, which defines a data point location in n-dimensional feature space. In particular, a pixel or voxel in an image denotes a point in the feature space, and a classified group is a region in the feature space with a high density of such points. The training set for the classifier is derived by manual segmentation such that a set of criteria for pattern recognition is defined, and then used as references for the automatic segmentation of new data.

There are numerous ways in which training data can be applied for image classification. The k-nearest neighbor [69] approach classifies image pixel into the same class as the majority of the k-nearest training data. In particular, this classifier finds k nearest neighbors of the unknown feature vector from the training vectors, and assigns the unknown vector to the class based on majority vote among the k points. This is usually done using Euclidean distance measure which does not reflect the global geometrical information of the training samples. In [70], the global geometrical information is incorporated and parameter tuning is not required.

Another approach, the Parzen window carries out the classification by using a weighted decision process within a predefined window function of the feature space, centered at the unlabeled pixel intensity. The k-nearest neighbor and Parzen window are considered nonparametric classifiers because they do not make underlying assumption about the statistical structure of the data.

The maximum likelihood or Bayes classifier [71] is a commonly used method for parametric classification. In this approach, pixel intensities are assumed to be independent random variables with parameterized probability distributions, usually Gaussian for medical images. A mixture model is then defined in which the probability distribution can be computed as a multiplication of the parameterized probability functions. The training data are collected by acquiring representative samples from components of the mixture model and then estimating the K-means, covariances, and mixing coefficients.

The Bayesian model for pixel classification can be mathematically given as,

$$P(\theta_i|x) = \frac{p(x|\theta_i)P(\theta_i)}{p(x)} \tag{2.1}$$

where

$$p(x) = \sum_i p(x|\theta_i)P(\theta_i) \tag{2.2}$$

Here $P(\theta_i|x)$ denotes the posterior probability which is the conditional probability of the class θ_i given the feature vector x of a pixel, that is assigned after the relevant information is taken into account. $p(x|\theta_i)$ is the likelihood which is the probability of x given the class θ_i and represents the data now available. $P(\theta_i)$ is the prior that is the probability of the event computed before the collection of new data. Classification of new data can now be obtained by assigning each pixel to the class with the highest posterior probability calculated.

Classifiers are relatively computationally efficient and can be applied to multichannel images [72,73]. One major drawback of classifiers is the requirement of manual interaction to segment the image and obtain the training set, which can be laborious. Also, the use of the same training set for a large number of image scans can lead to biased results that do not consider the variability within individuals. Recent improvements in image classification include the incorporation of spatial, neighborhood and geometric information [74–77].

2.5 Clustering

Clustering techniques are unsupervised classification methods that group objects into different categories, with objects within each class exhibiting similar characteristics. Clustering methods generally perform in a similar fashion as image classification methods, but without using any training data. In particular, clustering techniques iterate between image segmentation and characterization of properties of each class. In other words, data training is done intrinscially using the available data in clustering techniques. Some commonly used clustering methods are the K-means or ISODATA [78–81], fuzzy c-means [82–84], and expectation maximization (EM) algorithms [85–87].

The K-means method is used to minimize intra-cluster variability, which is the sum of squared distances between all points and the cluster centre, given by

$$Var = \sum_{i=1}^{K} \sum_{x \in C_i} |x - \mu_i|^2 \tag{2.3}$$

where x represents the selected image pixel, K is the number of clusters, and μ_i is the centre of cluster C_i. In other words the K-means method partitions data by iteratively computing a mean intensity for each class, and segmenting the image by classifying each pixel in the class with the closest mean. ISODATA is similar to K-means, except that it does not assume a given number of clusters. A large K is usually chosen initially, and clusters are removed when their cluster centre are not assigned enough samples, thus obtaining an optimal number of clusters. The fuzzy c-means algorithm is also similar to the K-means algorithm, but it allows data to belong to two or more clusters. In this technique, a class membership is assigned to a data point based on the similarity of the data point to a particular class relative to the other groups. The EM is an iterative optimization method that generally uses the same clustering principles, with the assumption that the data follow a finite Gaussian mixture model. It alternates between computing the posterior probabilities and estimating the maximum likelihood of the means, covariances and mixing coefficients of the mixture model.

Image clustering approaches are efficient for acquiring global characteristics, however they do not directly incorporate spatial modelling, and are thus sensitive to noise and intensity inhomogenities. Recent developments in image clustering techniques include the use of Markov Random Field (MRF) models [88], graph based theory [9] and particle swarm optimization (PSO) algorithm [89] which take into consideration the spatial information of images. More information and descriptions on image classifiers and clustering methods can be found in [90,91].

2.6 Graph Based Approaches

In recent years, graph based approaches [7–10] have been applied to the problem of image segmentation. Such techniques are based on combinatorial optimizations which can be used to minimize a cost function defined on a discrete set of variables. In this approach, the image is represented using an adjacency graph consisting of vertices which represent the image pixels or voxels. The vertices are connected by edges, with the weight of an edge representing the similarity between two corresponding pixels. The graph edges are assigned some non-negative weights or costs, and a cut is a subset of edges that partition the vertices into disjoint sets. The cost of the cut is the sum of the costs of all edges that are cut. In [92], the cost function is formulated as a boundary based metric, and a minimum cut approach is used to partition a graph into subgroups such that the maximum cut across the subgroups is minimized. The minimum cut is considered as the cut that minimizes the energy function to provide the optimal segmentation. Such graph partitioning techniques however has a bias towards smaller regions with short boundaries [93]. The normalized cut technique [8] was introduced to reduce such bias by using a cost function which considers both the total dissimilarity between the different groups and the total similarity within the groups. This however causes the technique to favour similar weight partition [94]. The graph cuts approach in [7, 10] provides a more interactive framework for image object segmentation compared to other graph based methods [8,9]. In this technique, there are two special vertices designated as the source and sink that represent image object and background labels respectively. An s-t cut is a subset of edges such that the source and sink is partitioned on the induced graph. In particular, the user can provide information to regularize the segmentation model by interatively selecting foreground and background regions in the image. The object contour is assumed to be the global minimum within the image given the user-specified constraints. As such, the extracted geometry varies with the interactive input. The cost function which can consist of boundary and regional information has to be well defined for graph cuts to provide a globally optimal solution. In addition, straightforward implementations of graph cut algorithms such as the max-flow algorithms can be computationally expensive. The discrete representation of the graphs may produce geometric artifacts, and techniques such as the ones described in [10, 92] have a bias towards cuts with short boundaries.

2.7 Atlas Based Approaches

Atlas based approaches use a standard atlas or template as a guide to perform medical image segmentation. The atlas is generated by compiling relevant information (i.e. location, shapes and spatial relationships) of anatomical structures. One way to create an atlas is to manually segment an image. This atlas is then used as a reference frame for the segmentation of new image data.

In general, atlas guided approaches perform segmentation based on image registration techniques [6]. An image can be segmented by finding a transformation that maps a segmented template image to the target image that requires segmentation. This process of warping the atlas to the target image can be performed using linear and nonlinear transformations.

Atlas based approaches are often used for the segmentation and analysis of various structures from MR brain images [95–99]. An advantage of atlas based approaches is that the labeling of tissues or anatomical structures is transferred as well as the segmentation. It is however difficult for atlas based approaches to find accurate segmentations of complex structures due to the variability of anatomical structures. Different authors [95, 100–102] have applied a sequence or combination of linear and nonlinear transformations to overcome this problem, but the computed deformation field is often not precise enough to warp the image and get the segmentation accurately. Thus, atlas based approaches are more suited for the segmentation of anatomical structures which exhibits slight variability between different individuals.

2.8 Deformable Models

Deformable models [1, 19, 29, 103] are curves and surfaces that can deform under the influence of internal and external forces to delineate an object boundary from the image. One of the earliest deformable models for image segmentation was introduced in the form of active contours in [19]. Deformable models have since become one of the most widely explored areas in image segmentaion, and have been applied for the segmentation and analysis of anatomic structures from various imaging modalities [104–106]. In general, deformable models can be categorized into explicit [19,103] and implicit models [1,29,107].

2.8.1 Explicit Deformable Models

Explicit deformable models represent curves and surfaces parametrically during deformation. This parametric contour and surface representation allows the explicit deformable models to track the points of the curves and surfaces across time, and is therefore well suited for real-time applications due to the fast computation time.

The classic active contour is a parameterized curve C represented by $\boldsymbol{x}(s)$, where $\boldsymbol{x}$ denotes the position vector in a Cartesian frame and s is the arc length. The energy functional can be defined on the contour as

$$E(\boldsymbol{x}) = E_{int} + E_{ext} \tag{2.4}$$

where E_{int} and E_{ext} denote the internal and external energies of the contour respectively. The internal energy is used to regularize the smoothness of the contour and is defined as

$$E_{int} = \int_0^1 \frac{1}{2}\Big(\alpha(s)|\frac{\partial \boldsymbol{x}(s)}{\partial s}|^2 + \beta(s)|\frac{\partial^2 \boldsymbol{x}(s)}{\partial s^2}|\Big)ds \tag{2.5}$$

where $\alpha(s)$ and $\beta(s)$ are parameters that control the tension and rigidity of the model respectively, and are usually set as constants, i.e. $\alpha(s) = \alpha$ and $\beta(s) = \beta$. For example, large values of α and β will allow less amount of stretching and bending of the contour respectively. In contrast, small values of α and β will place less constraints on the size and shape of the contour respectively, and allow more stretching and flexibility of the contour.

Note that careful tuning of these parameters is required, as large values of these parameters may cause over smoothing and shrink the contour, while small values of these parameters may cause the contour to be sensitive to local minima such as image noise. The external energy attracts the contour towards object boundaries in the image, and can be defined as

$$E_{ext} = \int_0^1 E_{img}(\boldsymbol{x}(s))ds \tag{2.6}$$

where $E_{img}(\boldsymbol{x}(s))$ denotes a scalar potential function defined on the image. The external potential function is usually derived such that the local minima of $E_{img}(x, y)$ coincide with intensity extrema, object edges and features of interest in the image. An example of the image attraction function can be defined as

$$E_{img}(x, y) = -c|\nabla G_\sigma(x, y) * I(x, y)|^2 \tag{2.7}$$

where c is a weighting parameter that controls the magnitude of the potential, and G_σ denotes a Gaussian smoothing filter with standard deviation σ. Here, $I(x, y)$ represents the image intensity and $*$ denotes the convolution operator. According to the calculus of variations, the contour that minimizes the energy functional $E(\boldsymbol{x})$ in equation (2.4) must satisfy the Euler-Lagrange equation [104, 108]

$$\frac{\partial}{\partial s}\left(\alpha\frac{\partial \boldsymbol{x}}{\partial s}\right) - \frac{\partial^2}{\partial s^2}\left(\beta\frac{\partial^2 \boldsymbol{x}}{\partial s^2}\right) - \nabla E_{img}(\boldsymbol{x}) = 0 \tag{2.8}$$

The active contour can be expressed as a function of the arc length s and time t, i.e. $\boldsymbol{x} = \boldsymbol{x}(s, t)$. The evolution of the contour can then be defined as

$$\frac{\partial \boldsymbol{x}}{\partial t} = \frac{\partial}{\partial s}\left(\alpha\frac{\partial \boldsymbol{x}}{\partial s}\right) - \frac{\partial^2}{\partial s^2}\left(\beta\frac{\partial^2 \boldsymbol{x}}{\partial s^2}\right) - \nabla E_{img}(\boldsymbol{x}) \tag{2.9}$$

Another approach to compute the local minima of the energy functional is to use a dynamic force formulation. The dynamics of the active contour $\boldsymbol{x}(s, t)$

with mass density $\mu(s)$ and damping density $\gamma(s)$ can be defined as

$$\mu\frac{\partial^2 \boldsymbol{x}}{\partial t^2} + \gamma\frac{\partial \boldsymbol{x}}{\partial t} = \boldsymbol{F}_{int}(\boldsymbol{x}) + \boldsymbol{F}_{ext}(\boldsymbol{x}) \tag{2.10}$$

where $\boldsymbol{F}_{int}$ is the internal force given as

$$\boldsymbol{F}_{int}(\boldsymbol{x}) = \frac{\partial}{\partial s}\left(\alpha\frac{\partial \boldsymbol{x}}{\partial s}\right) - \frac{\partial^2}{\partial s^2}\left(\beta\frac{\partial^2 \boldsymbol{x}}{\partial s^2}\right) \tag{2.11}$$

and $\boldsymbol{F}_{ext}$ is the external force which can be defined as

$$\boldsymbol{F}_{ext}(\boldsymbol{x}) = -\nabla E_{img}(\boldsymbol{x}) \tag{2.12}$$

Such a force formulation for the active contour allows the incorporation of various types of forces to regularize the model. A convenient technique to define the external force is to use a linear summation of different forces and can be expressed as

$$\boldsymbol{F}_{ext}(\boldsymbol{x}) = \sum_{i=0}^{N} \boldsymbol{F}_i(\boldsymbol{x}) \tag{2.13}$$

where N denotes the number of forces. The contour converges when the internal and external forces balance, and the equilibrium of the system is achieved.

Although traditional active contours have been widely applied in the segmentation of biomedical images, there are some limitations involved in using them. Traditional active contours are very sensitive to parameters. They have a small capture range and initial contours have to be placed close to the boundaries of the image objects in order to draw the contours towards them. The parametric active contours often have difficulties dealing with boundary concavities. Several techniques have been used to address the convergence issues of explicit deformable models. In [108], a pressure force is used to increase the attraction range of the model. However, it requires careful setting of the pressure force to inflate or deflate the model, as a strong force may easily overwhelm the weak edges. In [109], an external force computed using a distance map is used to increase the attraction range. The distance potential force however attracts the model points to the nearest edge, which can often cause difficulties for the model to propagate into boundary concavities. The external force field in [103] uses a diffusion of the image based potential function, which improves the attraction range and handling of boundary concavities of the deformable models. It however has convergence issues such as saddle or stationary points in the force field. It is also difficult for the explicit models to handle topological changes, such as splitting or merging during the deformation. In order to handle topological changes, McInerney and Terzopoulos [20, 110] designed topology adaptive deformable models. During the deformation, the model is periodically reparameterized with a new set of nodes and elements by computing its intersections with a regular simplicial partitioning of space. These intersection points are used as the nodes of the new contour or surface. The grid vertices that have moved from the exterior to the interior of the deformable model are then labeled to continuously track the interior grid vertices, such that the new contour or surface can be determined. This technique however works well only when the model inflates or deflates everywhere [111], which limits its applications in medical image analysis. Several techniques [21–23] have also been designed to handle topological changes. However, these approaches usually involve a set of heurestic rules to detect self-intersections and handle merging of the evolving model.

2.8.2 Implicit Deformable Models

Implicit deformable models are introduced by Caselles *et al.* [11] and Malladi *et al.* [12] to address some of the limitations of parametric deformable models. The implicit deformable models are implemented using the level set method introduced by Osher and Sethian [24] for front propagation. In this approach, the evolution of curves and surfaces are represented implicitly as a level set of a higher-dimensional scalar function. As the deformation of the model is based on geometric measures such as the unit normal and curvature, the evolution is independent of the parameterization and topological changes can be handled automatically. Consider a contour represented implicitly as the zero level set of the function $\phi(\boldsymbol{x}) : \Omega \rightarrow \Re$ such as

$$C = \{\boldsymbol{x} \in \Omega \,|\, \phi(\boldsymbol{x}, t) = 0\} \tag{2.14}$$

where Ω denotes the image domain, and $\phi(\boldsymbol{x}, t)$ is the evolving level set function. The level set function is defined as positive inside the boundary of the propagating front, and negative outside the propagating front as

$$\begin{cases} \phi(\boldsymbol{x}, t) > 0 \, \text{for} \, \boldsymbol{x} \in \Omega_{in} \\ \phi(\boldsymbol{x}, t) < 0 \, \text{for} \, \boldsymbol{x} \in \Omega \backslash \Omega_{in} \\ \phi(\boldsymbol{x}, t) = 0 \, \text{for} \, \boldsymbol{x} \in \partial\Omega_{in} = C \end{cases} \tag{2.15}$$

where Ω_{in} is a region in Ω with a boundary $\partial\Omega_{in}$ defined by the contour C. Figure 2.1 depicts the level set function and the various level set contours.

The propagating front of the level set function is defined as $\phi(\boldsymbol{x}(t), t) = 0$, and the evolution equation can be derived using chain rule as

$$\frac{\partial \phi}{\partial t} + \nabla \phi \cdot \frac{\partial \boldsymbol{x}}{\partial t} = 0 \tag{2.16}$$

The evolution of a contour along its normal direction can be expressed as

$$\frac{\partial \boldsymbol{x}}{\partial t} = V(\kappa)\boldsymbol{n} \tag{2.17}$$

where V is the speed function that determines the speed of the front propagation. κ denotes the mean curvature of the evolving front and is defined as

$$\kappa = \nabla \cdot \frac{\nabla \phi}{|\nabla \phi|} \tag{2.18}$$

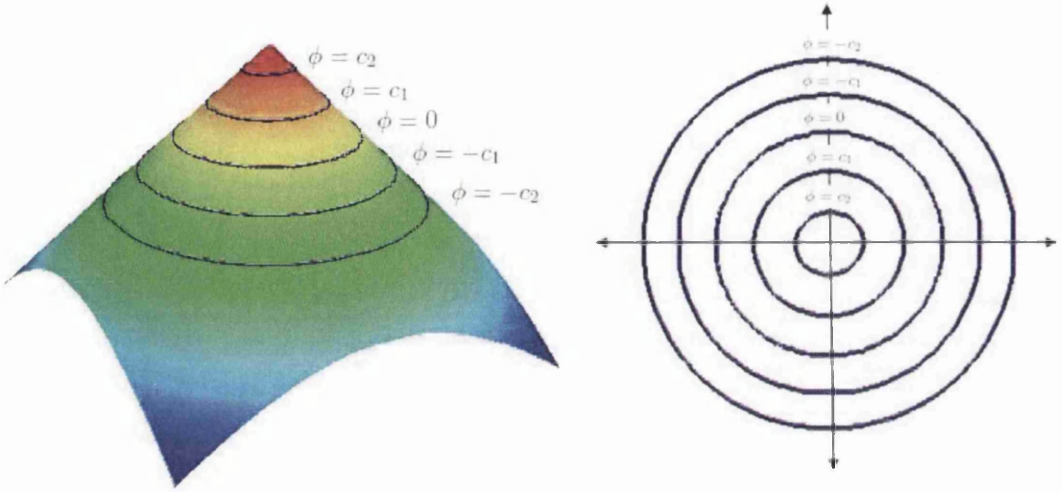

Figure 2.1: Level set function and the corresponding level set contours.

and $\boldsymbol{n}$ is the unit normal of the contour defined as

$$\boldsymbol{n} = -\frac{\nabla\phi}{|\nabla\phi|} \tag{2.19}$$

The level set evolution equation can thus be expressed as

$$\frac{\partial\phi}{\partial t} = V(\kappa)|\nabla\phi| \tag{2.20}$$

The numerical implementation of (2.20) can be computationally expensive, as the evolving contour is represented implicitly in a higher-dimensional function. There are however efficient methods such as the fast marching method [112] and the narrow band method [25] which can be used to reduce the computational cost of evolving the level set function. Although the fast marching method can be used to reduce the computational cost significantly, they are designed for problems in which the sign convention of the speed function is constant. In other words, the front can only propagate forward or

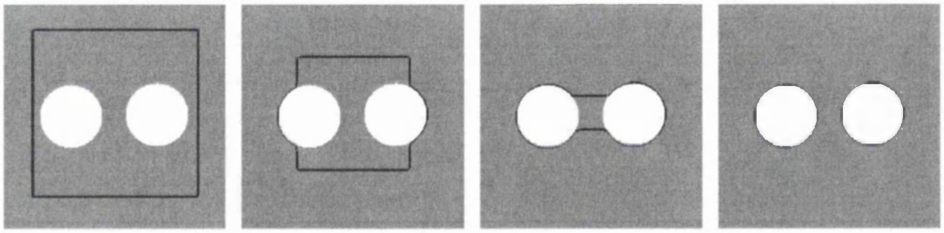

Figure 2.2: Segmentation of image objects using implicit deformable model.

backward in a single direction, which can limit the applications of the technique. Also, the fast marching method is only suitable for steady problems, i.e. $\frac{\partial \phi}{\partial t} = 0$. The narrow band method provides an efficient solution for the front propagating problem by considering only a narrow band of pixels or voxels that are located in the vicinity of the current level set interface.

The level set method provides an elegant approach to formulate the deformable models for efficient image segmentation. The implicit deformable model can be used to extract multiple objects in an image, and can handle topological changes automatically. Figure 2.2 depicts the segmentation of disc objects from an image using implicit deformable model. As shown in the figure, the initial contour is set outside the disc objects, and is allowed to propagate and localize on the boundaries of the image objects. Figure 2.3 depicts the evolution of the level set function, and the changes in topology in the corresponding level set contour.

The implicit deformable models are generally categorized into image intensity gradient based methods and region based methods. The classic geometric active contour model introduced in [11, 12] is an image intensity gradient based model which uses an edge stopping function derived from an image which is smoothed by a Gaussian filter. The geometric active contour uses a constant force to expand or shrink the contour in the normal direction towards object boundaries. As such, the contour has to be initialized inside or outside the image object. The consant force used in the model can easily overwhelm weak object edges in the image. Various methods have

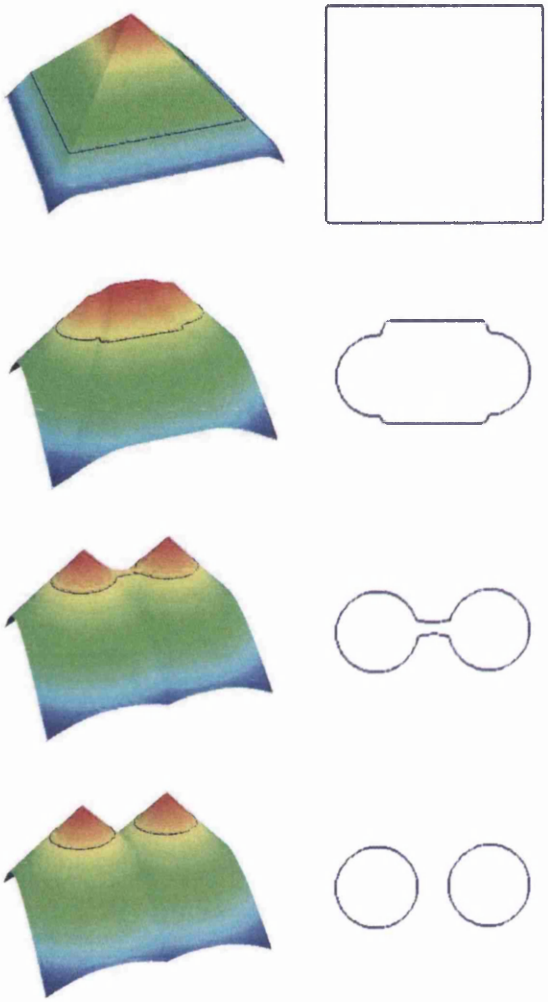

Figure 2.3: The changes in topology in the evolution of the level set function. The left column presents the evolution of the level set function and the right column shows the corresponding level set contour.

been proposed to improve the performance of image intensity gradient based models [29, 113, 114]. In general, the image intensity gradient based models are sensitive to local minima such as noise as they make use of only local image information. The region based active contours [1, 47, 107] make use of the similarity of image characteristics to extract objects from the image. The image attraction energy used in such models is often derived from global image information. The region based models are therefore more robust to image noise and intializations of the contours. They are however based on the assumption that image objects are composed of homogeneous image characteristics such as intensity and colour, which limits their applications in real image dataset. In addition, region based models often have difficulties dealing with intensity inhomogeneity in the image.

2.9 Summary

This chapter introduced some of the most popular state-of-the-art methods for image segmentation. The methods described have been widely applied in the segmentation of biomedical image datasets. The various techniques are analysed, and the advantages and disadvantages in using these techniques are described. In particular, the various classes of deformable models, the formulation and convergence issues of the deformable models when applied to image segmentation are described. Table 2.1 shows the advantages and disadvantages of the various methods for segmentation. Although the thresholding, region growing and watershed techniques are simple and fast, they are sensitive to noise and intensity inhomogeneity. Classification methods are relative fast but requires large training set and are often biased towards shapes in training set. Clustering techniques are sensitive to noise as they often do not consider spatial information. Graph based methods are robust to noise but they are computationally expensive and are often biased towards smaller regions. Atlas based methods produces labelling of image objects but have difficulty handling large shape variability in complex geometries. Deformable models can easily adapt to local features, and can incorporate forces to regularize the smoothness and shapes of the contours. In the next chapter, a new approach for efficient segmentation of images by deriving a geometric based external force field for deformable models is proposed.

Table 2.1: Various methods for segmentation of images

Segmentation methods	Advantages	Disadvantages
Thresholding	simple, fast	sensitive to noise, sensitive to intensity inhomogeneity
Region growing	simple, fast	sensitive to noise, sensitive to intensity inhomogeneity
Watershed	simple, fast	sensitive to noise, sensitive to weak edges, produces over segmentation, difficulty in handling thin structures
Classification	relatively fast	large training set, biased towards training shapes
Clustering	relatively fast	sensitive to noise, do not consider spatial information
Graph based approaches	robust to noise, combinatorial optimization	computationally expensive, biased towards smaller regions
Atlas based approaches	produces labelling of image objects	computationally expensive, difficulty in handling large variability in shapes
Explicit deformable models	relatively fast, easily adapt to local features, can easily incorporate regularization forces	difficulty in handling boundary concavities, difficulty in handling topological changes
Implicit deformable models	easily adapt to local features, automatic handling of topological changes, can easily incorporate regularization forces	computationally expensive

Chapter 3

Geometrically Induced Force Interaction for Contour and Surface Evolution

3.1 Introduction

The design of deformable models often varies in the representation of the object boundary and external force field used. There have been numerous publications on deformable models and improvement of the underlying techniques. These usually take the form of image gradient based approaches e.g. [12, 103, 114–116], region based approaches e.g. [1, 117] and hybrid approaches e.g. [118, 119]. Image gradient based techniques have been found useful when there is limited prior knowledge and image gradients are reasonable indications of object boundaries. However, the extension from 2D to 3D is not trivial. Conventional image gradient based approaches, such as the one in [12], require careful initialization even in 2D [117]. Although several improvements have been developed, e.g. [103, 114], it remains a great challenge for image gradient based models to achieve initialization invariance and robust convergence. This is especially true when segmenting objects with complex geometries and shapes in 3D, where delicate manual initialization is more difficult than in 2D.

Region based methods [1,47,107,117,120] have also been widely applied to image segmentation. The Chan-Vese model [1] which is based on the Mumford-Shah functional [121] is considered as one of the most popular region based techniques. In this approach, the image is assumed to be composed of regions of approximately piecewise-constant intensities. The Chan-Vese model then extracts the image object based on the average intensities inside and outside the contour. Although the Chan-Vese model can be used to extract objects with smoothly varying boundaries, it has difficulties dealing with image regions with intensity inhomogeneity. Other region based models such as [47,107] also assume that image objects consist of distinct regional features, which is often not true for real image dataset due to intensity inhomogeneity and multi-modal nature.

In this chapter, a novel deformable model with an external force field based on the relative position and orientation of the deformable model and object boundaries is proposed. The external force field is called the *geometric potential force (GPF) field* as it is based on the hypothesized interactions between the relative geometries of the deforming surface and the object boundaries (characterized by image gradients). The evolution of the deformable model is solved using the level set method so as to facilitate topological changes. The proposed external force field can attract the deformable model to object boundaries with arbitrary initialization, and allows the deformable model to reach highly concave regions which are generally difficult for other methods. The vector force field introduced, can be viewed as a generalized version of the magnetic force field described in the recent magnetostatic active contour (MAC) model [116]. The proposed method uses a vector force field computed based on geometric properties such as unit vectors and unit normals which can be easily derived, and can therefore be conveniently extended to higher dimensions. In contrast, the MAC model cannot be directly applied to 3D image dataset as it is not apparent how the hypothesized current direction represented by tangent vectors can be estimated and set on a 3D object. It is shown that the proposed model can be applied to segment complex geometries from synthetic and real image datasets efficiently.

3.2 Related Work

In image gradient based deformable models, it is assumed that object boundaries coincide with image intensity discontinuities. In region based techniques, an image object is assumed to have distinctive and continuous regional features such as colour and texture, which is not always true for real world data due to intensity inhomogeneity and multi-modal nature of the images. Conventional image gradient based methods have difficulties in dealing with boundary concavities, weak edges, image noise and difficult initializations as they are generally prone to local minima that often appear in real images. Numerous research works have been performed in order to improve the initialization and convergence capabilities of the gradient based approaches.

The geodesic active contour model [29] uses an image dependent constant flow to move each point on the deformable model in the direction of its normal at a speed proportional to the edge stopping function. This function monotonically shrinks or expands the contour towards the object boundary and plays an important role in the geodesic model, and in subsequent incremental improvements, such as [113]. This method often produces leaking of the deformable model on images with indistinct object boundary or boundary gaps. This is due to the fact that the edge stopping term only slows down the curve or surface near the boundary, and a relatively large pressure term can easily overwhelm it. Also, the edge stopping function which is similar to the ballon force, a constant inflation or deflation force used in [12], can only monotonically shrink or expand the contour depending on the sign convention of the pressure term. As such, cross-initialization of the contour which is useful in segmenting complex and compact geometries cannot be applied to the image dataset.

The geodesic model [29] can be expressed as:

$$\frac{\mathrm{d}\boldsymbol{x}}{\mathrm{d}t} = g(\alpha\kappa + C)\,\hat{\boldsymbol{n}} - (\nabla g \cdot \hat{\boldsymbol{n}})\,\hat{\boldsymbol{n}} \tag{3.1}$$

where C is a constant pressure term, κ and $\hat{\boldsymbol{n}}$ are the curvature and inward unit normal of the contour respectively, and α is a weighting parameter that controls the smoothness of the contour. The edge stopping function $g(\boldsymbol{x})$ is given as:

$$g(\boldsymbol{x}) = \frac{1}{1 + f(\boldsymbol{x})} \tag{3.2}$$

where $f(\boldsymbol{x})$ is a function that represents the image object edge, and is usually set to the image gradient magnitude. α is set according to the amount of noise, i.e. α is increased if the amount of noise is increased. However, too large a value of α may cause the contour to shrink. The constant C can be positive or negative depending on the direction of propagation. If C is too small, the contour may not propagate to the object edges, and if C is too large, the contour may overwhelm weak object edges.

The gradient vector flow (GVF) and its generalized version GGVF [13, 103] have shown significant improvements over conventional external force field such as the geodesic model [29] and have been widely used in deformable models, e.g. [16]. It uses a vector diffusion equation that diffuses the gradient of an edge map to regions distant from the object boundary. The amount of diffusion adapts according to the image edge strength, and is designed such that there will be very little smoothing of the vector field in the proximity of large image gradients.The GGVF model can be defined as:

$$\frac{\mathrm{d}\boldsymbol{x}}{\mathrm{d}t} = \alpha g\,\kappa\,\hat{\boldsymbol{n}} + (1 - \alpha)(\boldsymbol{v} \cdot \hat{\boldsymbol{n}})\,\hat{\boldsymbol{n}} \tag{3.3}$$

where $\boldsymbol{x}$ denotes a position vector on the deformable contour, t denotes the artificial time component, g is the stopping function, κ is the curvature, $\hat{\boldsymbol{n}}$ is the unit normal, and α is a real constant to balance the contribution of the curvature term; $(\boldsymbol{v} \cdot \hat{\boldsymbol{n}})\,\hat{\boldsymbol{n}}$ is the flow component normal to the contour. Let I denote the image intensity and $u = |\nabla I|$ be the image gradient magnitude. The diffused gradient vector flow field $\boldsymbol{v}(\boldsymbol{x})$ is given as the equilibrium solution to the following PDE:

$$\frac{\partial \tilde{\boldsymbol{v}}}{\partial t} = w_1(|\nabla u|)\nabla^2 \tilde{\boldsymbol{v}} - w_2(|\nabla u|)(\tilde{\boldsymbol{v}} - \nabla u) \tag{3.4}$$

where $w_1(|\nabla u|) = e^{-(|\nabla u|/K)}$ and $w_2(|\nabla u|) = 1 - w_1(|\nabla u|)$ are weighting functions which control the amount of diffusion according to the gradient of the edge map. K is a parameter that controls the amount of field smoothness, and can generally be set to $K = 0.05$ to $K = 0.2$ depending on the amount of noise [13]. Although the GGVF has been shown to improve the capture range and boundary concavities tracking ability, it has convergence issues caused by saddle or stationary points in its force field, i.e. when the contour is tangent to the force vector [116, 122].

In [122], a distance transform based on a modified mean curvature flow was used to compute the curvature vector flow (CVF), which can be used to attract contours into boundary concavities. Curvature flow was used to evolve the object boundaries till they were no longer concave. The inward or outward propagation was defined by monotonically non-negative or non-positive curvature flow respectively. A distance map was then computed based on the evolution of a contour, from which the CVF can be defined. This method only reduces the number of stationary or saddle points. It is also noted that the CVF active contour requires that the object boundary be closed, i.e. there should be no gaps along the object boundary, otherwise pre-processing is required to close the gaps along the object boundaries. However, image datasets often come with weak object edges and broken boundaries.

Recently, there have been several research works on physics-based deformable models such as the ones described in [49, 116, 123]. In [123], a charged-particle model (CPM) based on electrostatics was applied to attract particles toward object boundaries. Jalba *et al.* [123] hypothesized a set Ω of freely moving particles with the same positive charge q in an external electrostatic field, generated by fixed negative charges $e_{\boldsymbol{x}}$ proportional to the image gradient $|\nabla I(\boldsymbol{x})|$ at point $\boldsymbol{x}$. The positively charged particles are attracted towards the fixed negative charges under the influence of the external particle-mesh force $\mathbf{F}_a$ and repelled by each other by the particle-particle force $\mathbf{F}_r$. These forces acting on a moving particle at position $\boldsymbol{x}$ can be computed as the sums

$$\mathbf{F}_a(\boldsymbol{x}) = \frac{q}{4\pi\epsilon} \sum_{\boldsymbol{x}' \neq \boldsymbol{x}} e_{\boldsymbol{x}'} \frac{\hat{\boldsymbol{r}}_{\boldsymbol{x}\boldsymbol{x}'}}{r^2_{\boldsymbol{x}\boldsymbol{x}'}}, \; \mathbf{F}_r(\boldsymbol{x}) = \frac{q^2}{4\pi\epsilon} \sum_{\substack{\boldsymbol{x}' \in \Omega \\ \boldsymbol{x}' \neq \boldsymbol{x}}} \frac{\hat{\boldsymbol{r}}_{\boldsymbol{x}\boldsymbol{x}'}}{r^2_{\boldsymbol{x}\boldsymbol{x}'}} \tag{3.5}$$

where ϵ is the permittivity, $\hat{\boldsymbol{r}}_{\boldsymbol{x}\boldsymbol{x}'}$ is the unit vector in the direction from $\boldsymbol{x}$ to $\boldsymbol{x}'$, $r_{\boldsymbol{x}\boldsymbol{x}'} = |\boldsymbol{x} - \boldsymbol{x}'|$ is the distance between these two points. The total force acting on a particle is given by $\mathbf{F} = w_a\mathbf{F}_a + w_r\mathbf{F}_r + w_d\,\mathbf{F}_d$ where w_a, w_r and w_d are weighting parameters for the attraction force $\mathbf{F}_a$, repulsion force $\mathbf{F}_r$ and damping force $\mathbf{F}_d = -\frac{\mathrm{d}\boldsymbol{x}(t)}{\mathrm{d}t}$ respectively. A low ratio of w_r to w_a will cause the particles to be attracted to spurious edges while a high ratio will cause the particles to move through weak object edges. In contrast, a small w_d will cause the particle to cross over object edges while a large w_d will increase the viscous effect on the particles. The values of the parameters can be set to $w_a = 0.5$, $w_r = 0.7$ and $w_d = 0.5$ for a wide range of images. When the particles attain a stable equilibrium state due to the viscous effect of $\mathbf{F}_d$, contour reconstruction is required to obtain the object boundary representation. Although this approach can resolve the above-mentioned convergence issues, the fact that particles on weak edges may be attracted to nearby strong edges often causes broken contours to be formed. In addition, the method requires frequent particle insertion and deletion, which is computationally expensive, which makes it impractical in 3D. Yang *et al.* [124] incorporated the particle model [123] into a contour model and showed subsequent improvements on the CPM. In their approach, a positively charged active contour moving in an hypothesized electrostatic field with field strength proportional to image gradient magnitudes, is attracted to image edges based on a boundary attraction force based on the Lorentz force described in Equation (3.5). A boundary competition force is then used to repel nearby free contours from moving towards the already occupied image boundary. The repulsion force was generated in such a way that contours that have reached object boundaries will exert repulsion forces upon other contours while being minimally affected by other contours. However, the dominant external force field is static and its dynamic behavior due to repulsion force can be difficult to control. Park and Chung [125] also considered the pixels in the image edge map as static electric charges and used an external force equivalent to $\mathbf{F}_a$ in Equation (3.5) in their parametric model. Similar to [123], their parametric model based on hypothesized electric field computed from the edge map cannot deal with leakage at weak edges when strong nearby edges are present. Zhu *et al.* [126] incorporated tangent direction of the image map to compute a modified version of the electric potential force field. The tangent direction information is obtained by a 90° rotation of the gradient vectors of the smoothed image, and is coupled with a new parameter that controls the influence of the rotated vectors and the corresponding force field. This enhances the intensity of the hypothesized electric potential along the image edge and allows the active contour to better handle weak edge. However, the performance of the modified external force field in preventing leakage at weak edges is greatly determined by the value of the new parameter, which also affects the noise sensitivity of the active contour. In other words, the noise sensitivity of the modified electric field active contour increases together with its performance in handling weak image edges.

Li and Acton [49] used an external force calculated from the convolution of a vector field and the image edge map to attract the active contour towards image boundaries. The vector field kernel $\mathbf{k}(\boldsymbol{x})$ consists of radial symmetric vectors pointing towards the center of the kernel, and is given as $\mathbf{k}(\boldsymbol{x}) = m(\boldsymbol{x})\hat{\boldsymbol{x}}$, where $m(\boldsymbol{x})$ is the magnitude, $\hat{\boldsymbol{x}} = -\boldsymbol{x}/r$ is the unit vector pointing to the kernel origin, and $r = |\boldsymbol{x}|$ is the distance from the kernel origin. The magnitude $m(\boldsymbol{x})$ of the vector field kernel should be a decreasing positive function of distance from the origin, and can be given as $m(\boldsymbol{x}) = (r + \epsilon)^{-\gamma}$ which is inspired by the gravitational law, or $m(\boldsymbol{x}) = e^{-r^2/\zeta^2}$ which is a Gaussian shape function, where γ and ζ are positive parameters to control the decrease, and ϵ is a small positive constant to prevent division by zero at the origin. A small value of γ will increase the attraction range of the vector field but may cause leakage through weak edges. In contrast, a large value of ζ will increase the attraction range but may smooth out fine object edges. In general, γ can usually be set to 1.5 and ζ can be set to 1.0 for most images. The vector field convolution can then be written as:

$$\boldsymbol{F}(\boldsymbol{x}) = f(\boldsymbol{x}) * \mathbf{k}(\boldsymbol{x}) \tag{3.6}$$

where $f(\boldsymbol{x})$ is the image edge map generated from the image intensity I, and $*$ is the convolution operator. The kernels used in [49] however uses only regional pixels and edge pixels located away from the kernel origin are not included in the computation of the force. The authors showed better initialization and noise insensitivity in their method. However the generated field is static and cannot handle the convergence issues discussed above.

In [116, 127], Xie and Mirmehdi introduced an external force field that is based on the hypothesized magnetic force between the active contour and object boundaries. This formulation has been applied directly in the magnetostatic active contour (MAC) to compute the magnetic field and force required to draw the active contour towards object boundaries in 2D images. This image gradient based method showed significant improvements on convergence issues, e.g. reaching deep concavities, and in handling weak edges and broken boundaries. When applying the analogy directly to deformable modeling, it requires estimation of tangent vectors for the deformable contours, which is convenient in the 2D case, however, not possible in 3D. It will be shown later that the MAC model is in fact a special case of the proposed method in 2D. Xiang *et al.* [128] derived an external force for the active contour based on the elastic interaction (EI) between line defects in solids [129,130], with its long range attraction force similar to the magnetic force used in MAC [116,127]. One of the unique properties of MAC and EI is that they take into account the orientation of image gradient vectors in deriving the external force fields, unlike other edge based approaches, where only image gradient magnitudes are used. It will be shown later that the MAC model is in fact a special case of the proposed method in 2D. The new method does not rely on specific initialization as required in the EI model and handles noise interference much better.

Kimmel [118] also explicitly used image gradient vector directions as an alignment measure in a hybrid approach, coupled with the geodesic active contour and minimal variance criterion suggested by [1]. Given a contour C of length L, and in a parametric form represented by $\boldsymbol{x}(s)$ where s is the arc length, the alignment measure used in [118] is given as

$$E(\boldsymbol{x}) = \int_0^L \left| \nabla I[\boldsymbol{x}(s)] \cdot \hat{\boldsymbol{n}}(s) \right| \mathrm{d}s \tag{3.7}$$

where $\hat{\boldsymbol{n}}(s)$ is the unit normal to contour C at s, $\nabla I(\boldsymbol{x})$ is the image intensity gradient at $\boldsymbol{x}$. The alignment measure is used to optimize the orientation of the curve with respect to the image intensity gradients. This measure, together with the gradient-based geodesic measure and the region-based minimal variance criterion is then used to push or pull the contour towards the image boundary. This hybrid approach, however, requires careful tuning of the different parameters associated with various measures in order to efficiently bridge the image intensity gradient and regional information. In addition, only local edge information are used in the alignment measure, while edge information of pixels located away from the contour are not considered in this technique.

3.3 Proposed Method

Here, a novel external force field is defined based on hypothesized geometrically induced interactions between the relative geometries of the deformable model and the object boundaries (characterized by image intensity gradients). In other words, the magnitude and direction of the interaction forces are based on the relative position and orientation between the geometries of the deformable model and image object boundaries, and hence, it is called the *geometric potential force (GPF)* field. The bidirectionality of the new external force field can facilitate arbitrary cross-boundary initialization, which is a very useful feature to have, especially in the segmentation of complex geometries in 3D. It also improves the performance of the deformable model in handling weak edges, i.e. fuzzy object boundaries in the image. The computation of the new force field utilizes pixels or voxels across the whole image domain, which provides a global view of the image object boundary. In addition, the proposed external force field is dynamic in nature as it changes according to the relative position and orientation between the evolving deformable model and object boundary.

3.3.1 Geometric Potential Force

In order to first deduce the geometric interaction force in 2D, consider a deformable contour C and an ideal object boundary C' in the image plane (see Figure 3.1). Let $\mathrm{d}l$ and $\mathrm{d}l'$ denote the infinitesimal elements of contour C and object boundary C', respectively. In the existing force field based models such as [49,124], the interaction between $\mathrm{d}l$ and $\mathrm{d}l'$ is inversely proportional to the distance separating these two elements and the derived force lies in a straight

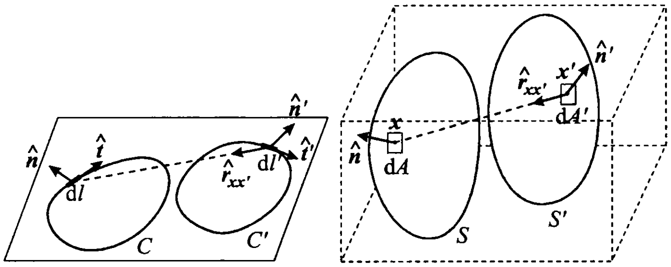

Figure 3.1: Relative position and orientation between geometries in 2D and 3D.

line between them. They do not take into account the local geometry of the deformable contour C or object boundary C'. It is proposed to incorporate the mutual location and orientation of these elements.

Let $\boldsymbol{x}$ and $\boldsymbol{x}'$ denote the positions of elements $\mathrm{d}l$ and $\mathrm{d}l'$, respectively. Thus, $\boldsymbol{r}_{\boldsymbol{x}\boldsymbol{x}'} = \boldsymbol{x} - \boldsymbol{x}'$ is their mutual location of those two elements, $r_{\boldsymbol{x}\boldsymbol{x}'} = |\boldsymbol{x} - \boldsymbol{x}'|$ is the distance between them, and $\hat{\boldsymbol{r}}_{\boldsymbol{x}\boldsymbol{x}'} = (\boldsymbol{x} - \boldsymbol{x}')/r_{\boldsymbol{x}\boldsymbol{x}'}$ is the unit vector pointing to $\mathrm{d}l$ from $\mathrm{d}l'$. The directions of these elements can be represented by their unit tangent vectors $\hat{\boldsymbol{t}}$ and $\hat{\boldsymbol{t}}'$. However, a unique tangent vector is no longer available for infinitesimal surface elements in 3D. Thus, we use unit outward normal vectors $\hat{\boldsymbol{n}}$ and $\hat{\boldsymbol{n}}'$ to characterize the orientations of these elements instead (see Figure 3.1). In 2D, they are simply 90° rotated tangent vectors.

The hypothesized interaction force $\mathrm{d}\mathbf{F}\,\mathrm{d}l$ which acts on element $\mathrm{d}l$ by virtue of the hypothesized force field induced by element $\mathrm{d}l'$ can now be introduced. It is desirable to combine the element orientation vectors and distance vector in deriving the force. A simple but effective combination of these three vectors as $\hat{\boldsymbol{n}}\,(\hat{\boldsymbol{r}}_{\boldsymbol{x}\boldsymbol{x}'} \cdot \hat{\boldsymbol{n}}')$ is proposed, unlike CPM [123] as an example where only the distance vector $\hat{\boldsymbol{r}}_{\boldsymbol{x}\boldsymbol{x}'}$ is used. The multiplication of contour normal $\hat{\boldsymbol{n}}$ ensures that the force is always imposed in the normal direction so that the deformable model does not suffer from convergence issues (i.e. stationary points, saddle points and extreme boundary concavities), which are often associated with other vector force field based methods such as GVF [103]. The dot product of the object boundary element normal with the distance vector allows the force on the contour in the normal direction to diminish as the contour reaches the object boundary. Similar to other physics-inspired force field, it is also desirable to decay the force interaction with the increase of distance between the elements, i.e. the force is designed proportional to $\hat{\boldsymbol{n}}\,(\hat{\boldsymbol{r}}_{\boldsymbol{x}\boldsymbol{x}'} \cdot \hat{\boldsymbol{n}}')/r^{\lambda}_{\boldsymbol{x}\boldsymbol{x}'}$ where $\lambda > 0$. Thus, the contribution of element $\mathrm{d}l'$ of object boundary C' to the total force acting on $\mathrm{d}l$ in accordance with their distance and mutual orientation can be formulated as

$$\mathrm{d}\mathbf{F}\,\mathrm{d}l = \hat{\boldsymbol{n}}\,\mathrm{d}G\,\mathrm{d}l, \qquad \mathrm{d}G = \left(\frac{\hat{\boldsymbol{r}}_{\boldsymbol{x}\boldsymbol{x}'}}{r^{\lambda}_{\boldsymbol{x}\boldsymbol{x}'}} \cdot \hat{\boldsymbol{n}}'\right)\mathrm{d}l' \tag{3.8}$$

where $\mathbf{F}$ is defined as force per unit length, $\mathrm{d}G$ is the contribution of element $\mathrm{d}l'$ of object boundary C' into the scalar field $G(\boldsymbol{x})$, which can be considered as an intermediate potential field, and λ is a positive constant that affects the magnitude of the interaction force based on the distance between the elements. In this study, the best results are obtained when λ coincides with the dimension of the image data, i.e. $\lambda = 2$ in the 2D case. Furthermore, it is shown later that when λ coincides with data dimension in 2D, the proposed force interaction has an explicit link to the magnetostatics theory and thus the spatial decay of the magnitude of the interaction force is analogous to that of the magnetic field.

$\mathrm{d}\mathbf{F}\,\mathrm{d}l = \hat{\boldsymbol{n}}\,\mathrm{d}G\,\mathrm{d}l,$

As shown in Equation (3.8), the computation of the new force field only requires unit normal vectors and relative position of the two elements, which is convenient to acquire. Thus, this new force field can be easily extended to higher dimensions, e.g. 3D. Let $\mathrm{d}A$ belong to the deformable surface S whereas $\mathrm{d}A'$ belongs to the object boundary S' (see Figure 3.1). The generalized 3D version of force $\mathrm{d}\mathbf{F}\,\mathrm{d}A$ acting between these two area elements can be readily given as

$$\mathrm{d}\mathbf{F}\,\mathrm{d}A = \hat{\boldsymbol{n}}\,\mathrm{d}G\,\mathrm{d}A, \qquad \mathrm{d}G = \left(\frac{\hat{\boldsymbol{r}}_{\boldsymbol{x}\boldsymbol{x}'}}{r^{\lambda}_{\boldsymbol{x}\boldsymbol{x}'}} \cdot \hat{\boldsymbol{n}}'\right)\mathrm{d}A' \tag{3.9}$$

where $\mathbf{F}$ is defined as force per unit area, G is the corresponding 3D potential field, $\hat{\boldsymbol{n}}$ and $\boldsymbol{n}'$ are unit surface normals of the deformable model and object boundary, respectively, and $\lambda = 3$. Again, the magnitude and direction of the induced force $\mathbf{F}$ is handled intrinsically by the relative position and orientation between the geometries of the deformable model determined by the evolving surface S and object boundary determined by S'. Since the force is derived geometrically and its interaction is a function of inverse distance, we name it geometric potential force (GPF).

3.3.2 GPF Deformable Model

The GPF force in Equation (3.9) is derived using geometrical information from ideal object boundaries. Next, this is extended to deal with real image data and formulated for 3D deformable modelling. Here, an edge based approach is used, in which the image intensity discontinuity is utilized to estimate the presence and strength of object boundaries.

Let $I(\boldsymbol{x})$ denote the 3D image intensity, where $\boldsymbol{x}$ is a voxel location in the image domain. Temporarily, let $\boldsymbol{x}$ be considered as a continuously varying point. One may treat this as an interpolation between voxel grid points to obtain a continuous image intensity $I(\boldsymbol{x})$. To derive the force acting on $\mathrm{d}A$, the total potential field for an arbitrary point $\boldsymbol{x}$ is first computed as:

$$G(\boldsymbol{x}) = P.V. \oiint_{S'} \mathcal{W}(\boldsymbol{x}') \left(\frac{\hat{\boldsymbol{r}}_{\boldsymbol{x}\boldsymbol{x}'}}{r^{\lambda}_{\boldsymbol{x}\boldsymbol{x}'}} \cdot \hat{\boldsymbol{n}}'(\boldsymbol{x}')\right)\mathrm{d}A'. \tag{3.10}$$

where $\mathcal{W}(\cdot)$ is an image dependent weighting function that is defined later, and *P.V.* means *'Principal Value'*: the contribution of infinitesimal circular vicinity of singular point $\boldsymbol{x}' = \boldsymbol{x}$ into the integral is disregarded, which occurs when surfaces S and S' intersect.

In an ideal continuous image, $I(\boldsymbol{x})$ has a jump at the edge, where ∇I is infinite, and the surface S' is rigorously defined. In a real image, ∇I is a smooth function with its magnitude $|\nabla I|$ reaching its maximum in the vicinity of the object boundary. Thus, instead of the surface integration over S', a volume integral is taken across the image domain. The weighting function $\mathcal{W}$ is set as proportional to the edge strength, which can be estimated as $|\nabla I|$, so that strong edges have larger influence on the generated potential force field than weaker ones, i.e. $\mathcal{W} = |\nabla I|$. In this way, spurious edges which are caused by noise have little effect on the generated force field. Note that $\nabla I = |\nabla I|\,\hat{\boldsymbol{n}}' \equiv \mathcal{W}\,\hat{\boldsymbol{n}}'$. The geometric potential field in the continuous form can then be formulated as

$$G(\boldsymbol{x}) = P.V. \iiint\limits_{\Omega} \left(\frac{\hat{\boldsymbol{r}}_{\boldsymbol{x}\boldsymbol{x}'}}{r^{\lambda}_{\boldsymbol{x}\boldsymbol{x}'}} \cdot \nabla I(\boldsymbol{x}') \right) \mathrm{d}V'. \tag{3.11}$$

where integral is carried out over the image domain Ω. The discrete form of the geometric potential field in Equation (3.11) can be given as

$$G(\boldsymbol{x}) = \sum_{\boldsymbol{x}' \in \Omega, \boldsymbol{x}' \neq \boldsymbol{x}} \left(\frac{\hat{\boldsymbol{r}}_{\boldsymbol{x}\boldsymbol{x}'}}{r^{\lambda}_{\boldsymbol{x}\boldsymbol{x}'}} \cdot \nabla I(\boldsymbol{x}') \right). \tag{3.12}$$

This can be considered as a convolution of the image intensity gradient with the vector kernel $\mathbf{K}_{\lambda}(\boldsymbol{x})$

$$\begin{cases} \mathbf{K}_{\lambda}(\boldsymbol{x}) = P.V. \dfrac{\hat{\boldsymbol{x}}}{|\boldsymbol{x}|^{\lambda}} = P.V. \dfrac{\boldsymbol{x}}{|\boldsymbol{x}|^{\lambda+1}} \\ G = \mathbf{K}_{\lambda} * \nabla I = \displaystyle\iiint\limits_{\Omega} \left(\mathbf{K}_{\lambda}(\boldsymbol{x} - \boldsymbol{x}') \cdot \nabla I(\boldsymbol{x}') \right) dV' \end{cases} \tag{3.13}$$

which can be carried out efficiently using the fast Fourier transform (FFT).

Note that the potential field G is computed as a convolution of two vector functions.

The total force acting on the unit area element of the deformable surface S is thus given as $\mathbf{F} = \hat{\boldsymbol{n}}\, G(\boldsymbol{x})$. where $\hat{\boldsymbol{n}}$ is the outward unit normal of the level set surface. Note, an inward normal can also be used, i.e. $\mathbf{F} = -\hat{\boldsymbol{n}}\, G(\boldsymbol{x})$, which will result in opposite deformable model propagation since the force field is exactly in the opposite direction. An example is given in Figure 3.4. Hence, the force can now be written in a generalized form:

$$\mathbf{F} = \mathcal{J}\hat{\boldsymbol{n}}\, G(\boldsymbol{x}). \tag{3.14}$$

where $\mathcal{J}$ is a constant taking values of ± 1. Note that this is different from the constant force in the geodesic model, where the force is monotonically expanding or shrinking. The sign convention ± is merely used to determine the direction of propagation of the deformable model.

The general contrast consistency along the object boundaries however is important to the model. Large contrast variation can disrupt the force field, e.g. half of the object appears brighter than background and the other half appears to be darker. However, this does not mean that the entire object has to be brighter or darker than background. Those regions away from object boundary can be continuously varying in intensity (see Figure 3.2 as an example).

Once the force field $\mathbf{F}(\boldsymbol{x})$ derived from the hypothesized interactions based on the relative geometries of the deformable model and object boundary is determined, the evolution of the deformable model under this GPF field can be defined. Consider a surface represented implicitly as the zero level set of the function $\phi(\boldsymbol{x}) : \Omega \rightarrow \Re$ such as

$$S = \{\boldsymbol{x} \in \Omega \,|\, \phi(\boldsymbol{x}, t) = 0\} \tag{3.15}$$

where Ω denotes the image domain, and $\phi(\boldsymbol{x}, t)$ denotes the evolving level

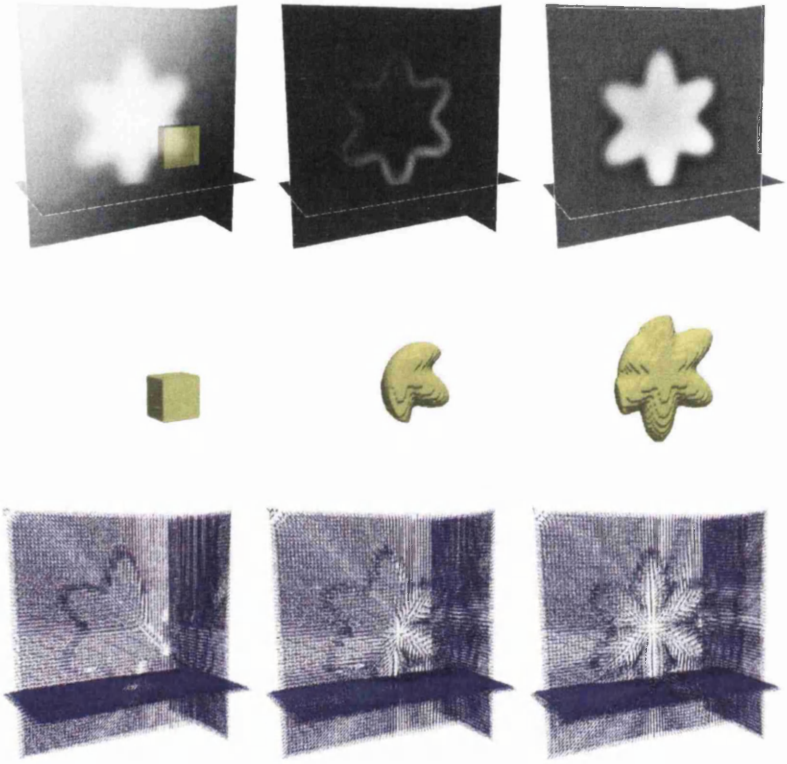

Figure 3.2: GPF: first row from left to right - input image and initial deformable model, corresponding edge map and computed geometric potential field, second row - initial and evolving deformable models, and third row - corresponding GPF vector field.

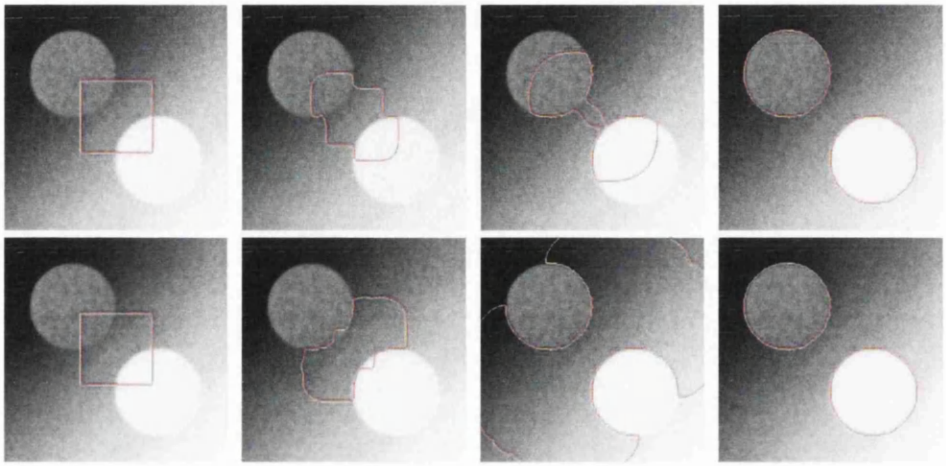

Figure 3.3: Direction of propagation of the GPF deformable model with cross-boundary initialization of the contour: first row - $\mathcal{J} = 1$, second row - $\mathcal{J} = -1$.

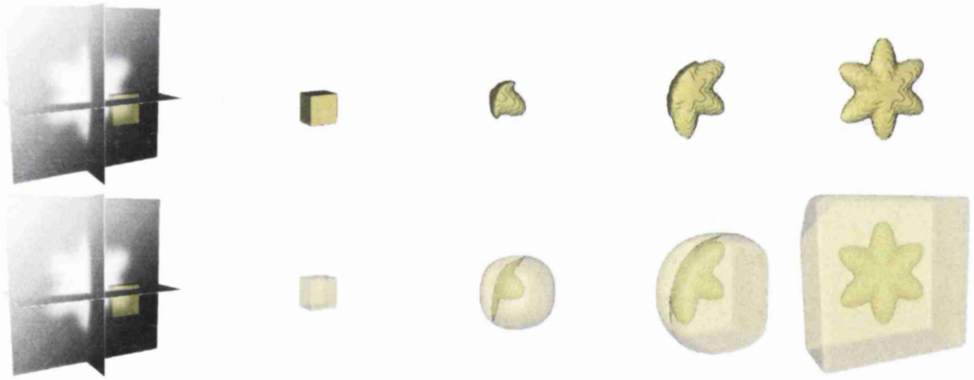

Figure 3.4: Direction of propagation of the GPF deformable model with cross-boundary initialization of the surface: first row - $\mathcal{J} = 1$, second row - $\mathcal{J} = -1$.

set function. The level set representation of the proposed deformable model based on GPF can be formulated as

$$\frac{\partial \phi}{\partial t} = \alpha \, g \, \kappa \, |\nabla \phi| - (1-\alpha)(\mathbf{F} \cdot \nabla \phi) \tag{3.16}$$

where α is a constant parameter, κ is the curvature and $g(\boldsymbol{x}) = 1/(1 + |\nabla I|)$ is the edge stopping function. α controls the amount of smoothness of the contour, for example an increase in α will cause an increase in contour smoothness. As the curvature κ is coupled with the edge stopping function g, the effect of curvature flow will be small in the vicinity of object edges, while the geometric potential force $\mathbf{F}$ in the vicinity of the object edges have large values. Therefore, the model is generally not sensitive to the values of α as the large geometric potential force $\mathbf{F}$ will attract the contours or surfaces to the object boundaries. Note, the GPF force field is defined on the deformable surface, which is implicitly embedded in the level set function, i.e. the force field computed at the propagating front needs to be extended across the computational domain so that the full level set function can be continuously evolved. Although direct force extension method such as the one in [131] can be used, the GPF forces can be conveniently computed for each level set so that this external force is extended to the entire level set function.

The GPF deformable model differs from conventional edge based models by utilizing edge voxel interactions across the whole image, thus providing a more global view of the object boundary. The magnitude of the potential field strength at each image location $\boldsymbol{x}$ is based on the relative position of $\boldsymbol{x}$ with all other voxels in the image. Therefore, voxels at homogeneous regions will also have a non-zero potential field strength. In this way, surfaces which are initialized far away from object boundaries can propagate towards the image edges and converge.

As shown in Equation (3.9), the dot product $\hat{\boldsymbol{r}}_{\boldsymbol{x}\boldsymbol{x}'} \cdot \hat{\boldsymbol{n}}'$ can be both positive and negative, depending on the relative configurations of the geometries between the deformable model and the image boundaries, thus giving a bidirectional vector force field. This useful bidirectionality facilitates arbitrary cross boundary initializations, as its force vectors point towards the object boundary from both ways. This also allows the model to stabilize the deformable surfaces at weak edges, thus preventing leakage. The first row of Figure 3.2 shows a substantially blurred image with linearly varying intensity, and the corresponding edge map and computed geometric potential field. In addition, as the deformable model evolves, the unit vector $\hat{\boldsymbol{r}}_{\boldsymbol{x}\boldsymbol{x}'}$ changes accordingly based on the relative geometries. This contributes to a vector force field that changes dynamically as the deformable model evolves, as depicted in the second row of Figure 3.2. Therefore, the proposed model has much better invariance to its initial position and can deal with complex geometries and extreme boundary concavities.

The physics-based deformable models described in [49, 123–126] and reviewed in Section 3.2 all use a kernel based function to compute the external force field with kernels being decreasing functions of distance from the origin. This is similar to convolving a vector field with the image edge map. For example, forces in Equation (3.5) can be represented as a convolution with the same kernel $\mathbf{K}_\lambda$ in Equation (3.13) with $\lambda = 2$:

$$\mathbf{F}_a(\boldsymbol{x}) = \frac{q}{4\pi\epsilon}\big(\mathbf{K}_\lambda * |\nabla I|\big), \quad \mathbf{F}_r(\boldsymbol{x}) = \frac{q^2}{4\pi\epsilon}\big(\mathbf{K}_\lambda * 1_\Omega\big) \tag{3.17}$$

where $1_\Omega(\boldsymbol{x})$ is a function equal to 1 when $\boldsymbol{x} \in \Omega$ and 0 otherwise. The repelling force $\mathbf{F}_r(\boldsymbol{x})$ is largely imposed in the tangential direction, which has very limited effect on changing the shape or topology of the deformable model. Thus, it is not necessary in the new model. In order to compare with the dominant attraction force $\mathbf{F}_a$, Equations (3.13) and (3.14) are combined and the GPF force is expressed as

$$\mathbf{F}_{\text{GPF}} = \mathcal{J}\hat{\boldsymbol{n}}\big(\mathbf{K}_\lambda * \nabla I\big) \tag{3.18}$$

It is clear that the GPF force is directed by the normal of the deformable model, i.e. it does not contain the tangential 'parasitic' component in contrast to the $\mathbf{F}_a$ force. Moreover, the proposed GPF takes into account edge orientations, as well as edge strength (the convolution in Equation (3.17) is based on a convolution of a vector function on a scalar field; whereas in Equation (3.18) it is carried out on a vector field).

3.3.3 Edge-Preserving Enhancement of Geometric Potential Field Using Non-Local Method

Although the GPF deformable model can reduce its noise sensitivity to a certain extent by modeling gradient vector interactions across the image domain, deformable models based on image gradients are in general susceptible to heavy noise interference. Note, the GPF force $\mathbf{F}$ is determined by its potential G, see Equation (3.14), and G can be pre-computed before evolving the deformable model. Thus, its performance can be improved towards image noise by refining the potential G. Here, it is enhanced using non-local methods [132, 133], so as to increase its robustness even in the presence of a large amount of image noise. One main advantage in choosing non-local methods over local diffusion or averaging methods [134, 135] is the ability to preserve fine structures. Moreover, the potential field has zero or close to zero magnitude in the centre of object boundaries, with positive and negative potential values immediately on either side. Using local methods to carry out smoothing, there is a risk of canceling out on object boundaries, which is not desirable. In non-local methods [132, 133], similarity is not measured based on a single pixel/voxel value but is measured based on the neighborhood of the pixel/voxel. In particular, non-local methods not only compares the intensity value in a single pixel/voxel, but also the geometrical configuration in its neighborhood. This gives a more robust performance than local smoothing filters. In a standard non-local denoising algorithm [132], an image pixel/voxel is restored using the weighted average of all the pixels/voxels in the image. This algorithm, however, cannot be applied directly to the denoising of the geometrically induced potential field G. This is because edge information in the geometric potential field is represented differently from that of the original image. For instance, the gray level values of the original image on the same side of object edges can be quite similar, thus giving a large weight for similarity measure. On the other hand, the difference in magnitudes of the geometric potential field at these regions can however be very large, giving a small weight for similarity measure, causing similar structures to be considered as different. Therefore, instead of comparing voxel neighborhood from the geometric potential field to refine itself, we measure voxel similarity from the original image and use the computed similarity weights to refine the geometric potential.

Given the noisy image with intensity $I(\boldsymbol{x})$ and its corresponding geometric potential field $G(\boldsymbol{x})$, this non-local smoothing of the geometric potential field is carried out by computing a weighted average at each voxel position $\boldsymbol{x}$ according to:

$$G'(\boldsymbol{x}) = \sum_{\boldsymbol{x}' \in \Omega_{\boldsymbol{x}}, \boldsymbol{x}' \neq \boldsymbol{x}} w(\boldsymbol{x}, \boldsymbol{x}')\, G(\boldsymbol{x}) \tag{3.19}$$

where $\Omega_{\boldsymbol{x}}$ is a search window centered around $\boldsymbol{x}$. Following the approach in Buades *et al.* [132], the similarity between two square (2D) or cube (3D) regions centered at location $\boldsymbol{x}$ and $\boldsymbol{x}'$ is measured, and the similarity weight from the image intensity $I(\boldsymbol{x})$ is determined as:

$$w(\boldsymbol{x}, \boldsymbol{x}') = \frac{1}{Z(\boldsymbol{x})} e^{-\frac{1}{h^2}\left(\sum_{\delta \in \boldsymbol{N}} G_\sigma(\delta)(I(\boldsymbol{x}+\delta) - I(\boldsymbol{x}'+\delta))^2 \right)^2} \tag{3.20}$$

where $G_\sigma(.)$ is a Gaussian kernel with standard deviation σ, $\boldsymbol{N}$ denotes the region containing the pixels/voxels location δ, h is the parameter that controls the amount of filtering, and $Z(\boldsymbol{x})$ is a normalization constant given by $Z(\boldsymbol{x}) = \sum_{\boldsymbol{x}' \in \Omega_{\boldsymbol{x}}} w(\boldsymbol{x}, \boldsymbol{x}')$. The parameter h controls the decay of the exponential function and therefore the amount of smoothing. There will be little

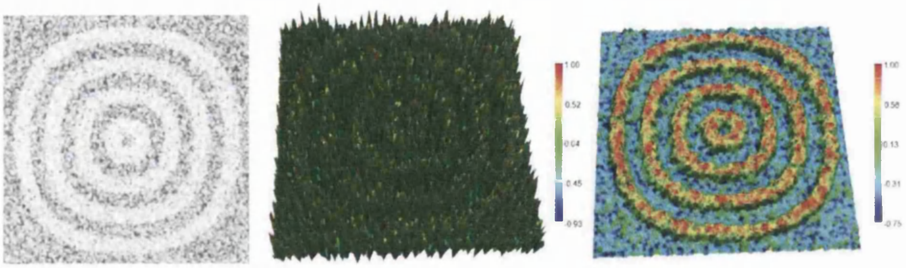

Figure 3.5: Edge-preserving non-local enhancement of geometric potential field: from left - example image with noise, geometric potential field $G(\boldsymbol{x})$ and the corresponding enhanced $G'(\boldsymbol{x})$. Note that $G(\boldsymbol{x})$ and $G'(\boldsymbol{x})$ are shown as 3D surface plots.

smoothing effect if h is too small, and over smoothing of the image if h is too large. In general, h is set proportional to the standard deviation σ, i.e. $h = 1.0\sigma$ to $h = 1.5\sigma$. The force acting due to the enhanced geometrical potential field on the deformable surface S described in Equation (3.14) can then be given as:

$$\begin{aligned}\mathbf{F}(\boldsymbol{x}) &= \mathcal{J}\,\hat{\boldsymbol{n}}(\boldsymbol{x})\,G'(\boldsymbol{x}) \\ &= \mathcal{J}\,\hat{\boldsymbol{n}}(\boldsymbol{x}) \sum_{\boldsymbol{x}'\in\Omega_{\boldsymbol{x}},\boldsymbol{x}'\neq\boldsymbol{x}} w(\boldsymbol{x},\boldsymbol{x}')\,G(\boldsymbol{x})\end{aligned} \tag{3.21}$$

By comparing regional similarity instead of single pixel/voxel similarity from the noisy image, a more reliable geometric potential field is achieved. Moreover, oscillations at flat or homogeneous regions are readily smoothed and edge information at object boundaries are enhanced in the denoised geometric potential field. Figure 3.5 shows a 2D image with 70% added Gaussian noise, the computed geometric potential field $G(\boldsymbol{x})$ and the enhanced $G'(\boldsymbol{x})$ using nonlocal filtering. It is evident that this nonlocal method can efficiently remove noise interference and preserves edge information in the geometric potential field. This greatly enhances the performance of the deformable model in handling image noise. The second row of Figure 3.6 provides the segmentation result on this substantially noise corrupted image using the enhanced geometric potential field.

3.3.4 Relationship with MAC and Comparison with EI Models

In the MAC models [116, 127], the external force field is based on the hypothesized magnetic force between the active contour C and object edge C'. Interaction between two elements $\mathrm{d}l$ and $\mathrm{d}l'$ of contours C and C', respectively, is described in accordance with the Biot-Savart law:

$$\mathrm{d}\mathbf{F}\,\mathrm{d}l = \Upsilon\,\mathrm{d}l\,(\hat{\boldsymbol{t}} \times \mathrm{d}\mathbf{B}), \quad \mathrm{d}\mathbf{B} = \frac{\mu_0}{4\pi}\frac{\Upsilon'\mathrm{d}l'}{r^2_{\boldsymbol{x}'\boldsymbol{x}}}(\hat{\boldsymbol{t}}' \times \hat{\boldsymbol{r}}_{\boldsymbol{x}'\boldsymbol{x}}) \tag{3.22}$$

where Υ and Υ' are electric currents in contours C and C', respectively; $\hat{\boldsymbol{t}}$ and $\hat{\boldsymbol{t}}'$ are unit tangent vectors to elements $\mathrm{d}l$ and $\mathrm{d}l'$, respectively; $r_{\boldsymbol{x}'\boldsymbol{x}}$ is the distance between $\mathrm{d}l$ and $\mathrm{d}l'$, $\hat{\boldsymbol{r}}_{\boldsymbol{x}'\boldsymbol{x}}$ is the unit vector pointing from $\mathrm{d}l'$ to $\mathrm{d}l$, and μ_0 is the permeability constant. The current directions represented by the tangent vectors $\hat{\boldsymbol{t}}$ and $\hat{\boldsymbol{t}}'$ have to be known in advance before computing the magnetic field and force. To deal with this requirement, the authors in [116, 127] compute the direction of the imposed currents for the active contour and object boundary by rotating the respective gradient vectors in a clockwise or anti-clockwise manner such that a current loop is formed on both the active contour and object boundary.

As shown in [116, 127], the MAC method has many advantages when dealing with objects of complicated topology, with noise, and weak edges. However, it is difficult to extend MAC to handle 3D images directly as it is not apparent how the hypothesized current direction is to be estimated and set on a 3D object. Here it is shown that the MAC model is a particular case of the proposed method in 2D.

Notice that tangent vectors $\hat{\boldsymbol{t}}$ and $\hat{\boldsymbol{t}}'$ can be represented as a cross-product of normals $\hat{\boldsymbol{n}}$ and $\hat{\boldsymbol{n}}'$ and the unit vector $\hat{\boldsymbol{z}} = (0,0,1)$ normal to the image plane: $\hat{\boldsymbol{t}} = \hat{\boldsymbol{z}} \times \hat{\boldsymbol{n}}$ and $\hat{\boldsymbol{t}}' = \hat{\boldsymbol{z}} \times \hat{\boldsymbol{n}}'$ (see Figure 3.1). Then applying Lagrange's formula for the vector triple product we obtain

$$\begin{aligned}(\hat{\boldsymbol{z}} \times \hat{\boldsymbol{n}}) \times \mathrm{d}\mathbf{B} &= -\hat{\boldsymbol{z}}\,(\hat{\boldsymbol{n}} \cdot \mathrm{d}\mathbf{B}) + \hat{\boldsymbol{n}}\,(\hat{\boldsymbol{z}} \cdot \mathrm{d}\mathbf{B}) \\ &= \hat{\boldsymbol{n}}\,(\hat{\boldsymbol{z}} \cdot \mathrm{d}\mathbf{B}), \end{aligned} \tag{3.23}$$

$$\begin{aligned}(\hat{\boldsymbol{z}} \times \hat{\boldsymbol{n}}') \times \hat{\boldsymbol{r}}_{\boldsymbol{x}'\boldsymbol{x}} &= -\hat{\boldsymbol{z}}\,(\hat{\boldsymbol{n}}' \cdot \hat{\boldsymbol{r}}_{\boldsymbol{x}'\boldsymbol{x}}) + \hat{\boldsymbol{n}}'\,(\hat{\boldsymbol{z}} \cdot \hat{\boldsymbol{r}}_{\boldsymbol{x}'\boldsymbol{x}}) \\ &= -\hat{\boldsymbol{z}}\,(\hat{\boldsymbol{n}}' \cdot \hat{\boldsymbol{r}}_{\boldsymbol{x}'\boldsymbol{x}}). \end{aligned} \tag{3.24}$$

Now Equation (3.22) can be re-written in the following form (ignoring constants)

$$\mathrm{d}\mathbf{F}\,\mathrm{d}l = \Upsilon\,\mathrm{d}l\,\hat{\boldsymbol{n}}\,\big(\hat{\boldsymbol{z}} \cdot \mathrm{d}\mathbf{B}\big), \quad \mathrm{d}\mathbf{B} = -\frac{\Upsilon'\mathrm{d}l'}{r^2_{\boldsymbol{x}'\boldsymbol{x}}}\hat{\boldsymbol{z}}\,\big(\hat{\boldsymbol{r}}_{\boldsymbol{x}'\boldsymbol{x}} \cdot \hat{\boldsymbol{n}}'\big) \tag{3.25}$$

Note that the magnetic field in the 2D model has only a vertical component: $\mathrm{d}\mathbf{B} = (0,0,\mathrm{d}B) = \mathrm{d}B\,\hat{\boldsymbol{z}}$ where $\mathrm{d}B = \big(\hat{\boldsymbol{z}} \cdot \mathrm{d}\mathbf{B}\big)$. Hence, by setting $\mathrm{d}B = \mathrm{d}G$, $\Upsilon = 1$ and $\Upsilon' = 1$ and also taking into account that $\hat{\boldsymbol{r}}_{\boldsymbol{x}'\boldsymbol{x}} = -\hat{\boldsymbol{r}}_{\boldsymbol{x}\boldsymbol{x}'}$ and $r_{\boldsymbol{x}'\boldsymbol{x}} = r_{\boldsymbol{x}\boldsymbol{x}'}$, it will lead one to the 2D GPF model as in Equation (3.8) with $\lambda = 2$. If one set $\Upsilon = \mathcal{J}$ and $\Upsilon' = |\nabla I|$, this will show that the image intensity gradient based MAC model is equivalent to the proposed image intensity gradient weighted GPF in 2D as given in Equations (3.12) and (3.14), again with $\lambda = 2$. Thus, one can consider the proposed method as a generalization of the MAC method [116] to higher dimensions or, in other words, the MAC method is a special case of GPF in 2D.

The force field used in the EI model [30, 128] is defined based on the elastic interaction between line defects and can be given as:

$$\tilde{\boldsymbol{v}} = P.V. \oiint_{\Omega} \frac{\hat{\boldsymbol{r}}_{\boldsymbol{x}\boldsymbol{x}'}}{r^2_{\boldsymbol{x}\boldsymbol{x}'}} \cdot \nabla(G_\sigma * I + \nu_c \mathcal{H}_\epsilon(\phi))\,\mathrm{d}A \tag{3.26}$$

where $\boldsymbol{x}$ and $\boldsymbol{x}'$ are points on the moving contour and on the object boundary, respectively, G_σ is a Gaussian kernel with standard deviation σ, ν_c is an

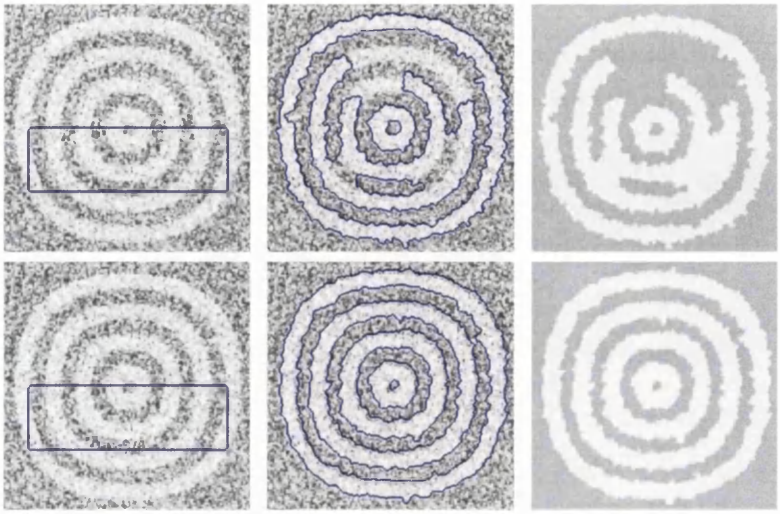

Figure 3.6: Comparative results of the segmentation of concentric rings from noisy image - first row: EI model; second row: proposed GPF model.

adjustable coefficient, and $\mathcal{H}_\epsilon$ is a smoothed Heaviside function. The elastic interaction force $\tilde{\boldsymbol{v}}$ in Equation (3.26) consists of an image based interaction force and a contour based interaction force. The image based interaction is given by the dot product $\left(\hat{\boldsymbol{r}}_{\boldsymbol{x}\boldsymbol{x}'}/r^2_{\boldsymbol{x}\boldsymbol{x}'}\right) \cdot \nabla(G_\sigma * I)$ and takes a similar form to the proposed geometric interactions. The term $\left(\hat{\boldsymbol{r}}_{\boldsymbol{x}\boldsymbol{x}'}/r^2_{\boldsymbol{x}\boldsymbol{x}'}\right) \cdot \nabla(\nu_c \mathcal{H}_\epsilon(\phi))$ represents the contour based interaction within the moving contour.

The EI model initializes the contour using the zero-crossing of the image based interaction force, which sets the initial contour near the object boundary. This also generates many false contours caused by spurious edges. It is assumed that the force generated by the noise is relatively small as compared to the interaction force at the object boundary. The EI model then uses the contour based interaction force within the evolving contour to overcome the interaction between the noise and the contour. The parameter ν_c thus needs to be sufficiently large in order to shrink the spurious edges caused by the noise. This initialization strategy, however, is only suitable when the user intends to extract all the objects in the image. It is therefore not appropriate to use this initialization technique to extract a single object from multiple objects that exist in the image. For example, in order to segment the aorta and the femoral bone from the medical images shown in Figure 3.16 and Figure 3.20 respectively, the user should be able to place the initial contour or surface inside, outside or across the feature of interest. However, with a user-defined initialization, it is difficult to select the parameter ν_c, since a small ν_c may not be able to handle the image noise, and a large ν_c may overwhelm weak edges and the deformable model may not be able to propagate through boundary concavities as an example. It is also noted that the curvature flow used in the formulation of the EI model is not coupled with an edge stopping function which generally exists in geometric deformable models. The weighting for the curvature term in the EI model can be set to a large value, so as to have significant influence on the contour evolution and to overcome the noise. However, without the edge stopping function, a large curvature force may easily overwhelm weak edges or even shrink the correct contour at the object boundary. Moreover, the computation of the contour based interaction force is required at every time step during the contour evolution. Although this can be accelerated by using fast Fourier transform (FFT), it still requires a significant amount of computational effort, especially when dealing with 3D images.

The proposed method, however, does not rely on any specific initialization strategy. The deformable model can be placed to localize single or multiple regions of interest with arbitrary cross boundary initializations. Compared to EI, it is more effective in removing noise interference and more efficient in evolving the deformable model. Figure 3.6 gives such an example. A heavily noise corrupted image containing concentric rings with a cross boundary initialization is used for the test. It is shown that the EI model has difficulties in finding the right balance in overcoming the image noise and propagating the contour further. The proposed method evolves much more efficiently and achieves a much better result.

3.3.5 Implementation and Setting of Parameters

The image object boundary description used in the computation of $G(\boldsymbol{x})$ can be acquired from the derivatives of the image intensity using central difference, or standard edge detection methods such as the Sobel filter which estimates the image derivatives using convolution kernels designed to respond maximally to edges in the x, y and z directions. Some spurious edges can be removed by excluding edges with very small magnitude, i.e. 5% - 10% of the maximum magnitude.

The level set evolution in Equation (3.16) is solved numerically by the finite difference method. Let $\boldsymbol{x}_{ijk} = [x_i, y_j, z_k]^T = [i\Delta x, j\Delta y, k\Delta z]^T$ be the grid point where Δx, Δy and Δz are the grid steps along the x, y and z directions respectively (i.e. voxel size in each direction). Let Δt be a time step, so $t_n = n\Delta t$ where $n \geq 0$. The level set function $\phi(x, y, z, t)$ is then given on the time-space grid as:

$$\phi_{ijk}^{n} = \phi(x_i, y_j, z_k, t_n) \tag{3.27}$$

The forward Euler method is used for time discretization:

$$\phi_{ijk}^{n+1} = \phi_{ijk}^{n} + \Delta t\{\alpha\ (g\,\kappa\ |\nabla\phi|)_{ijk}^{n} - (1-\alpha)(\boldsymbol{F}\cdot\nabla\phi)_{i,j,k}^{n}\} \tag{3.28}$$

In the curvature term $\left(g\,\kappa|\nabla\phi|\right)$ in Equation (3.28), all the derivatives such as $\partial\phi/\partial x$, $\partial I/\partial x$, $\partial\phi/\partial y$, etc., are approximated using central differences, i.e. $(\partial\phi/\partial x)_{ijk} \approx [\phi_{i+1,j,k} - \phi_{i-1,j,k}]/(2\Delta x)$, and so on. The vector force term $\left(\boldsymbol{F}\cdot\nabla\phi\right)$ in Equation (3.28) is computed using the upwind difference scheme which can be expressed as:

$$(\boldsymbol{F}\cdot\nabla\phi)_{i,j,k}^{n}) = \left(F_x\frac{\partial\phi}{\partial x}\right)_{i,j,k}^{n} + \left(F_y\frac{\partial\phi}{\partial y}\right)_{i,j,k}^{n} + \left(F_z\frac{\partial\phi}{\partial z}\right)_{i,j,k}^{n} \tag{3.29}$$

where the components in the x, y and z directions are given as:

$$\left(F_x\frac{\partial\phi}{\partial x}\right)^n_{i,j,k} \approx \begin{cases} F_x^n\dfrac{\phi^n_{i,j,k}-\phi^n_{i-1,j,k}}{\Delta x} & \text{if} \quad F_x^n > 0 \\ F_x^n\dfrac{\phi^n_{i+1,j,k}-\phi^n_{i,j,k}}{\Delta x} & \text{if} \quad F_x^n < 0 \end{cases} \tag{3.30}$$

$$\left(F_y\frac{\partial\phi}{\partial y}\right)^n_{i,j,k} \approx \begin{cases} F_y^n\dfrac{\phi^n_{i,j,k}-\phi^n_{i,j-1,k}}{\Delta y} & \text{if} \quad F_y^n > 0 \\ F_y^n\dfrac{\phi^n_{i,j+1,k}-\phi^n_{i,j,k}}{\Delta y} & \text{if} \quad F_y^n < 0 \end{cases} \tag{3.31}$$

$$\left(F_z\frac{\partial\phi}{\partial z}\right)^n_{i,j,k} \approx \begin{cases} F_z^n\dfrac{\phi^n_{i,j,k}-\phi^n_{i,j,k-1}}{\Delta z} & \text{if} \quad F_z^n > 0 \\ F_z^n\dfrac{\phi^n_{i,j,k+1}-\phi^n_{i,j,k}}{\Delta z} & \text{if} \quad F_z^n < 0 \end{cases} \tag{3.32}$$

The initial contour or surface can be defined arbitrarily inside, outside or across the boundary of the image object to be segmented. An initial level set function is defined as a signed distance function $\mathsf{D}[S_0]$ from the initial surface S_0:

$$\phi(x_i, y_j, z_k, 0) = \mathsf{D}\left[S_0\right] \tag{3.33}$$

The signed distance function can be computed efficiently using the distance transform algorithm described in [9]. In this approach, the squared Euclidean distance is computed as a minimum convolution of a sampled function and a parabola. The Neumann boundary conditions are imposed at the boundaries of the image domain. The isosurface of the level set function is extracted and rendered using the marching cubes algorithm [136, 137]. The Narrow Band approach described in [25] is used to reduce the computational cost in updating the level set function .

During the numerical computation, the level set function ϕ can become irregular. Therefore, it is periodically reinitialised to the signed distance function from the current zero level set (surface of the deformable model), $S(t) = \{\boldsymbol{x} : \phi(\boldsymbol{x}, t) = 0\}$. Hence, ϕ can be denoted as $\phi(\boldsymbol{x}, t) = \mathsf{D}[S(t)]$, which is a smooth function with $S(t)$ as the zero level set.

As mentioned in Section 3.3.2, $\mathcal{J} = \pm 1$ can be used to determine the direction of propagation of the deformable model. In particular, the deformable model will extract relatively brighter voxels from an image region when $\mathcal{J} = 1$, and extract the darker voxels when $\mathcal{J} = -1$ as shown in Figure 3.3 and Figure 3.4. However, as shown in Figure 3.3 and Figure 3.4, the deformable model will often converge to the same object geometry with a cross-boundary initialization. α is a constant parameter that controls the smoothness of the contour, and is generally set to a small value in the experiments, i.e. $\alpha = 10^{-3}$.

The enhancement of the geometric potential field using nonlocal method can be computationally expensive a search window $\Omega_{\boldsymbol{x}}$ of size similar to that of the image is used. For computational purposes, a search window of 21×21 pixels for 2D images as suggested in [132] and $21 \times 21 \times 21$ voxels for 3D images are generally sufficient for most images, and a square or cube similarity neighborhood region $\boldsymbol{N}$ of length 7 for 2D and 3D images is usually large enough for noise robustness and small enough to preserve fine structures and details [132]. In addition, the nonlocal filtering can be accelerated using efficient algorithms such as the combination of summed square image scheme and FFT used in [138], and the vectorization and parallelization strategy described in [133]. The parameter h in Equation (3.20) controls the amount of filtering which depends on the amount of noise present in the image, and is generally set proportional to the standard deviation σ, i.e. $h = 1.0\sigma$ to $h = 1.5\sigma$. Note that refining of the geometric potential field is only necessary when the noise presence is significant such as the example shown in Figure 3.13. The proposed GPF model can handle considerable amount of image noise as the geometric potential field is computed using edge pixel or voxel interactions across the whole image.

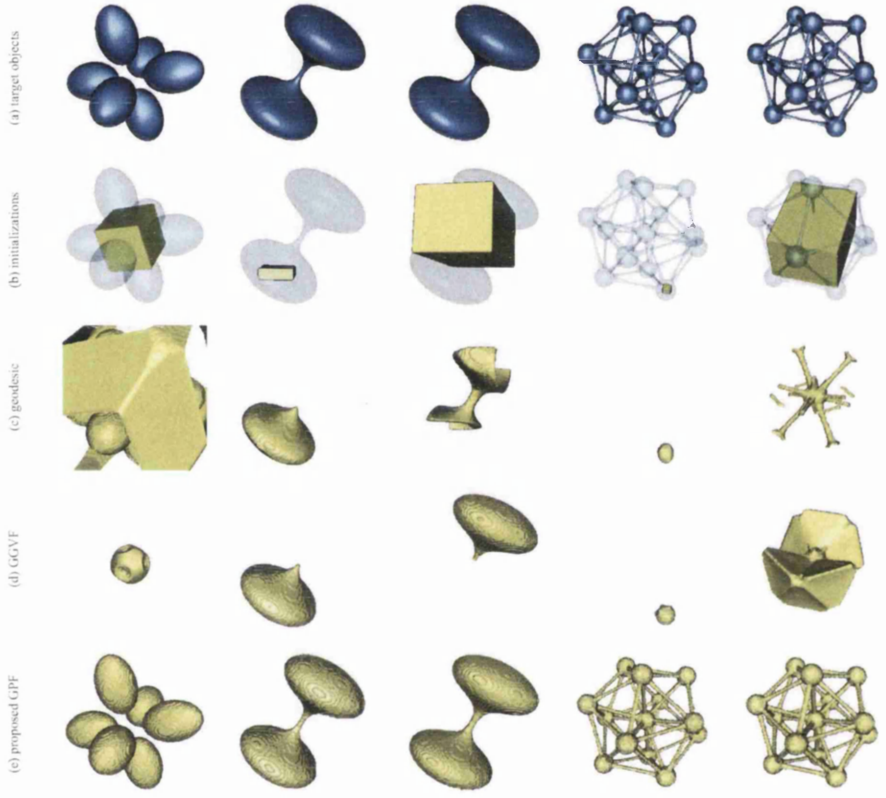

Figure 3.7: Shape recovery from synthetic images: (a) isosurfaces of various shapes to be recovered from synthetic images (128×128×128), (b) initial deformable models (yellow) with input shapes (blue, semi-transparent), (c) recovered shape using geodesic, (d) GGVF, (e) proposed GPF

3.4 Results and Discussion

In this section, experimental results on both synthetic and real image data are presented. The algorithms are implemented in C++, and the computations are performed on an Intel Core 2 Duo 3.00GHz processor with 4GB RAM. The comparative analysis is performed using several classical and state-of-the-art methods which consists of image intensity gradient based and region based methods. In particular, the geodesic model [29] is included as a representative of conventional local edge fitting based method with monotonically expanding or shrinking force. The various vector field based models, such as [49, 123–126], have very similar convergence and initialization dependence behavior to the GVF [103] or GGVF [13], due to their dominant external forces being static as discussed earlier. Thus, the GGVF [13] model is used as a representative of vector force field based approaches. In addition, the Chan-Vese model [1] with its region based formulation, and the more recent EI model [30] which uses a dynamic vector force, are also included in the analysis. The geodesic, GGVF, EI and Chan-Vese models are implemented according to the algorithms described in the papers [1, 13, 29, 30]. In the experiments, the parameters used for the various models are first selected based on the values recommended in the papers when appropriate, and when necessary, a range of values for the parameters are used to tune the models such that the best outcomes for each model are selected to ensure a fair comparison.

3.4.1 Multiple Objects

The first column in Figure 3.7 shows the shape extraction results for the six-ellipsoids problem. Given an arbitrary initialization across all the ellipsoids, only GPF could accurately recover the shapes. The geodesic model, given the same initialization configuration, simply expanded outwards and reached the image borders. This is due to the fact that the geodesic model cannot handle cross-boundary initialization as the constant pressure term can only monotonically shrink or expand the contour. Although the bidirectionality of the GGVF model enables it to handle cross-boundary initialization, the saddle and stationary points in this example prevented GGVF from extracting the ellipsoids.

3.4.2 Convergence to Boundary Concavities

Next, we compare the ability of the deformable models to deal with highly concave boundaries. As shown in the second and third columns in Figure 3.7, the geometrical object to be recovered consists of two flattened ellipsoids connected by a narrowing tube with a constriction in the middle. With the deformable models initialized inside one of the ellipsoid, only GPF could propagate through the narrowing tube to accurately extract the shape. Also, with a more arbitrary cross-boundary initialization, GPF was the only successful model to extract the exact shape. The other two methods could neither handle the arbitrary initialization nor propagate through deep concavities. Note that the bottleneck between the two ellipsoids is extremely narrow, which makes it particularly difficult for the geodesic model to propagate through without stepping through the object boundary due to the large expansion force.

3.4.3 Handling Complex Geometries and Topologies

The fourth and fifth columns in Figure 3.7 compare the shape extraction results on a complex geometry with different initialization configurations. When the initial surface is placed inside one of the sphere of the molecular structure, GPF is the only model that managed to extract the geometry successfully. The other two models were not able to propagate through the long narrow tubes connecting the spheres. With a cross-boundary initialization, the geodesic model only recovered part of the geometry with a negative pres-

Table 3.1: Comparative results on the segmentation of various shapes from synthetic images: Foreground (FG), background (BG) and overall accuracy measured in %.

		Geodesic	GGVF	GPF
Six-ellipsoids cross initialization	FG (%)	93.9	0.20	99.9
	BG (%)	0.15	99.3	100
	Overall (%)	47.0	49.7	**99.9**
Ellipsoids with narrowing tube inside initialization	FG (%)	41.7	48.5	99.5
	BG (%)	100	100	100
	Overall (%)	70.8	74.2	**99.8**
Ellipsoids with narrowing tube cross initialization	FG (%)	3.79	48.5	99.5
	BG (%)	99.8	100	100
	Overall (%)	51.8	74.2	**99.8**
Molecular inside initialization	FG (%)	4.73	5.51	99.9
	BG (%)	100	100	99.7
	Overall (%)	52.4	52.8	**99.8**
Molecular cross initialization	FG (%)	12.0	10.6	100
	BG (%)	99.8	95.6	99.7
	Overall (%)	55.9	53.1	**99.8**
FG Average (%)		31.2	22.7	**99.8**
BG Average (%)		80.0	99.0	**99.9**
Overall Average (%)		55.6	60.8	**99.8**

sure force, while GGVF converges to the wrong shape due to the saddle and stationary regions in the complex geometry.

The above examples demonstrate the superior performance of the GPF deformable model in resolving deep concavities and handling complex geometries and topologies. This is mainly due to the dynamic nature of the vector force field. In addition, we show that the bidirectionality of the new force field gives GPF the flexibility to deal with arbitrary cross-initializations.

Table 3.1 presents the comparative results for the recovery of various shapes shown in Figure 3.7. The foreground (FG) and background (BG) accuracy of the extracted shapes are measured as the percentages of true foreground and background voxels which were actually segmented as foreground and background respectively, i.e. $\mathrm{FG} = \frac{\mathrm{TP}}{N_{\mathrm{FG}}}$ and $\mathrm{BG} = \frac{\mathrm{TN}}{N_{\mathrm{BG}}}$, where the number of true positives (TP) and true negatives (TN) are denoted by the number of correctly classified foreground and background voxels respectively. N_{FG} and N_{BG} denote the number of true foreground and background voxels. Note that each of the synthetic images used in the examples shown in Figure 3.7 has an image size of 128^3 voxels, and contains a relatively large number of background voxels compared to the foreground voxels, e.g. the percentages of foreground and background voxels in the six-ellipsoids images are 7.60% and 92.4% respectively. Therefore, a normalized overall accuracy given as the average of FG and BG (i.e. overall accuracy $= \frac{\mathrm{FG}+\mathrm{BG}}{2}$) is used to measure the accuracy of correctly extracted voxels from the image, so as to prevent measurement bias towards the large number of background voxels. Note that FG and BG do not take into account the number of misclassified voxels, and represent only the percentages of correctly classified voxels. For example, a high value in FG does not necessarily mean that the extracted geometry has high accuracy, as there may be a large number of misclassified background voxels, i.e. the Geodesic model in the extraction of multiple ellipsoids. Therefore, FG and BG should be viewed together with the overall accuracy to give a good indication of the accuracy of the extracted geometries. The geodesic model is shown to give an average FG and BG accuracy of 31.2% and 80.0% respectively, and an average overall accuracy of 55.6%. The GGVF model provides an average FG accuracy of 22.7%, an average BG accuracy of 99.0% and an overall average of 60.8%. The GPF model clearly outperforms the others with a significantly higher FG and BG average accuracy of 99.8% and 99.9% respectively, and an overall average of 99.8%.

3.4.4 Localization of Objects from Varying Intensity

The region based techniques such as the Chan-Vese model often assume that image objects consist of distinct characteristics, and are therefore sensitive to

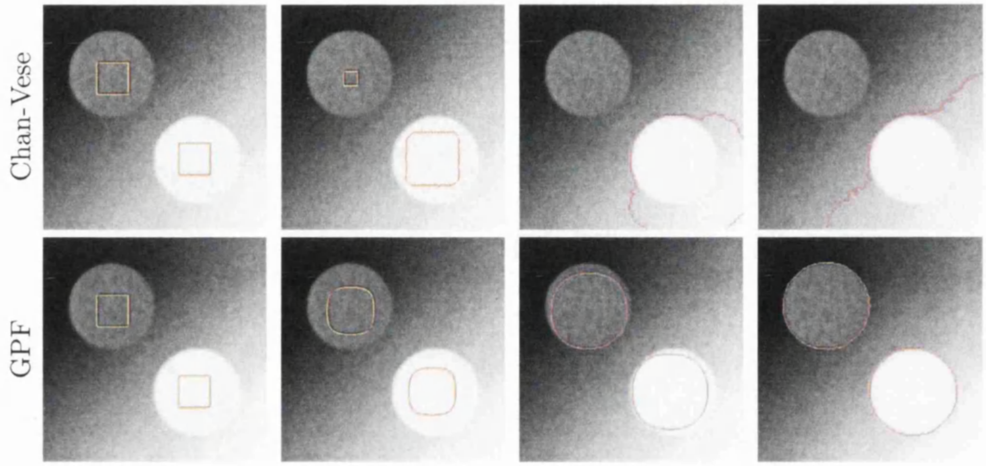

Figure 3.8: Localization of objects from images with intensity inhomogeneity: (top row) Chan-Vese and (bottom row) GPF with contour initialization inside object boundaries.

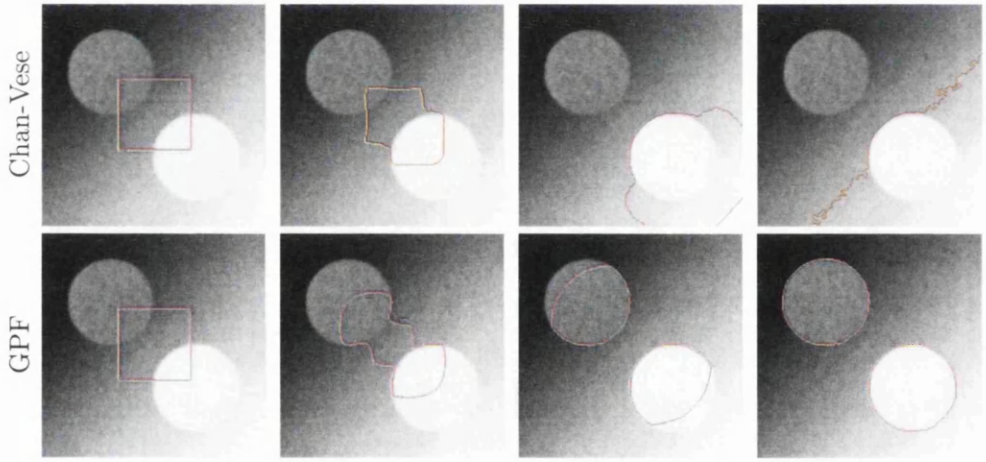

Figure 3.9: Localization of objects from images with intensity inhomogeneity: (top row) Chan-Vese and (bottom row) GPF with contour initialization across object boundaries.

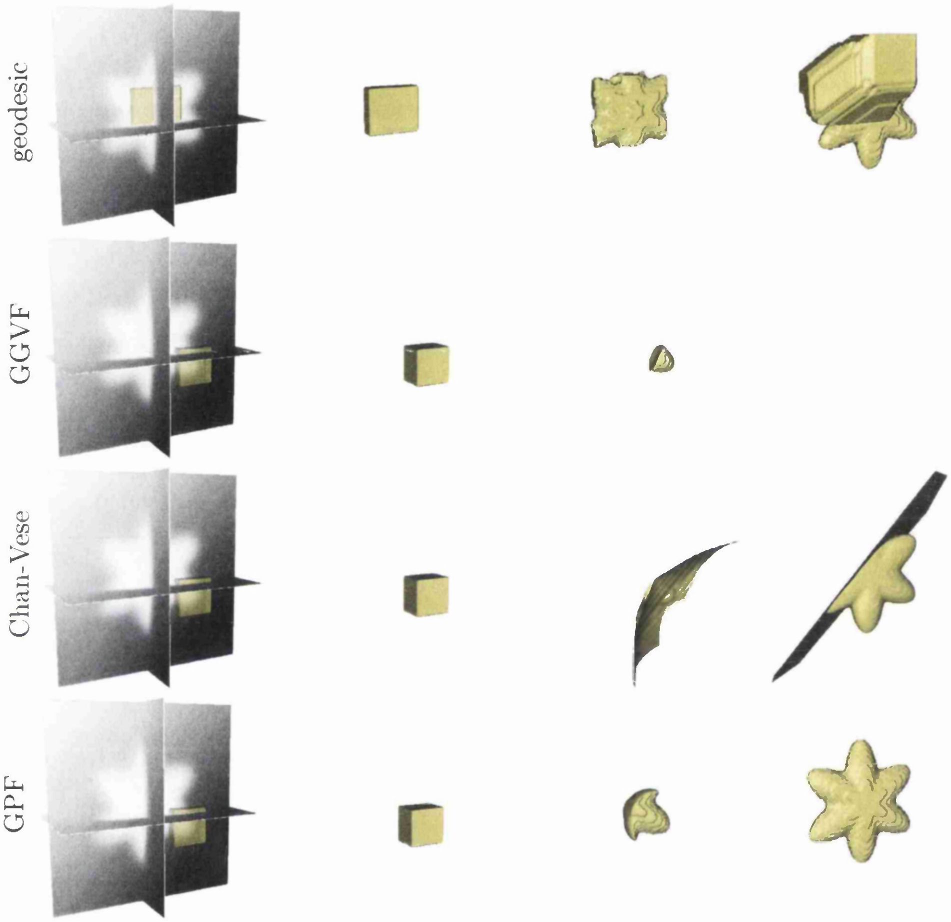

Figure 3.10: Shape recovery from weak edges - first row: geodesic; second row: GGVF; third row: Chan-Vese; fourth row: proposed GPF.

intensity inhomogeneity. Although the GPF model is computed using pixels or voxels across the image, it is derived from image intensity gradient information. It is therefore robust to smooth intensity variation in images. Figure 3.8 depicts the segmentation of disc objects from an image with intensity inhomogeneity using deformable models with the initial contours placed inside the object boundaries. As shown in the figure, the Chan-Vese contour inside the darker region shrinks, while the contour in the brighter region expands and leaks out of the object boundaries. In contrast, the GPF model located the object boundaries accurately. Figure 3.9 shows the segmentation of the discs objects with cross-boundary initialization. As shown, the Chan-Vese model has difficulties handling the intensity variation, while the GPF model converges to the object boundaries efficiently.

3.4.5 Recovery of Weak Object Boundaries

Figure 3.10 shows a harmonic shape with smoothly varying image intensity and substantially diffused or blurred boundary segment. The geodesic model with the initial surface placed inside the object as shown in the first row, leaks through the weak edge. The GGVF model, due to the bidirectionality of its force field, can converge to the weak edge with careful initialization. However, a more arbitrary cross-boundary initialization causes the GGVF model to collapse as shown in the second row. The Chan-Vese model has difficulties in propagating across the image due to intensity inhomogeneity as shown in the third row of Figure 3.10. The GPF, on the other hand, can efficiently localize the object despite the weak boundary, intensity inhomogeneity, and cross-boundary initialization, as shown in the last row.

3.4.6 Invariance to Initialization

The bidirectional and dynamic force field gives the GPF model a high invariance to various arbitrary initializations, therefore providing a high con-

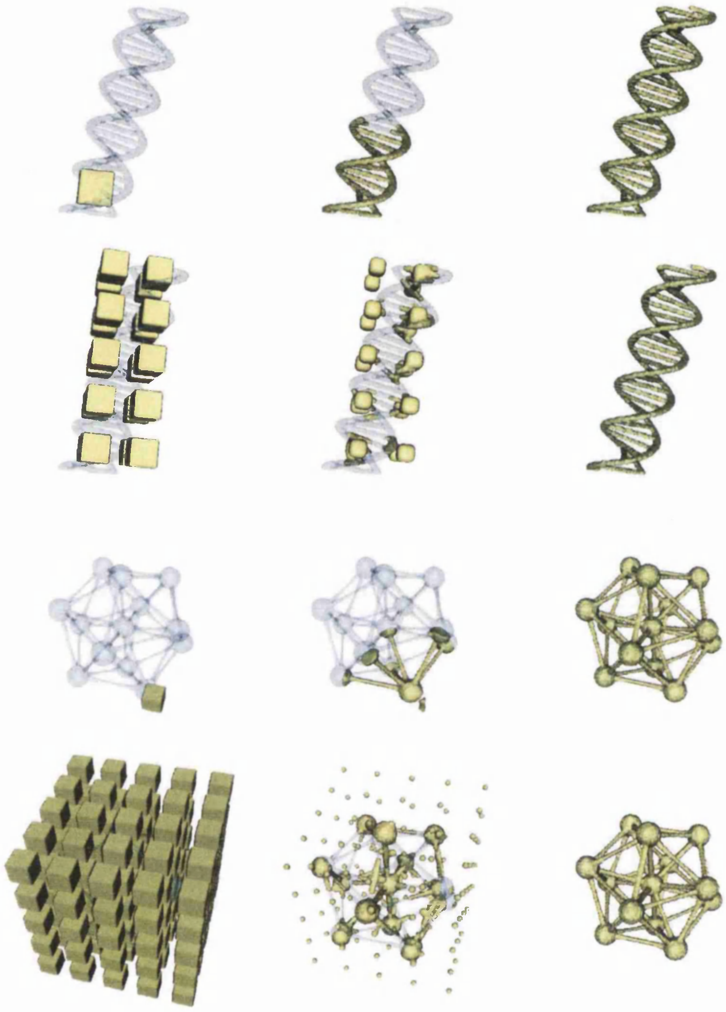

Figure 3.11: Arbitrary initialization using GPF (yellow - deformable surfaces, semi-transparent blue - isosurfaces from synthetic images): First and second rows: double helix shape segmentation using different initializations. Third and fourth rows: molecular shape segmentation using different initializations.

Figure 3.12: Shape recovery from noisy image - from left: noisy image, isosurface with initialization (yellow), and recovered shape using the GPF model.

sistency in segmentation results. For example in Figure 3.7, the geodesic and GGVF models both give very different segmentation results when the models are initialized differently. Conversely, the GPF model converged to the correct object boundaries given different initializations. More arbitrary initializations are used in the complex geometries in Figure 3.11 to further illustrate the initialization invariance of the GPF model. In the first and third rows of Figure 3.11, the initial surface is placed across one end of the double helix shape and molecular structure respectively. In the second and fourth rows of Figure 3.11, a uniformly distributed initialization is used to segment the complex geometries. No discernable difference is found in the results produced through different initializations.

3.4.7 Robustness to Image Noise

As the geometric potential field is computed using edge voxel interactions across the whole image, it provides a more global view of the object boundary representation. This makes the GPF model more robust to image noise compared to other models which use only local image intensity gradient information. In addition, the edge-preserving denoising of the geometric potential field described in Section 3.3.3 can significantly reduce its sensitivity to noise.

Figure 3.12 shows the robustness of the GPF model on image noise, using the geometric potential field computed directly from the noisy image

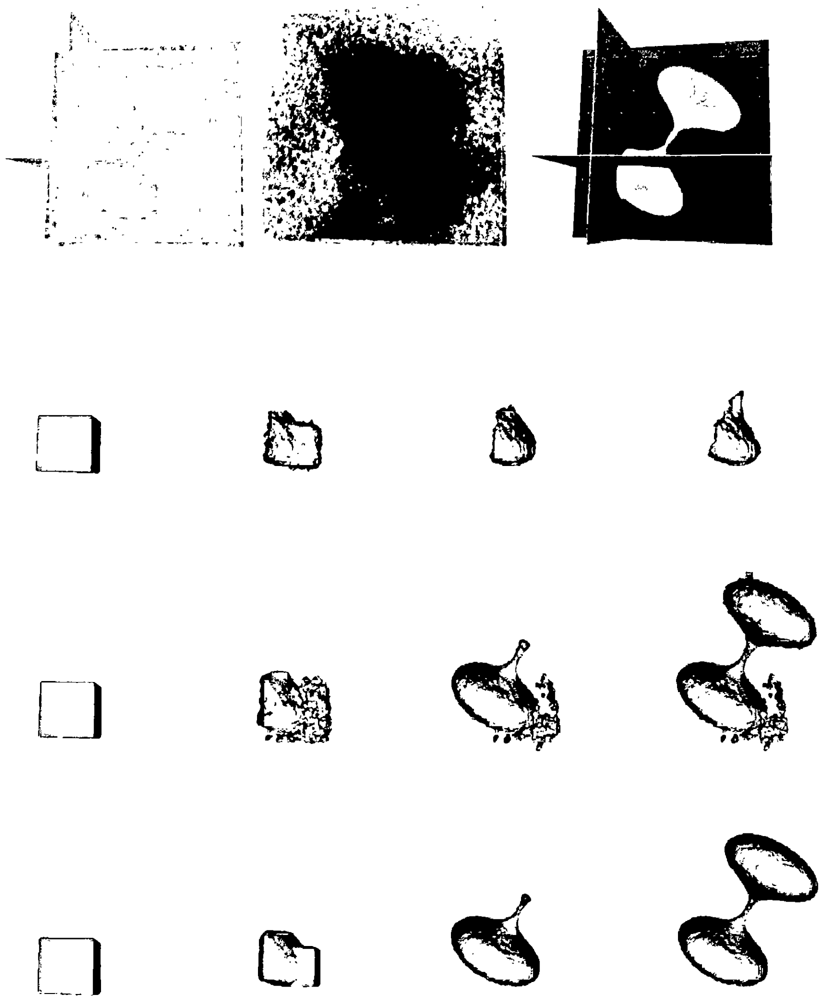

Figure 3.13: Shape recovery using edge-preserving nonlocal enhancement of geometric potential field - first row: noisy image (128×128×128), isosurface with initialization (yellow), and denoised geometric potential field using nonlocal method; second row: evolving deformable surfaces using the EI model (CPU-time, 109590s); third row: evolving deformable surfaces using the GPF model with original geometric potential field from noisy image (CPU-time, 1846s); fourth row: evolving deformable surfaces using the GPF model with denoised geometric potential field using nonlocal method (CPU-time, 932s).

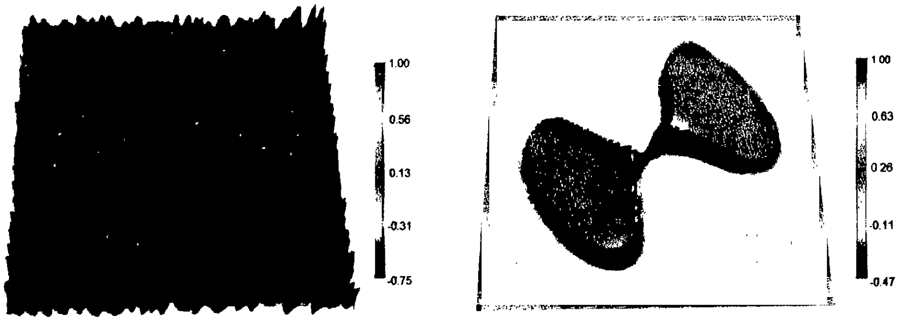

Figure 3.14: Edge-preserving nonlocal denoising of geometric potential field - left: geometric potential field (normalized) of noisy image before nonlocal denoising; right: geometric potential field (normalized) of noisy image with nonlocal denoising.

(i.e. without denoising). It accurately extracted the shape from the noisy image. Note the substantial amount of noise made it difficult for the marching cubes based algorithm to render the target object (cf. Figure 3.7). Figure 3.13 illustrates the increase in noise robustness of the GPF model, using the nonlocal denoising algorithm on the geometric potential field. In this particular example, a considerable amount of non-uniform noise was further added to the noisy image from Figure 3.12. As depicted in Figure 3.13, the substantial amount of noise added produces some localized noise concentration or artifacts. Although the EI model with its contour based interaction force can shrink the spurious edges caused by the large amount of noise, it prevented the deformable model from propagating across the image object. A smaller weight for the contour based force will result in numerous erroneous regions. The deformable model using the potential field computed directly from the noisy image managed to extract the foreground object, but it also produced some erroneous edges. On the other hand, an enhanced geometric potential field using the nonlocal method greatly increases the accuracy of the deformable model in segmenting the object from the noisy image. Note that no filtering such as Gaussian or anisotropic smoothing was applied. The

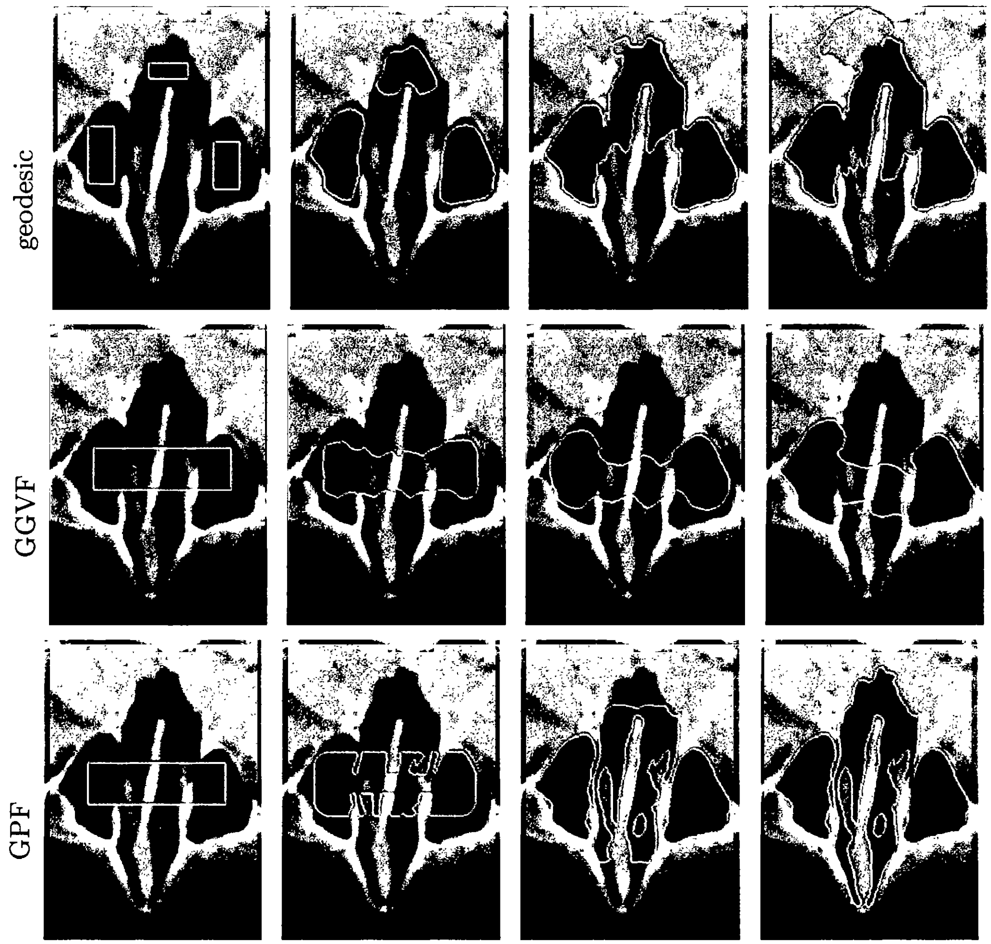

Figure 3.15: Segmentation of the nasal cavity from CT image using different deformable models - first row: geodesic; second row: GGVF; third row: proposed GPF.

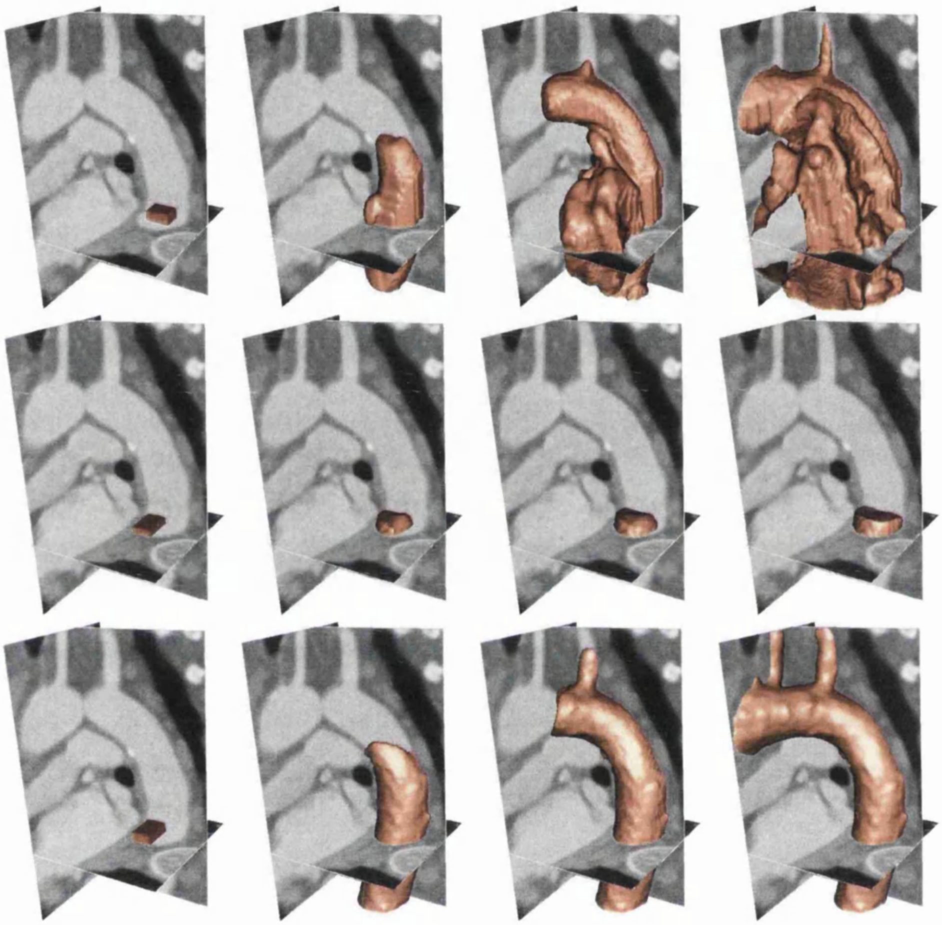

Figure 3.16: Segmentation of human aorta from CT image dataset (64×64×128) using different deformable models - first row: geodesic (CPU-time, 2416s); second row: GGVF (CPU-time, 104s); third row: proposed GPF (CPU-time, 1388s).

Figure 3.17: Comparison of recovered geometries (orange) with manual segmentation (blue) - from left: reconstructed geometry from manual segmentation, comparison of manual segmentation with geometry recovered using geodesic model, comparison of manual segmentation with GGVF model, comparison of manual segmentation with Chan-Vese model, and comparison of manual segmentation with the proposed GPF model.

EI model took 109590s to converge in this example due to the high computation cost of its contour based interaction force at each iteration, while the GPF model achieved a much faster convergence using 1846s and 932s with the original and denoised geometric potential field respectively. Figure 3.14 compares the profiles of the geometric potential field before and after nonlocal denoising. The noise fluctuation shown in the original profile of geometric potential field can introduce some false edges to the segmentation. However, the nonlocal denoising method described previously can remove the noise interference and enhance the true object boundary information.

3.4.8 Segmentation of Real Images

Real images often contain complex geometries and topologies, image noise and weak edges. Here, some comparative results on the segmentation of medical image data are shown. Figure 3.15 shows the segmentation of the nasal cavity from computed tomography (CT) images. The geodesic model

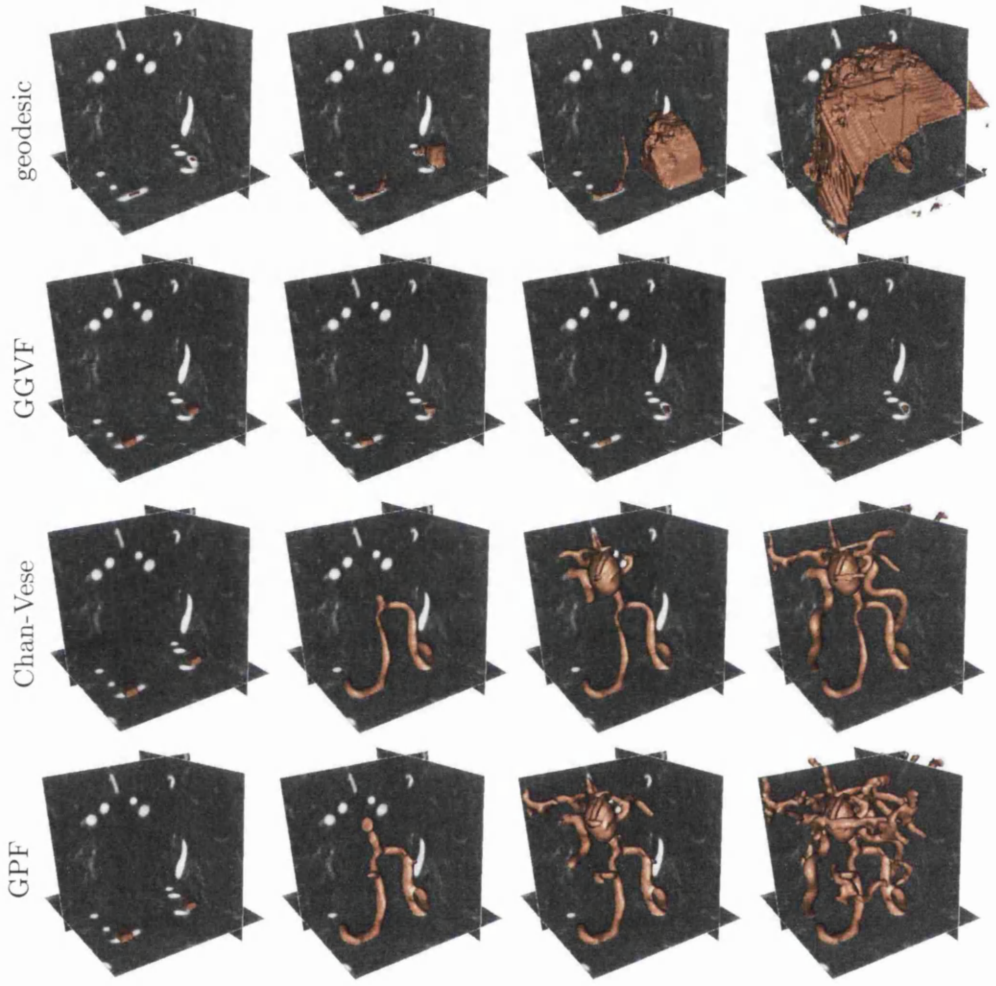

Figure 3.18: Segmentation of cerebral arterial structure from MR image dataset (128×128×128) using different deformable models - first row: geodesic (CPU-time, 5073s); second row: GGVF (CPU-time, 215s); third row: Chan-Vese (CPU-time, 6963s); fourth row: proposed GPF (CPU-time, 2614s).

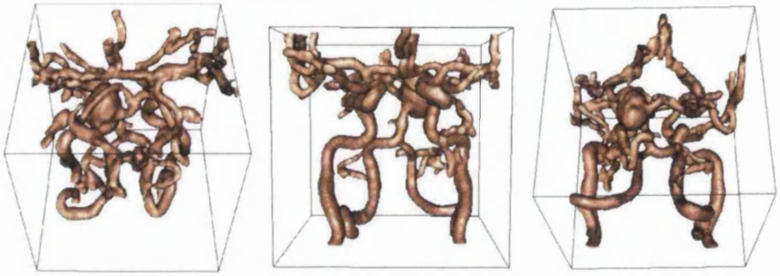

Figure 3.19: Different views of the segmented cerebral arterial model using the GPF deformable model.

uses a constant force to shrink or expand a contour, and therefore cannot be intialized across the structures. As such, multiple contours have to be initialized inside the structures for the geodesic model to handle the complex geometry and topology. As shown in the figure, the geodesic model leaks out at weak object edges due to the expansion force. The GGVF and GPF models are initialized across the object boundaries. The GGVF model cannot handle the saddle and stationary points and did not localize the image structures. In contrast, the GPF model propagates across the image structures and converge to the geometry accurately. Figure 3.16 shows the segmentation of a human aorta from CT images. In this example, a simple global image thresholding was applied to remove the dark regions which represent air cavity in the image. This preprocessing was applied so as to minimize the interference in segmenting the aorta. As the geodesic model cannot handle cross-boundary initialization, the initial surface is placed within the image structure as shown in the first row. The constant pressure term of the geodesic model easily overwhelms the weak edges and causes some leakage which expands towards the image boundary. A more arbitrary initialization is used for GGVF and GPF as shown in the second and third rows respectively. The GGVF model did not propagate through the main aortic structure and collapsed to nearby edges, while the GPF model accurately converged to the geometry of the aorta. Note that in order for the GGVF method to converge properly, the initial surface needs to be placed very close to the aorta boundaries, which is impractical in 3D. Figure 3.17 compares the segmented geometries using various deformable models with manual segmentation. It is found that although the geodesic model acquired a FG accuracy of 97.4% for this example, the corresponding BG accuracy acquired is less than 50% due to the leakage through weak edges. The GGVF model had difficulties propagating through the long narrow structure and only provided a FG accuracy of 7.3%, while the GPF model acquired a FG, BG and overall accuracy of 99.8%, 98.7% and 99.2% respectively. Figure 3.18 shows comparative results on the segmentation of cerebral arterial structure from magnetic resonance (MR) imaging. Two initial surfaces are placed inside the object of interest for the geodesic model, and across the object boundaries for GGVF, Chan-Vese and GPF. The geodesic model cannot propagate through the narrow tubular structures, and leaks out at weak object boundaries during the evolution. The GGVF model collapsed to the nearby object edges due to the saddle or stationary points inside the narrow image structures. In contrast, the Chan-Vese and GPF models are able to propagate through the long tubular structures to extract the cerebral arterial geometry. The EI model can be initialized near the boundary of the cerebral structure using the zero-crossing of the image based interaction force, and the image noise can be subsequently removed with its contour based interaction force to extract the geometry. However, this specific initialization strategy cannot be applied to segment the aorta and the femoral bone from the medical images with multiple objects shown in Figure 3.16 and Figure 3.20 respectively. Various views of the segmented cerebral arterial model using GPF is depicted in Figure 3.19. Figure 3.20 presents another example whereby a femur is segmented from CT images using the different methods. In this example, the geodesic model and the Chan-Vese model leaked due to the weak image edges and varying intensities respectively, while the GGVF and EI models had difficulties in propagating across the image object. The GPF model, however, can effectively extract the image object despite the image noise, weak edges and inhomogeneous intensities.Figure 3.21 shows the various views of the femoral model segmented using the GPF model. Figure 3.22 depicts the segmentation of multiple branches of the carotid using GPF and Figure 3.23 shows the various views of the segmented geometries. The examples above have shown that the GPF deformable model can efficiently segment narrow and complex structures, and can handle inhomogeneity in image intensities, noises and weak edges, which are often present in real images. The improvements achieved by the proposed method, as demonstrated extensively in various examples, are significant and consistent.

3.5 Summary

A novel deformable model using an external force field known as the geometric potential force (GPF) that is computed based on the relative geometrical configurations between the deformable model and image object is presented. The relative configuration between geometries gives the GPF model its distinctive bidirectionality, which allows it to handle arbitrary cross-boundary initialization. The new vector force field is dynamic and changes according to the relative position and orientation between the geometries as the deformable model evolves. As such, the dynamic force can easily attract the deformable model into highly concave regions, and propagate the surface through long thin structures. This allows the proposed method to deal with complex geometries and extreme boundary concavities efficiently. The enhancement of the potential field using nonlocal filtering can efficiently remove noise interference, and preserve object edges and fine details. Comparative studies against several existing edge based and region based techniques are provided. The results showed the proposed method achieved significant improvements in convergence capability and initialization invariance, and is more robust and efficient than the various methods. In Chapter 4, a robust

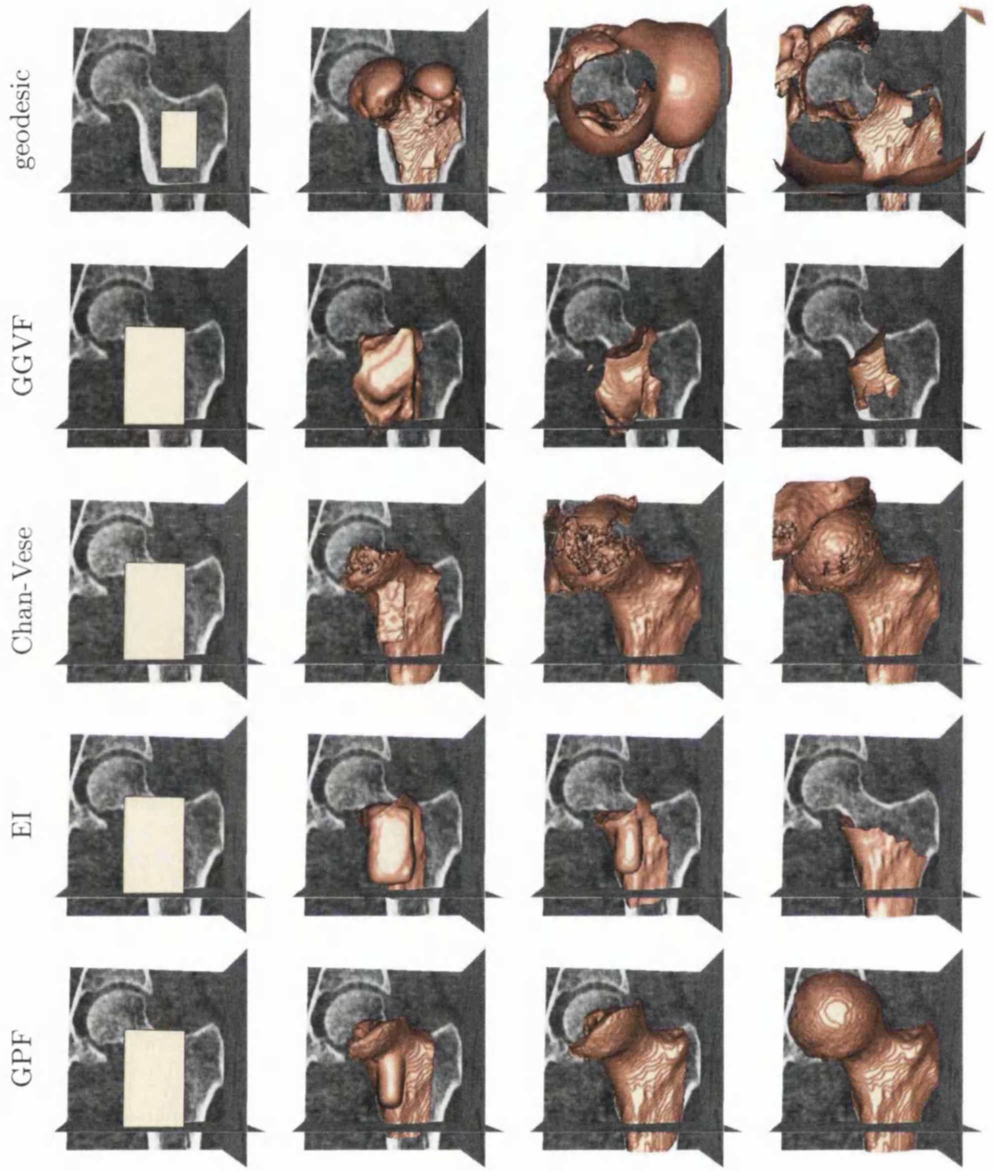

Figure 3.20: Segmentation of femur from CT image dataset (128×128×128) using different deformable models - first row: geodesic (CPU-time, 4176s); second row: GGVF (CPU-time, 1250s); third row: Chan-Vese (CPU-time, 10060s); fourth row: EI (CPU-time, 163520s); fifth row: proposed GPF (CPU-time, 2423s).

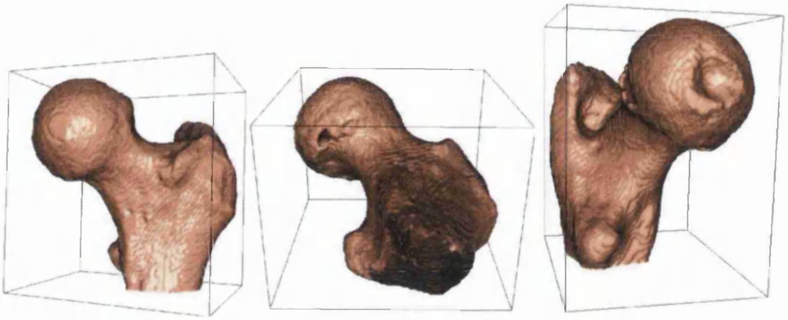

Figure 3.21: Different views of the segmented femoral model using the GPF deformable model.

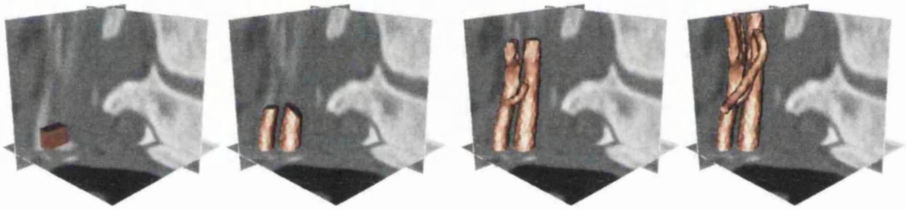

Figure 3.22: Segmentation of multiple branches of the carotid from CT image dataset (120×120×60) using GPF (CPU-time, 2581s).

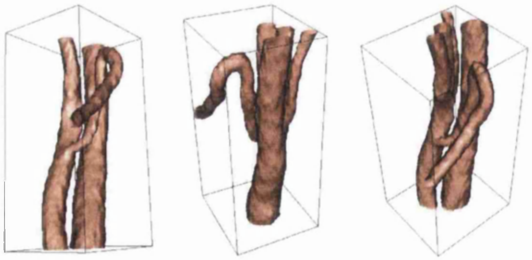

Figure 3.23: Different views of the segmented carotid model using the GPF deformable model.

segmentation framework based on the GPF deformable model with region constraint is used to extract the geometries of vessels from medical images accurately. In Chapter 5, it is shown that by incorporating shape prior information, the deformable model can efficiently handle image noise, feature inhomogeneity, occlusion and diffused object edges to segment object shapes.

Chapter 4

Segmentation of Vessel Geometries from Medical Images using GPF Deformable Model

4.1 Introduction

The human circulatory system consists of vessels that transport blood throughout the body, providing the tissues with oxygen and nutrients. It is known that vascular diseases such as stenosis and aneurysms are often associated with changes in blood flow patterns and the distribution of wall shear stress. Modelling and analysis of the hemodynamics in the human vascular system can improve our understanding of vascular disease, and provide valuable insights which can help in the development of efficient treatment methods. In recent years, computational fluid dynamics (CFD) has been widely used for patient-specific modelling of blood flow in vascular structures [139–142]. Despite the involvement of numerous groups working in this field, and rapid advancement in efficient computational methods, there has been limited applications of computational hemodynamics in clinical practice. This is largely due to the challenges involved in the design of an integrated framework which can efficiently and accurately automate the interdisciplinary computational modelling process, which includes image segmentation, mesh generation and CFD simulation.

One of the main challenges in the computational modelling of hemodynamics is the accurate reconstruction of the vascular geometry. Anatomically accurate geometric models of the vascular structures are essential for realistic flow simulations and analysis [143,144]. The anatomical information used to reconstruct the geometric models are usually provided in the form of medical image datasets (scans) from imaging modalities such as computed tomography (CT) and magnetic resonance (MR) imaging. Manual reconstruction of the vasculature geometries can be tedious and time consuming. There is also the issue of variability between the geometries extracted manually by different individuals, and variability of geometries extracted by the same individual at different occasions. In order to allow computational flow modelling to be efficiently applied as a diagnostic or predictive tool, the amount of user intervention required in the process should be reasonably small. In particular, a considerable amount of user intervention is often required in the reconstruction of an accurate geometric model for the simulation of flow dynamics. Therefore a robust and efficient method that can be used to accurately segment the geometric structures from medical image datasets can be very useful and advantageous in the modelling process. Here, we propose a robust framework for the segmentation of vessel geometries using the GPF deformable model. The framework is then applied to efficiently segment the geometries of carotid arteries from CT images.

4.2 Existing Methods for Reconstruction of Vascular Structures

Although several techniques exist for the segmentation of vascular structures from medical images, it remains an intricate process due to factors such as image noise, partial volume effects, image artifacts, intensity inhomogeneity and changes in topology. In [145], the coordinate points for the center line of the aortic arch were extracted from volume rendered MR images. A cubic spline was then used to represent the aortic centerline, and cross-sectional grids were generated on normal planes at equidistant points along the curve. This generated a curved tube with circular cross section of uniform radius, which is not representative of the geometry of the aorta. In [146], the centerline and diameter information of the vessels was extracted from the image dataset, and the vascular model was reconstructed using non-uniform rational B-splines (NURBS). Such techniques may often smooth out geometric information that can be important to the computation of accurate flow dynamics, such as those at bifurcations.

The 3D models of the vascular structures in [147] were reconstructed by extracting the 2D contours of the vessels at each of the image slices of the MR image dataset, and then lofting through the contours to create the surface models of the vessels. The different vessels were then merged using boolean operations in solid modelling. The cross sections of a particular vessel may however intersect with cross sections of branching vessels, and the geometry at these positions have to be approximated. Other authors such as [148–152] also reconstructed 3D surface models of the vessels from 2D contours extracted from image slices. This sometimes requires positioning and orienting the 2D contours according to the medial axis of the vessels, and curve and surface interpolation are used to approximate and reconstruct the surface models. However, the 2D contour extraction techniques used do not provide control over 3D smoothness, and 3D geometric properties from the image datasets are not considered.

A simple thresholding technique was used in [39] to extract the binary image of the vessels, and the vascular model was reconstructed using an isosurface algorithm. The thresholding technique however does not consider the spatial characteristics of the image, and is sensitive to image noise and inhomogeneous intensity. In [58,59], region growing algorithms were applied to segment the vascular structures from CT and MR angiography data. The region growing techniques are, in general, sensitive to noise, and can often lead to non-contiguous regions and over-segmentation. In addition, thin structures are often not extracted due to variations in image intensities. The watershed transform was used in [66] to extract the geometry of the carotid. In this approach, the image is interpreted as a landscape or topographic surface, with the pixel intensity representing the elevation of the topographic surface. Consider water on the landscape flowing towards regions with local minima, the watersheds are the lines that partition these regions. In this way, the image is partitioned into homogeneous regions with the watersheds defining the boundaries of the regions. The watershed transform tends to be sensitive to noise and often produces over-segmentation. It is also difficult for the watershed technique to extract thin structures and weak object edges.

In [153,154], a 3D dynamic surface model was used to delineate the boundary of carotid arteries. An initial triangulated model was placed within the interior of the carotid vessels, and an inflation force was applied to deform the model towards the vessel wall. In particular, the inflation force is applied only when the vertices of the model are within the lumen, i.e., at locations with image intensity below a user-specified threshold. An image-based force is further applied to the surface model to better localize the boundary. It may however be difficult to select an appropriate threshold value that delineates the vessel wall closely due to inhomogeneous image intensity. This approach is sensitive to noise, and manual editing is often required to move the vertices towards the vessel wall. In [155], a 2D discrete dynamic contour was first used to extract the vessel contours, a dynamic surface model was then inflated to reconstruct the surface model using the binary images of the extracted contours. This however does not consider the 3D geometric information from the image dataset. In [156–158], the surface models for each of the vessel branches of the carotid artery were reconstructed independently using a tubular deformable model. A surface merging algorithm is then required to reconstruct the surface model of the carotid bifurcation from the triangulated surfaces of the vessel branches. This particular approach requires the determination of the axis of each of the vessels, which can be done manually by selecting a reasonable amount of points from image slices to represent the curves of the structure. Due to the smoothing effect of this technique, regions of high curvature such as those at bifurcations or stenosis may not be modeled accurately. These explicit deformable models represent contours and surfaces parametrically, which requires the tracking of points on the curves and surfaces during deformation. It is therefore difficult for explicit deformable models to deal with topological variation and complex shapes.

Implicit deformable models have been applied in the segmentation of vascular structures in [159–163]. However, many of these techniques use an attraction force field which acts on contours or surfaces only when they are close to the object boundaries. As such, initial contours have to be placed close to the object boundaries, which can be tedious in complex geometries. A constant pressure term such as the one in [12], is often used to monotically expand or shrink the deformable model towards the image object boundaries, which can overwhelm weak object edges. In addition, the initial contours have to be placed either inside or outside object boundaries, which can be difficult for compact and narrow structures. Many of these techniques are also sensitive to image noise, and have difficulties in extracting deep boundary concavities.

4.3 Robust Framework for Reconstruction of Vascular Geometries

In this section, a robust framework is proposed for the reconstruction of vascular geometries from medical images. The approach consists of image denoising using vessel enhancing diffusion [31, 164], optimal edge detection using the Canny edge filter [32], and robust segmentation of the vascular geometries using GPF deformable model.

4.3.1 Vessel Enhancing Diffusion Filtering

The formulation of the vessel enhancing diffusion filter [31, 164] is based on a smoothed version of the vesselness measure used in [165]. In this approach, an anisotropic diffusion filter with strength and direction determined by the vesselness measure is applied to enhance the geometric structures of the vessel. The vesselness measure is determined by analyzing the eigensystem of the Hessian matrix given as:

$$\boldsymbol{H} = \begin{bmatrix} I_{xx} & I_{xy} & I_{xz} \\ I_{yx} & I_{yy} & I_{yz} \\ I_{zx} & I_{zy} & I_{zz} \end{bmatrix} \tag{4.1}$$

which describes the geometric information at each point of a 3D image intensity I based on the local intensity variations. Here, the derivatives of the image intensity I are computed as convolution with derivatives of the Gaussian function, i.e. $I_x = I(\boldsymbol{x}) * \frac{\partial}{\partial x} G_\sigma(\boldsymbol{x})$, where G_σ denotes the Gaussian function with standard deviation σ. The principal curvatures and directions are given by the maximum and minimum eigenvalues and the corresponding eigenvectors. With the eigenvalues given such that $|\lambda_1| \leq |\lambda_2| \leq |\lambda_3|$, the vesselness measure is defined as:

$$V_\sigma(\lambda) = \begin{cases} 0 & \text{if } \lambda_2 \geq 0 \text{ or } \lambda_3 \geq 0 \\ \left(1 - e^{\frac{-{R_A}^2}{2\varrho^2}}\right) \cdot e^{\frac{-{R_B}^2}{2\varsigma^2}} \cdot \left(1 - e^{\frac{-S^2}{2\vartheta^2}}\right) \cdot e^{\frac{2c^2}{|\lambda_2|{\lambda_3}^2}} & \text{otherwise} \end{cases} \tag{4.2}$$

with

$$R_A = \frac{|\lambda_2|}{|\lambda_3|} \tag{4.3}$$

$$R_B = \frac{|\lambda_1|}{\sqrt{|\lambda_2 \lambda_3|}} \tag{4.4}$$

$$S = \sqrt{{\lambda_1}^2 + {\lambda_2}^2 + {\lambda_3}^2} \tag{4.5}$$

in which R_A and R_B can be used to differentiate tubular structures from blob-like and plate-like structures, while S is used to differentiate between foreground vessel structures and background noise. The parameters ϱ, ς and ϑ are weighting factors which control the sensitivity of the vesselness measure, and c is a small constant to ensure smoothness of the function around the origin. The parameters can generally be set as $\varrho = 0.5$, $\varsigma = 0.5$, $\vartheta = 5$ and $c = 10^{-6}$ as shown in [31].

For a multiscale analysis, the vesselness function is computed for a range of scales, and the maximum response is selected using the following equation:

$$V = \max_{\sigma_{min} \leq \sigma \leq \sigma_{max}} V_\sigma(\lambda) \tag{4.6}$$

The values of σ_{min} and σ_{max} are set such that small vessels which correspond to small scales or σ values, and large vessels which correspond to large scales or σ values are enhanced, and can generally be set as $\sigma_{min} = 0.5$ and $\sigma_{max} = 2.0$.

A diffusion tensor is then defined such that vessel diffusion takes place in the direction of the vessel, while diffusion perpendicular to the vessel direction is inhibited. The diffusion tensor can therefore be used to preserve vessel structures and is given as:

$$\boldsymbol{D} = \boldsymbol{Q}\boldsymbol{\lambda}'\boldsymbol{Q}^T \tag{4.7}$$

where $\boldsymbol{Q}$ is a matrix containing the eigenvectors of the Hessian matrix $\boldsymbol{H}$, and $\boldsymbol{\lambda}'$ is a diagonal matrix with elements given as:

$$\lambda_1' = 1 + (w - 1) \cdot V^{\frac{1}{s}} \tag{4.8}$$

$$\lambda_2' = \lambda_3' = 1 + (\varepsilon - 1) \cdot V^{\frac{1}{s}} \tag{4.9}$$

with w, ε and s as tuning parameters. w should in general be a large value and determines the strength of anisotropic diffusion, ε should be a small positive constant to ensure that the tensor is positive definite, and s denotes the sensitivity to the vesselness response. The parameters can generally be set as $w = 25$, $\varepsilon = 10^{-2}$ and $s = 5.0$ as shown in [31]. The anisotropic diffusion is then defined as:

$$L_t = \nabla \cdot (\boldsymbol{D}\nabla L) \tag{4.10}$$

where $L(0)$ is set as the input image. Figures 4.1 and 4.2 show that the vessel enhancing diffusion filter can be applied to enhance the vessel structures and smooth out noise in the image. The algorithm for the vessel enhancing diffusion filter has been implemented using the Insight Toolkit [166].

4.3.2 Optimal Image Object Edge Representation for Vessel Geometries

Image object edges are usually represented as regions with high intensity contrasts. Image intensity gradients can be determined using the gradient operator or the Sobel filter which estimates image derivatives using convolution of the image with kernels designed to respond maximally to edges in the x, y and z directions. These techniques however produces object edge width of a few pixels. This can easily cause nearby structures to be connected. For complex geometries such as those in medical images, it is often necessary to determine fine edges using more robust edge detection techniques [167, 168] for accurate representation of the image structures. The Canny edge detection [32] can produce object edges with single pixel width, and can therefore be used for accurate edge detection of the vessel structures. In the Canny edge detection technique, image smoothing is first applied to reduce noise interference. This can be performed using the Gaussian filter or other smoothing techniques such as vessel enhancing diffusion [31]. Given the smoothed image intensity $I_{smooth}(\boldsymbol{x})$, the image intensity gradients are then computed to determine the magnitudes and directions of the edges. Image pixels with image intensity gradient magnitudes (i.e. $f_{edge}(\boldsymbol{x}) = |\nabla I_{smooth}(\boldsymbol{x})|$) which are not local maxima in the directions of the edges are suppressed so as to thin edge ridges. This can be done by comparing the image intensity gradient magnitude $f_{edge}(\boldsymbol{x})$ of the selected pixel with image intensity gradient magnitudes of the neighbourhood pixels. Hysterisis thresholding is then applied to filter out spurious edges caused by noise. Image pixels with edge magnitude greater than a high threshold T_h, i.e. $f_{edge}(\boldsymbol{x}) > T_h$ are considered as edges, while pixels with edge magnitude lower than a low threshold T_l, i.e. $f_{edge}(\boldsymbol{x}) < T_l$ are removed. Image pixels with edge magnitudes in between the threshold values, i.e. $T_l \leq f_{edge}(\boldsymbol{x}) < T_h$, which are connected to edge pixels are also considered as edges. The values of T_h and T_l depend on the type of images and amount of image noise. For example, a smaller T_h should be used if the image contrast is low and the edges are indistinct, and a larger T_l should be used if there is a large amount of noise in the image. In general, the values of T_h and T_l are set such that weak edges are included while image noise are suppressed. The image intensity gradients at the detected edges are then used to compute the geometric potential field as defined in Equation

(3.11). As shown in Figure 4.1 and Figure 4.2, the geometric potential field gives a more coherent representation of the image object boundaries as it utlizes global edge pixel interactions across the image.

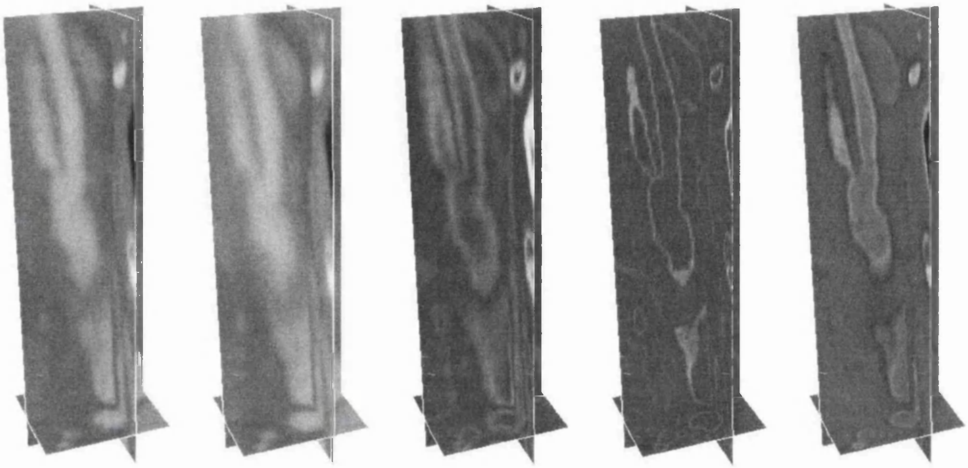

Figure 4.1: Vessel enhancing diffusion and image object edge representation of CT image dataset 1, from left to right - original image, image with vessel enhancing diffusion, image intensity gradient magnitude, Canny edge with image intensity gradient intensities, geometric potential field.

4.3.3 Segmentation of Vessel Geometries using GPF Deformable Model with Region Constraint

It was shown in Chapter 3 that the GPF deformable model can be used to efficiently segment complex geometries from biomedical images. By using pixel or voxel interactions across the whole image domain, the deformable model is more robust to image noise and weak edges. The dynamic vector force field changes according to the relative postition and orientation between the geometries, which allows the deformable model to propagate through long tubular structures.

Here, the GPF deformable model is applied to segment the geometries of

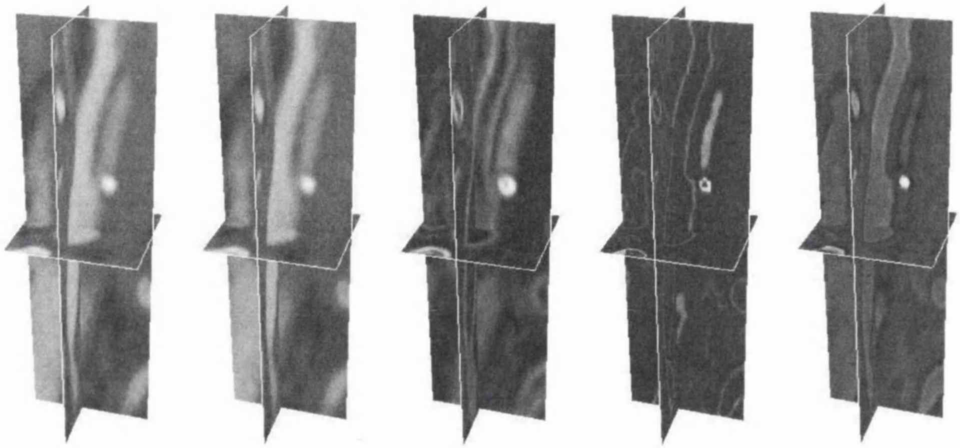

Figure 4.2: Vessel enhancing diffusion and image object edge representation of CT image dataset 2, from left to right - original image, image with vessel enhancing diffusion, image intensity gradient magnitude, Canny edge with image intensity gradient intensities, geometric potential field.

human carotid arteries from CT images. Some of the main challenges in the segmentation of the carotid geometries include intensity heterogeneity, weak edges and adjacent veins with similar intensities to the carotid. In addition, calcifications which are attached to the arterial walls should not be included in the reconstructed geometries. Although the calcified plaques often appear as relatively bright regions compared to soft tissues, plaques with lower densities may have similar intensities to the lumen. As the intensities of the plaques vary with the densities, it is not easy for techniques such as global intensity threshold to remove the plaques from the extracted geometries. In this section, a region constraint is added to the deformable model such that it does not propagate across the calcified regions. This is done by constraining the deformable model from propagating across regions with image intensity gradient magnitude larger than a user specified value, T_{max}. The deformable

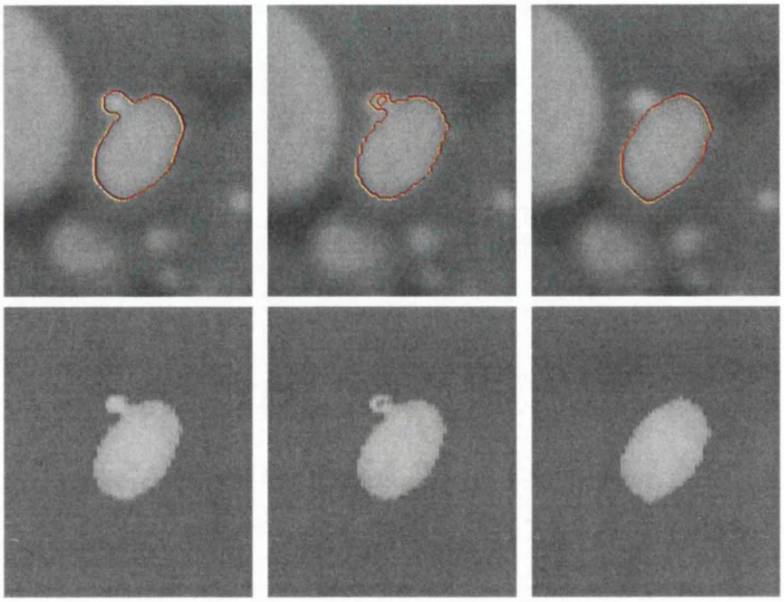

Figure 4.3: Image slice from CT image dataset 2 showing contours (top row) and corresponding pixels (bottom row) extracted using: from left to right - GPF deformable model, GPF deformable model with intensity threshold and GPF deformable model with region constraint.

model with region constraint can thus be expressed as:

$$\frac{\partial \phi}{\partial t} = \begin{cases} 0 & \text{if } |\nabla I| > T_{max} \\ \alpha\, g\, \kappa\, |\nabla \phi| - (1-\alpha)(\mathbf{F} \cdot \nabla \phi) & \text{otherwise} \end{cases} \tag{4.11}$$

where α is a weighting parameter, g is the edge stopping function, κ is the curvature and $\mathbf{F}$ is the geometric potential force defined in Equation (3.14). α is generally set to a small value, i.e. $\alpha = 10^{-4}$ to $\alpha = 10^{-3}$. As the calcified regions usually have relatively large image intensity gradients, the threshold value T_{max} can be easily selected by observing the histogram of the image intensity gradient magnitude, and is generally set to $T_{max} = 350$ to $T_{max} = 420$ in the experiments.

Figures 4.3 and 4.4 depict a z-axis slice of the extracted geometry. As

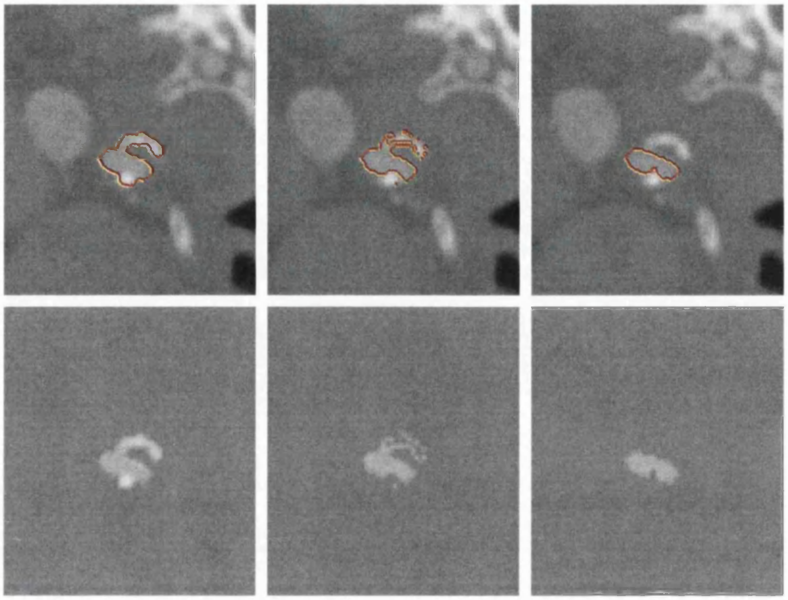

Figure 4.4: Image slice from CT image dataset 4 showing contours (top row) and corresponding pixels (bottom row) extracted using: from left to right - GPF deformable model, GPF deformable model with intensity threshold and GPF deformable model with region constraint.

shown in the figures, some calcified regions have similar intensity to the lumen, which caused the deformable model to include them in the extracted geometries. The intensities of the plaques vary which makes it difficult for a global intensity threshold to suppress them. It is shown that by adding the region constraint, the deformable model can easily get around the calcified regions to segment the carotid geometries accurately.

4.4 Results and Discussion

In this section, experimental results on the segmentation of the carotid geometries using the proposed framework are shown. In particular, 6 datasets from CT imaging (provided by Wolverhampton NHS trust) are used in the experiment. The volumes of interest containing the carotid arteries are extracted from the image datasets to reduce the size of the input datasets. The robust framework which consists of vessel diffusion enhancing, computation of optimal object edge representation and deformable model with regional constraint is then applied for the reconstruction of vessel geometries.

Figures 4.5 to 4.10 depict the segmentation of the carotid geometries using the GPF deformable model with region constraint. As shown in Figures 4.5 to 4.9, the bidirectional and dynamic vector force allows the flexible cross-boundary initializations of the model to easily propagate and converge to the geometries of the carotid arteries. The extraction of the vessel geometries from image datasets 1 and 4 took only 276s and 494s, while the extraction from image datasets 2 and 5 took 1216s and 1379s due to factors such as intensity variation, low contrast, multiple branches and complex topologies. For example, variation in intensity and low contrast can caused the image intensity gradients to take on smaller values, therefore giving a smaller vector force **F**. Also, the deformable model has to propagate a larger distance to extract geometries with multiple branches and complex topologies. A graphical user interface has been developed, which can be used to set multiple initial contours for fast convergence. It can also be used to remove inconsistency in object boundaries due to low resolution of the images, artifacts, etc., or small branches which do not affect the computational flow analysis. Figure 4.7 depicts the segmentation of the carotid artery from image dataset 3 using different initializations. As shown in Figure 4.7, one can easily speed up the segmentation process by placing multiple initial contours or surfaces, as the deformable model with a single initial surface converges to the carotid geometry in 979s, while the deformable model with multiple initial surfaces converges to the geometry in only 206s. Figure 4.10 shows the segmentation of the carotid artery from image dataset 6, in which the model converges to the vessel geometry in 185s using multiple initial surfaces. Note that the deformable model easily propagate through the stenotic carotid bifurcations

Figure 4.5: Segmentation of carotid artery from CT image dataset 1 (61×71×125) using GPF deformable model (CPU-time, 276s).

and get around the calcified regions to efficiently segment the carotid geometries from the CT images. Figure 4.11 depicts the segmented carotid geometries.

The reconstructed vessel geometries using the proposed framework are compared against geometries from manual segmentation. Figures 4.12 to 4.17 depict the comparison of the extracted geometries using random cross-section slices taken along the z-axis direction. The blue and orange contours represent the cross-section of the geometries extracted manually and using the GPF deformable model respectively. As shown in the figures, the image dataset consist of other tissue structures which may affect the geometric reconstruction. In particular, vessels adjacent to the carotid artery can often cause other models to leak out due to the similar intensity. The geometric potential field provides a more coherent and global representation of the object edges, and allows the deformable model to extract the geometry accurately. By adding a region constraint, the proposed model can easily get around the calcified regions as the deformable model propagates through the tubular structures to segment the vessel geometry as depicted in Figures 4.13, 4.14,

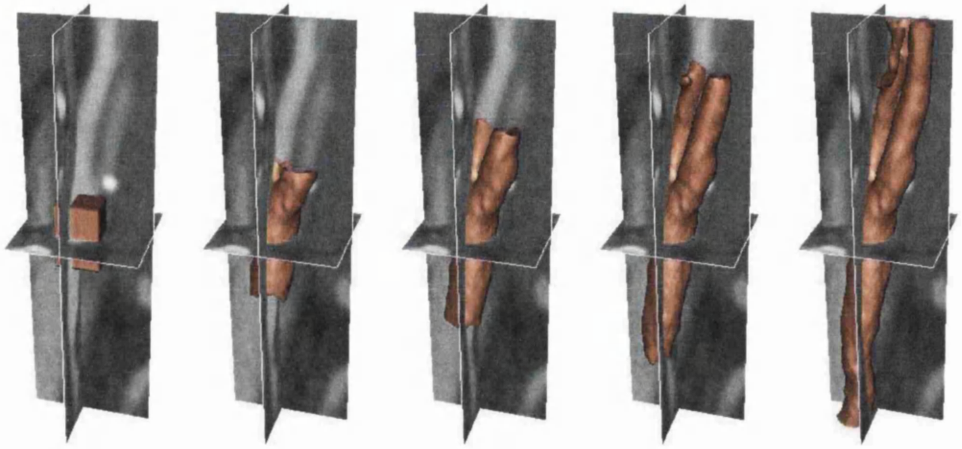

Figure 4.6: Segmentation of carotid artery from CT image dataset 2 (61×71×125) using GPF deformable model (CPU-time, 1216s).

Figure 4.7: Segmentation of carotid artery from CT image dataset 3 (70×80×120) using GPF deformable model with different initializations (top row: CPU-time, 979s, bottom row: CPU-time, 206s).

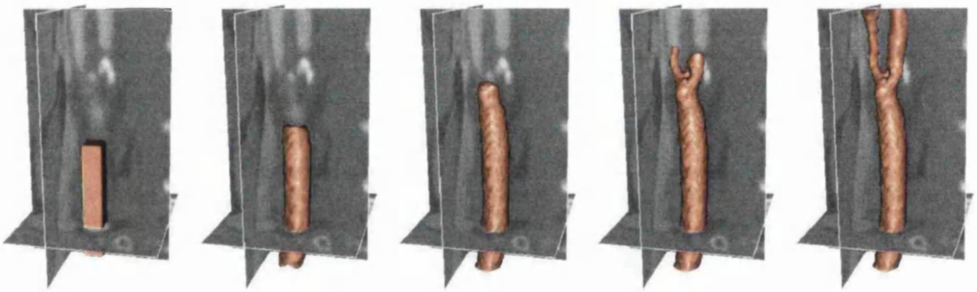

Figure 4.8: Segmentation of carotid artery from CT image dataset 4 (70×80×120) using GPF deformable model (CPU-time, 494s).

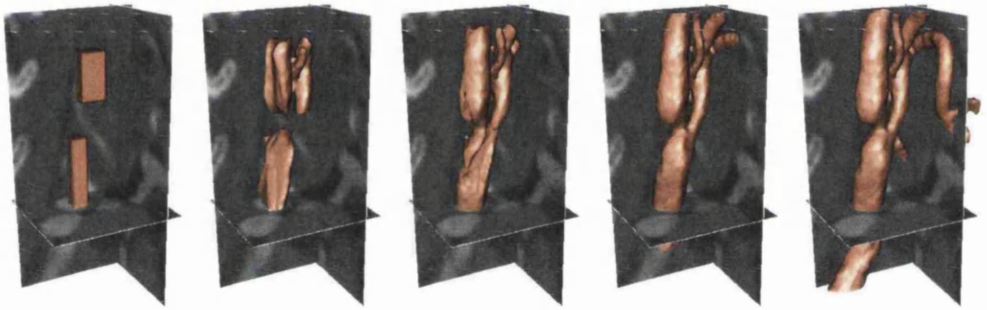

Figure 4.9: Segmentation of carotid artery from CT image dataset 5 (70×80×120) using GPF deformable model (CPU-time, 1379s).

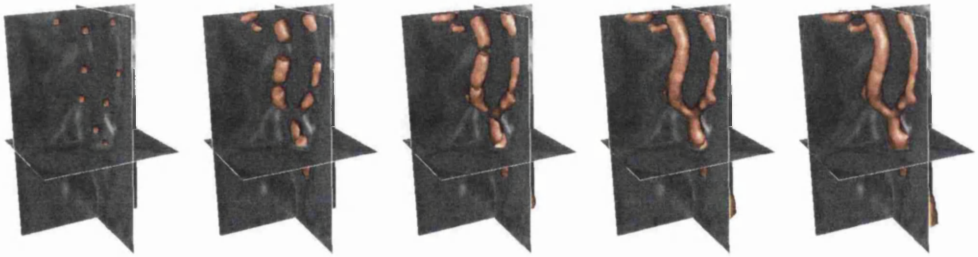

Figure 4.10: Segmentation of carotid artery from CT image dataset 6 (70×80×120) using GPF deformable model (CPU-time, 185s).

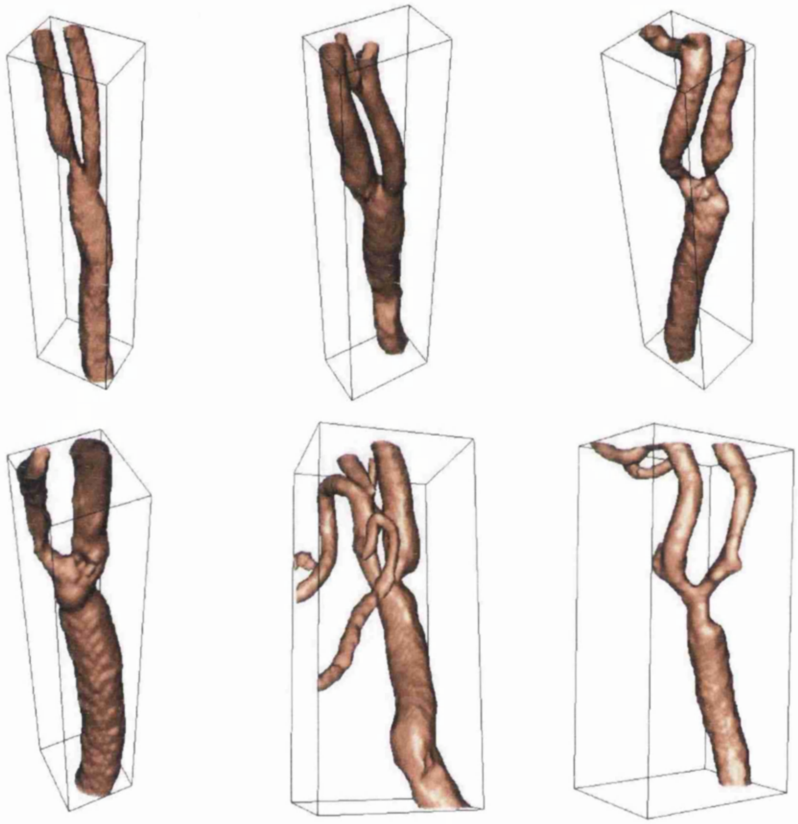

Figure 4.11: Segmented carotid geometries using the GPF deformable model.

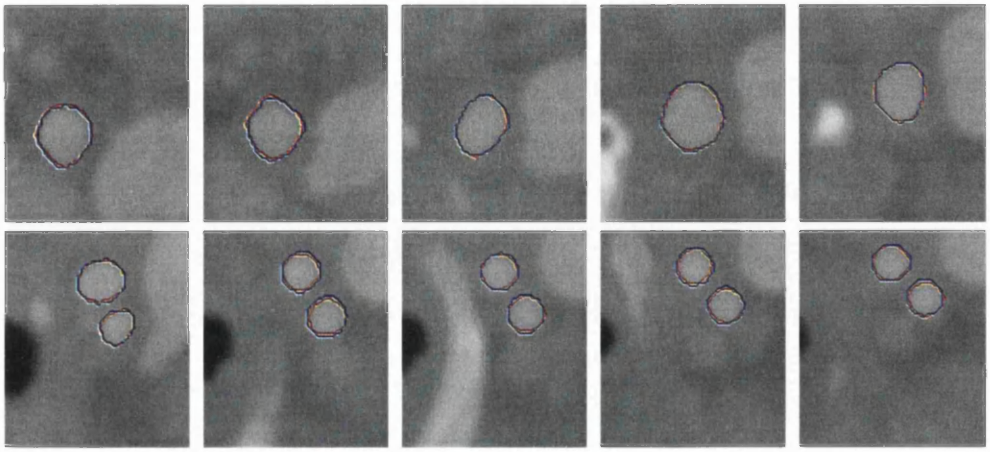

Figure 4.12: Comparison of geometry segmented from CT image dataset 1 using image slices taken along z-axis direction: blue - manual, orange - GPF deformable model.

4.15 and 4.17. The proposed framework can therefore be applied to segment the vessel geometries efficiently from the images. As shown in the figures, the vessel geometries segmented using the GPF deformable model with region constraint exhibit considerably small deviations from the manually extracted geometries.

Table 4.1 presents the accuracy of the segmented geometries using the proposed method. The foreground (FG) and background (BG) accuracy of the extracted shapes are measured as the percentages of true foreground and background voxels which were actually segmented as foreground and background respectively, i.e. $\mathrm{FG} = \frac{\mathrm{TP}}{N_{\mathrm{FG}}}$ and $\mathrm{BG} = \frac{\mathrm{TN}}{N_{\mathrm{BG}}}$, where the number of true positives (TP) and true negatives (TN) are denoted by the number of correctly classified foreground and background voxels respectively. N_{FG} and N_{BG} denote the number of true foreground and background voxels. In order for a fair measure of accuracy, a normalized overall accuracy given as the average of FG and BG (i.e. overall accuracy $= \frac{\mathrm{FG}+\mathrm{BG}}{2}$) is used to measure the accuracy of correctly extracted voxels from the image, so as to prevent measurement bias towards the large number of background voxels.

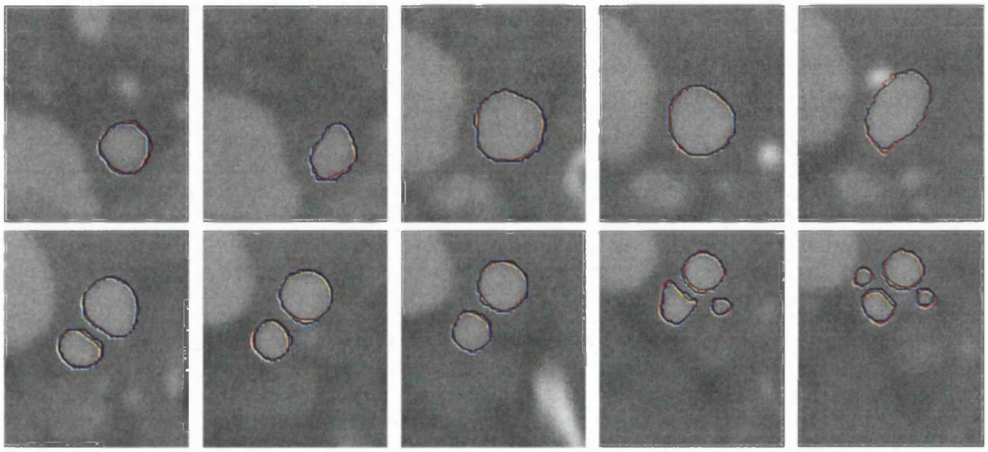

Figure 4.13: Comparison of geometry segmented from CT image dataset 2 using image slices taken along z-axis direction: blue - manual, orange - GPF deformable model.

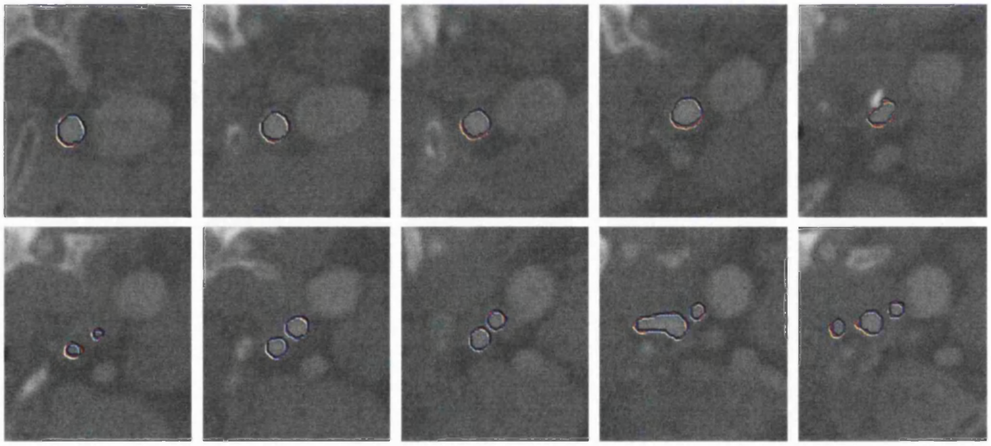

Figure 4.14: Comparison of geometry segmented from CT image dataset 3 using image slices taken along z-axis direction: blue - manual, orange - GPF deformable model.

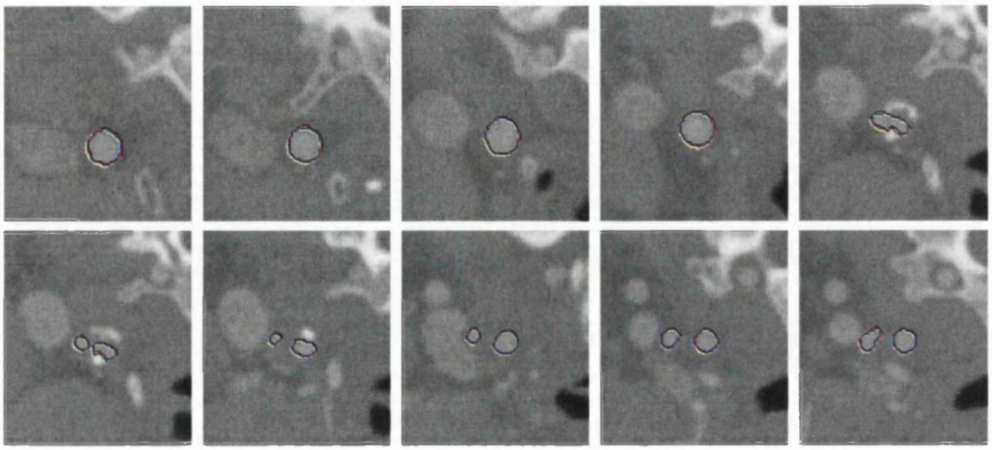

Figure 4.15: Comparison of geometry segmented from CT image dataset 4 using image slices taken along z-axis direction: blue - manual, orange - GPF deformable model.

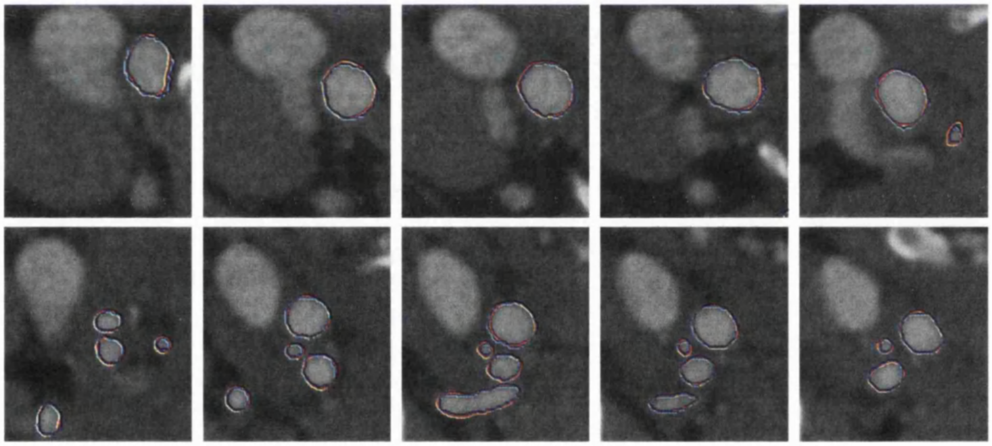

Figure 4.16: Comparison of geometry segmented from CT image dataset 5 using image slices taken along z-axis direction: blue - manual, orange - GPF deformable model.

Table 4.1: Comparison of the segmented carotid geometries using the GPF deformable model with manual segmentation: Foreground (FG), background (BG) and overall accuracy measured in %.

CT image dataset	GPF	
1	FG (%)	89.9
	BG (%)	99.9
	Overall (%)	**94.9**
2	FG (%)	89.8
	BG (%)	99.9
	Overall (%)	**94.8**
3	FG (%)	96.0
	BG (%)	99.9
	Overall (%)	**97.9**
4	FG (%)	99.1
	BG (%)	99.8
	Overall (%)	**99.5**
5	FG (%)	93.8
	BG (%)	99.5
	Overall (%)	**96.7**
6	FG (%)	94.4
	BG (%)	99.6
	Overall (%)	**97.0**
FG Average (%)		**93.9**
BG Average (%)		**99.8**
Overall Average (%)		**96.8**

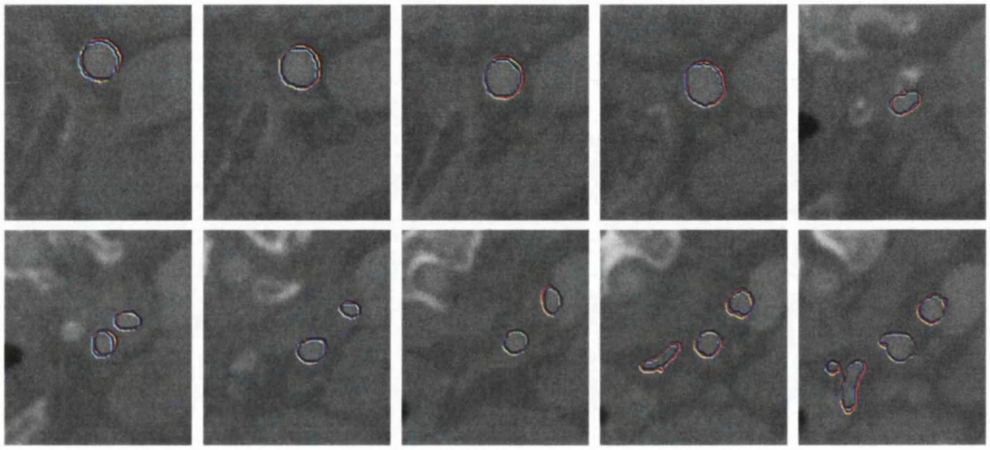

Figure 4.17: Comparison of geometry segmented from CT image dataset 6 using image slices taken along z-axis direction: blue - manual, orange - GPF deformable model.

As FG and BG do not take into account the number of misclassified voxels, and represent only the percentages of correctly classified voxels, FG and BG should be viewed together with the overall accuracy to give a good indication of the accuracy of the extracted geometries. It is shown that the proposed framework provides significantly accurate geometries with overall acurracies of 94.9%, 94.8%, 97.9%, 99.5%, 96.7% and 97.0% for image datasets 1 to 6, and an average overall accuracy of 96.8%.

4.5 Summary

We have presented a robust framework for the reconstruction of vascular geometries from medical images. Image denoising is performed using vessel enhancing diffusion, which can smooth out image noise and enhance vessel structures. The Canny edge detection technique which produces object edges with single pixel width is used for accurate detection of the lumen boundaries. The image intensity gradients are then used to compute the geometric potential field which gives a global representation of the geometric configuration. The deformable model uses a regional constraint to suppress calcified regions for accurate segmentation of the vessel geometries. The proposed framework show high accuracy when applied to the segmentation of the carotid arteries from CT images.

Chapter 5

A Variational Level Set Approach to Segmentation With Shape Prior

5.1 Introduction

Active contours provide an effective framework for object segmentation as they can easily adapt to shape variations [1,107,169]. Various types of information can also be incorporated to regularize the smoothness and shape of the contour. However, it is still a great challenge for active contour models to achieve strong invariance to initialization and robust convergence. This is particularly true when the active contour is applied on real image datasets consisting of varying intensities and complex geometries. In the presence of artifacts, occlusions or large amount of noise, it is difficult for purely image-based models to extract objects accurately. In such cases, prior knowledge of shape information can be very useful as it provides a constraint to the deformation of the contour such that the model favours similar shapes represented in the training set.

One of the earliest approach in modeling shape information uses an explicit representation of the shapes. In [170], the training shapes are represented using landmark or control points, and principal component analysis (PCA) is used to model the variability of the training set. The use of landmark points however has a drawback as the accuracy of the shape analysis depends on the quality of the landmarks. In addition, such shape models require the parameterization of the active contours. Recently, various groups [70, 171–173] have incorporated shape prior information into the level set framework. In [171], shapes are represented using signed distance functions, and PCA is applied to the training shapes. The prior information is then incorporated into a geodesic active contour [29] to attract the level set function towards similar shapes represented in the shape distribution. The shape model is then composed of the mean shape and a weighted sum of the principal modes of variation. In [174], PCA is applied to the space of signed distance functions, and the parameters of the principal eigenmodes are optimized efficiently. The signed distance functions are more robust to slight misalignments of the training shapes than parametric contours. However, the space of signed distance function is nonlinear and the shape representations using linear combination of eigenmodes do not in general correspond to a signed distance function. In [175], the shape information is imposed onto the contour extracted from the level set function at each iteration. The shape prior therefore acts on the contour and has difficulties in modelling topological changes.

In general, many of the shape models are based on statistical assumptions that the training shapes are distributed according to a Gaussian distribution. This can easily restrict the range of applications as real world objects can often exhibit complex shape variations and the projection from 3D object to 2D image can be nonlinear. In [70, 173, 176], the kernel density estimation (KDE) which is a nonparametric technique for the estimation of probability distribution functions, is applied to the space of shapes to model the shape distribution. This allows the model to handle a relatively large variation of shapes.

In this chapter, a new variational level set model using Bayesian inference is presented. The proposed model uses an image based energy and shape based energy to attract the active contour towards the object shape. Image intensity and colour or their local distributions has been commonly used to derive the image energy, such as in [173, 176]. Texture information can also be used, however they may form a large dimensional feature space, which can be difficult to formulate in the level set framework without cascading the feature vectors that may reduce its discriminability. Image intensity gradient is sensitive to image noise and weak edges as it uses local image information, and region based models are often affected by intensity variations. In this chapter, the image based energy is derived from the global interaction of image intensity gradient vectors. This gradient vector interaction field is also known as the geometric potential field, and it is shown in Chapter 3 that its vector form can increase the robustness and efficiency of the active contours in handling image noise, challenging initialization, weak edge and even broken object boundaries. Here, its scalar form is used as an image feature to indicate the presence of object boundaries. Its characteristics are fundamentally different from image intensity or image intensity gradient, as it exhibits a coherent and global geometric configuration of the image objects. The shape based energy is incorporated into the segmentation model using nonparametric shape distribution [173]. The use of the nonparametric technique of KDE allows the shape prior to model arbitrary shape distributions, and can therefore handle large shape variations in the training set. The proposed model which consists of the image and shape based energy allows the active contour to efficiently handle feature inhomogeneity, occlusion, image noise and weak object edges.

5.2 Proposed Method

In this section, the formulation of the proposed level set based segmentation model is presented. The proposed model consists of an image attraction force which propagates contours towards object boundaries, and a global shape force which deforms the model according to the shape distribution learned from a training set. The image attraction force is derived from the interaction of gradient vectors. It differs from conventional image intensity gradient based methods as it utilizes pixel interactions across the whole image domain. A shape distance is defined to measure the dissimilarity between shapes. The statistical shape information is incorporated into the model using nonparametric shape density distribution of the training shapes.

5.2.1 Bayesian Formulation of Segmentation Model

In this section, the segmentation model is formulated using Bayesian inference, where the segmentation of an image represented by the image intensity I can be considered as maximizing the conditional probability given as

$$p(\phi|I) = \frac{p(I|\phi)p(\phi)}{p(I)} \tag{5.1}$$

Here, $p(\phi|I)$ denotes the posterior probability and $p(I|\phi)$ is called the likelihood which is the probability of I given the shape ϕ. The shape that maximizes the posterior probability distribution can be estimated using a maximum a posteriori (MAP) approach:

$$\begin{aligned} \hat{\phi} &= \underset{\phi}{\operatorname{argmax}}\, p(\phi|I) = \underset{\phi}{\operatorname{argmax}}\, p(I|\phi) \cdot p(\phi) \\ &= \underset{\phi}{\operatorname{argmin}} \Big(-\log(p(I|\phi)) - \log(p(\phi)) \Big) \end{aligned} \tag{5.2}$$

since $p(I)$ is independent of the shape ϕ and is constant for a given image. The MAP estimation of the shape in Equation (5.2) that maximizes the posterior probability can also be achieved to minimize the following energy functional:

$$
\begin{aligned}
E(\phi) &= -\log(p(I|\phi)) - \log(p(\phi)) \\
&= E_{image}(\phi) + \nu E_{shape}(\phi)
\end{aligned} \tag{5.3}
$$

where $E_{image}(\phi)$ represents the image based term, $E_{shape}(\phi)$ represents the shape prior and ν is a constant that controls the influence of the shape based energy. Note that maximizing the posterior probability in Equation (5.1) is equivalent to minimizing the negative log-likelihood which is given as a sum of the energies $E_{image}(\phi)$ and $E_{shape}(\phi)$ in Equation (5.3). The minimization of the energy functional $E(\phi)$ can therefore be interpreted as a segmentation model that simultaneously maximizes the accuracy of the object boundaries located by the evolving shape, and the similarity of the evolving shape with respect to the shapes represented in the training set.

5.2.2 Image Based Energy

The image based term is used to propagate the model towards the feature of interest in the image and can be image intensity gradient based or region based. Conventional image intensity gradient based methods [12, 29] are often sensitive to image noise as they make use of local image information. The gradient vector flow (GVF) model in [103] uses vector diffusion which increases the attraction range and allows the model to handle boundary concavities. It however has convergence issues caused by saddle or stationary points in its force field [114,177]. Although region based techniques [1,47,107] exhibit more robustness against noise, they often cannot handle feature inhomogeneity. In Chapter 3, a new image attraction force based on hypothesized gradient vector interactions for contour evolution is derived. Here, the image based energy is formulated in a variational framework so that statistical prior information can be conveniently incorporated into the model.

The following image based energy functional is proposed:

$$E_{image}(\phi) = \rho \int_{\Omega} g(\boldsymbol{x})|\nabla H(\phi)|d\boldsymbol{x} + \int_{\Omega} G(\boldsymbol{x})H(\phi)d\boldsymbol{x} \tag{5.4}$$

where ρ is a constant parameter that controls the smoothness of the contour, $g(\boldsymbol{x}) = 1/|1 + \nabla I|$, and H is the Heaviside function. $G(\boldsymbol{x})$ represents the gradient vector interaction field given as:

$$G(\boldsymbol{x}) = \int_{\Omega} \frac{\hat{\boldsymbol{r}}_{\boldsymbol{x}\boldsymbol{x}'}}{r^{\lambda}_{\boldsymbol{x}\boldsymbol{x}'}} \cdot \nabla I(\boldsymbol{x})d\boldsymbol{x} \tag{5.5}$$

where $\hat{\boldsymbol{r}}_{\boldsymbol{x}\boldsymbol{x}'}$ is the unit vector from pixel location $\boldsymbol{x}$ to $\boldsymbol{x}'$ and $r_{\boldsymbol{x}\boldsymbol{x}'}$ is the distance between the pixels, and λ is a constant which coincides with the dimension of the image data (i.e. $\lambda = 2$ for 2D image). The first term in Equation (5.4) induces the segmentation model to favor minimal length, while the second term attracts the active contour towards object boundaries

Although the gradient vector interaction field $G(\boldsymbol{x})$ is derived from image intensity gradients, it utilizes image pixels or voxels across the whole image domain, and thus gives a global representation of the geometric configuration. This provides the active contour with a high invariance to initializations and a large attraction range. It also increases the robustness of the active contour against image noise.

5.2.3 Shape Based Energy

In this section, a nonparametric technique is used to generate a statistical shape distance measure for level set based shape representations. The signed distance function which can be conveniently derived from the level set function is used to represent a shape. Figure 5.1 depicts the various representations of shapes. As shown in the figure, the signed distance function exhibits spatial correlation between the pixels and the object boundaries, and can thus be effectively used for shape representations.

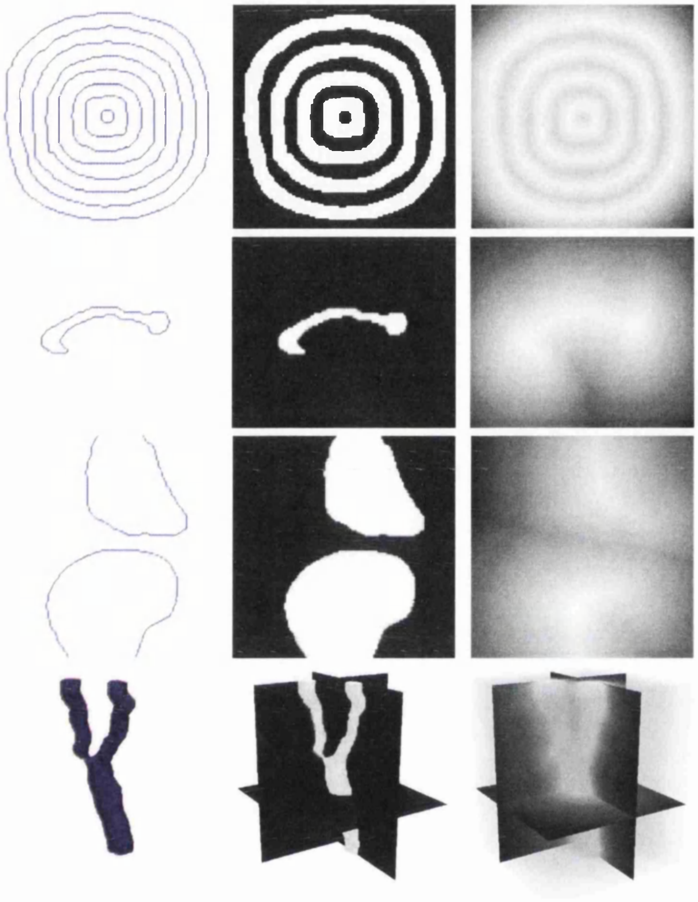

Figure 5.1: Various shape representations: (from left to right, top to bottom) contour or surface, binary image and signed distance function representations of shapes for annular-like objects, corpus callosum, knee and carotid respectively.

In order to derive a shape prior, a distance or dissimilarity measure for two shapes has to be defined. Given a set of training shapes $\{\phi_i\}_{i=1...N}$, the shape distance measure between the evolving shape and the training shapes

ϕ_i can be defined as:

$$D^2(\phi, \phi_i) = \int\limits_{\Omega} \Big(H(\phi(\boldsymbol{x} + \mu_\phi)) - H(\phi_i) \Big)^2 d\boldsymbol{x} \tag{5.6}$$

where μ_ϕ is the center of gravity of the shape ϕ, and can be defined as $\mu_\phi = \int \boldsymbol{x} h(\phi) d\boldsymbol{x}$, where $h(\phi) = \frac{H(\phi)}{\int_\Omega H(\phi) d\boldsymbol{x}}$. Note that the training shapes ϕ_i are assumed to be aligned with respect to their center of gravity. The intrinsic alignment in the shape distance provides a dissimilarity measure which is invariant to the location of the shape ϕ.

The nonparametric technique of KDE can then be used to model the statistical shape distribution. Here, the shape energy functional is defined based on a probability density on the space of signed distance functions by integrating the shape distance (5.6) in KDE as

$$E_{shape}(\phi) = \frac{1}{N} \sum_{i=1}^{N} exp \left(-\frac{1}{2\sigma^2} D^2(\phi, \phi_i) \right) \tag{5.7}$$

where σ is the kernel width, and can be set based on the mean nearest-neighbor distance. The shape prior is invariant to the translation of the shape ϕ. Intrinsic alignments with respect to scale and rotation can also be incorporated in the model [173].

5.2.4 Variational Level Set Segmentation Model With Global Shape Prior

The minimization of the energy functional in Equation (5.3) generates a segmentation model which attracts the active contour towards image object boundaries and similar shapes in the training set. The gradient descent with respect to the shape ϕ is used to minimize the energy functional in Equation (5.3), and can be derived using calculus of variation as:

$$\frac{\partial \phi}{\partial t} = -\frac{\partial E_{image}(\phi)}{\partial \phi} - \nu \frac{\partial E_{shape}(\phi)}{\partial \phi} \tag{5.8}$$

The image based gradient flow is given as:

$$\frac{\partial E_{image}(\phi)}{\partial \phi} = \rho\, g(\boldsymbol{x}) \nabla \cdot \Big(\frac{\nabla \phi(\boldsymbol{x})}{|\phi(\boldsymbol{x})|}\Big) \delta(\phi(\boldsymbol{x})) - G(\boldsymbol{x}) \delta(\phi(\boldsymbol{x})) \tag{5.9}$$

where δ is the Dirac delta function. The shape gradient flow is defined as:

$$\frac{\partial E_{shape}(\phi)}{\partial \phi} = \frac{\sum_i w_i \frac{\partial D^2(\phi, \phi_i)}{\partial \phi}}{2\sigma^2 \sum_i w_i} \tag{5.10}$$

which induces a shape force in the direction of each training shape ϕ_i weighted by the factor:

$$w_i = exp\Big(-\frac{1}{2\sigma^2} D^2(\phi, \phi_i)\Big) \tag{5.11}$$

The shape derivative with respect to ϕ is given as:

$$\begin{aligned} \frac{\partial D^2(\phi, \phi_i)}{\partial \phi} &= 2\delta(\phi(\boldsymbol{x}))\Big((H(\phi(\boldsymbol{x})) - H(\phi_i(\boldsymbol{x} - \mu_\phi)) + \frac{(\boldsymbol{x} - \mu_\phi)^T}{\int\limits_\Omega H(\phi) d\boldsymbol{x}} \\ &\times \int (H(\phi(\boldsymbol{x}')) - H(\phi_i(\boldsymbol{x}' - \mu_\phi) \delta(\phi(\boldsymbol{x}')) \nabla \phi(\boldsymbol{x}') d\boldsymbol{x}'\Big) \end{aligned} \tag{5.12}$$

The variational segmentation model therefore maximizes the alignment between the active contour and the image object boundaries, and the similarity of the evolving shape with respect to the shapes represented using the statistical shape distribution.

5.3 Implementation Details

The image object boundary representation used in the derivation of $G(\boldsymbol{x})$ can be computed using central differences, or standard edge detection methods such as the Sobel filter. Some effects caused by spurious edges can be removed by not considering pixels with very small edge magnitude, i.e. 5% - 10% of the maximum magnitude. $G(\boldsymbol{x})$ is computed efficiently as a vector convolution using FFT.

The Heaviside function H in Equation (5.4) is approximated by the regularized function H_ϵ defined as:

$$H_\epsilon(x) = \frac{1}{2}\Big(1 + \frac{2}{\pi}\arctan(\frac{x}{\epsilon})\Big) \tag{5.13}$$

and the Dirac delta function δ in Equation (5.6) is approximated by the derivative of H_ϵ as:

$$\delta_\epsilon(x) = \frac{\epsilon}{\pi(\epsilon^2 + x^2)} \tag{5.14}$$

where ϵ is an arbitrary small constant, i.e. $\epsilon = 1.0$. The finite difference method is used to approximate the derivatives, and the narrow band approach [25] which considers only a narrow band of pixels around the level set interface is used to reduce the computational cost in updating the level set function.

The training set are generated or extracted manually in the form of binary images, and the signed distance functions which represent the shapes are computed using an efficient distance transform algorithm [9].

The curvature weighting parameter ρ in Equation (5.4) can be set to a small value such as $\rho = 1.0$ or set as 0, as the shape prior can effectively smooth out noise interference and regularize the shape of the contour. The weighting parameter ν in Equation (5.3) is used to balance the effects of the image and shape based energy functionals on the segmentation process. The choice of ν depends on the specific application and the complexity of the images, and it is often required to tune this parameter for efficient segmentation [70,173,178]. A ν value that is too small may cause the shape prior to have little effect on shape regularization, and a ν value that is too large may cause the global shape force to be too dominant and overwhelm local shape features. Here, the magnitude of the gradient vector interaction field $G(\boldsymbol{x})$

is used as a guide to choose an appropriate value for ν, since it is the dominant component in the image based gradient flow given in Equation (5.9). In particular, $|G|$ is usually much larger than the magnitude of the shape gradient flow, therefore ν is set to a considerably large value to balance the image and shape based energy functionals. This can be done by setting ν to a fraction of the ratio of $|G|_{max}$ to the maximum of the magnitude of the shape gradient flow at the initial configuration. It can be noted that once the appropriate ν values are chosen, they can be used to efficiently segment a wide range of images of the same modality and application.

5.4 Results and Discussion

In this section, it is shown that the proposed method can be applied to efficiently segment image objects. The proposed method was compared against the Chan-Vese region based model [1], and the Chan-Vese model with shape prior [173] in which the proposed shape based energy is incorporated to the Chan-Vese model, on both synthetic and real images. In the experiments, a range of values for the parameters of the Chan-Vese model [1] and the Chan-Vese model with shape prior [173] are used, and the best outcomes for each model are selected to ensure a fair comparison.

5.4.1 Synthetic Images

Figure 5.2 depicts the segmentation of multiple annular-like objects from an image with 40% noise and intensity variation. It is shown that the image based energy derived from the global interactions of gradient vectors is robust to image noise and allows the active contour to extract the shapes accurately with an arbitrary cross-boundary initialization. Although the Chan-Vese model can handle the image noise, it cannot deal with the inhomogeneous intensity as shown in the figure.

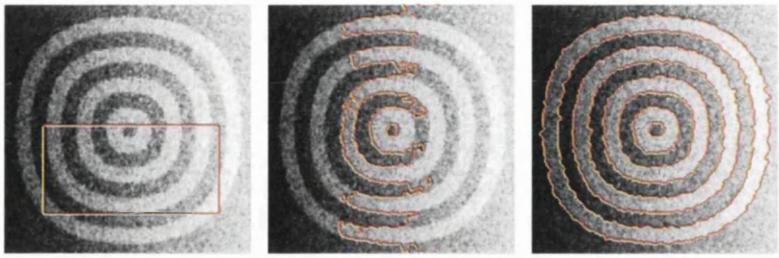

Figure 5.2: Segmentation of annular-like shapes from noisy image: (from left to right) initial contour, region based energy [1], gradient vector interaction based energy.

Next, we consider a training set of 20 images with annular-like objects of considerable shape variations which we will use to derive the shape prior. Figure 5.3 depicts 5 of the shapes of the multiple annular-like objects in the traning set. The top row of Figure 5.3 shows the binary images and the bottom row of the figure shows the signed distance function representation of the training shapes.

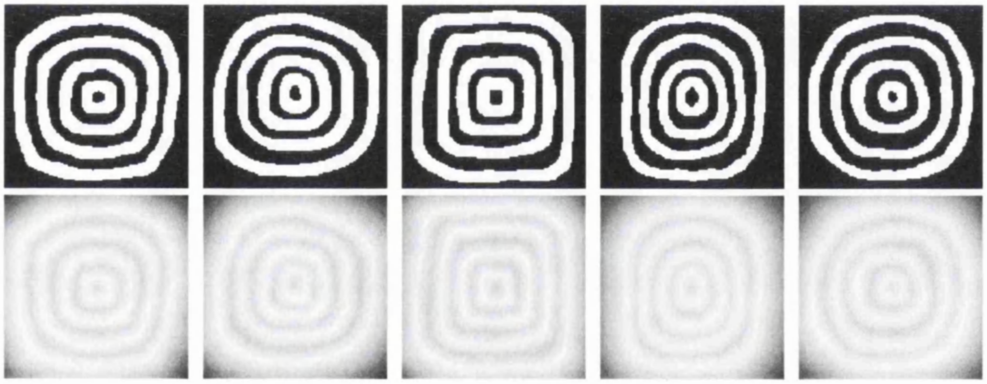

Figure 5.3: Training shapes of multiple annular-like objects: (top row) binary images and (bottom row) corresponding signed distance functions.

The shape prior is incorporated to the active contour models to extract the shapes from a noisy image (i.e. 70% of the pixels replaced by Gaussian noise), occlusions and intensity variation as shown in Figure 5.4. The top row

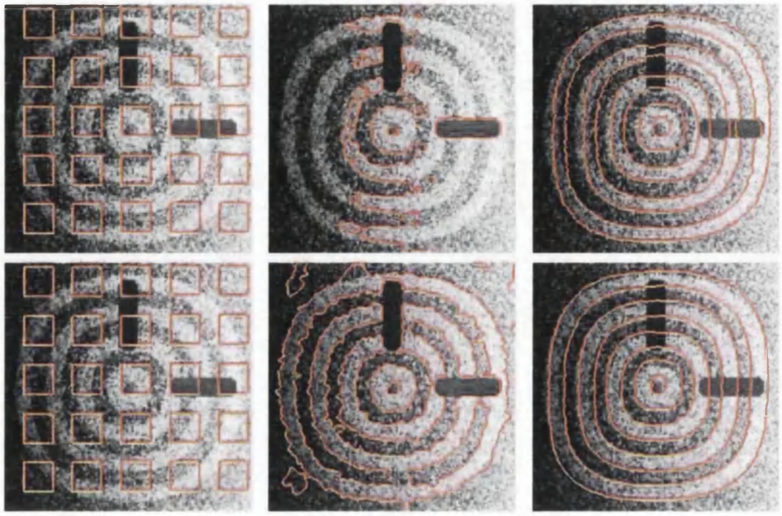

Figure 5.4: Segmentation of annular-like shapes from occluded and noisy image: (top row, from left to right) initial contour, Chan-Vese model, Chan-Vese model with shape prior, (bottom row, from left to right) initial contour, gradient vector interaction based energy, gradient vector interaction and shape based energy.

of Figure 5.4 shows the segmentation of the annular-like objects using Chan-Vese model, and Chan-Vese model with shape based energy. The bottom row of the figure shows the segmentation of the shapes using the proposed active contour with gradient vector interaction based energy, and gradient vector interaction and shape based energy. As shown in the figure, the shape force overwhelmed the region based force in the Chan-Vese model [1], and did not locate the boundaries of the objects accurately. In contrast, the proposed active contour with shape prior extracted the shapes efficiently.

Figure 5.5 shows another example in which the proposed model with shape prior is applied to segment the annular-like shapes with parts of the objects removed from the image. As shown in the figure, the gradient vector interaction based energy allows the active contour to locate the object boundaries, while the global shape based energy draws the active contour towards similar annular-like shapes to segment the image objects effectively.

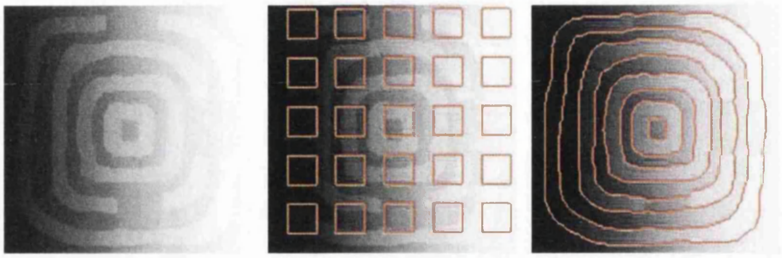

Figure 5.5: Segmentation of annular-like shapes using gradient vector interaction and shape based energy (from left to right) input image, initial contour, converged model.

5.4.2 Real Images

The proposed level set segmentation with shape prior is also applied on real images. In particular, it is shown that the statistical shape prior can be used to increase the robustness of the deformable model in the segmentation of biomedical structures such as the corpus callosum, knee joint and carotid geometries from image dataset. In the various applications, the training shapes are manually segmented to model the shape distribution. The shape priors are then used in the segmentation of the biomedical structures from images of which the shapes are not included in the training set. As the shape prior information is incorporated using nonparametric shape distribution, the model can handle a relatively large amount of shape variability in the training set. The image and shape based energies can therefore attract the contours towards image object boundaries and similar shapes represented in the shape distribution to minimize inter-operator variability.

Segmentation of the corpus callosum from MR image can be challenging as the intensity range is similar to connecting structures such as the white matter of the cortical regions and fornix as shown in Figure 5.6. Therefore, segmentation models which use only image information may often include other white matter regions due to diffused object boundaries and similar region characteristics in the image. By incorporating prior shape information, the segmentation model can attract the model to similar shapes represented in the shape distribution to efficiently segment the structure from the image.

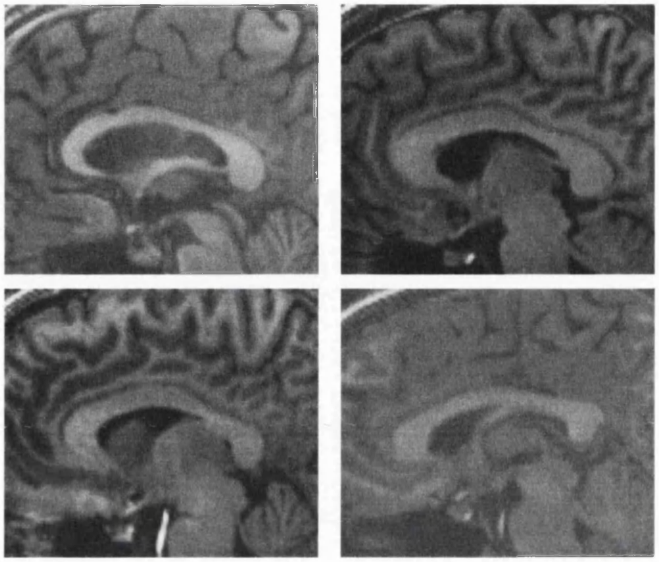

Figure 5.6: Various images of the brain: structures such as the white matter of the cortical regions and the fornix have similar intensity range and are connected to the corpus callosum.

The training set consists of 15 shapes of the corpus callosum which are manually segmented from MR images. Figure 5.7 depicts some of the training shapes of the corpus callosum. The top row of the figure depicts the manually segmented shapes, and the bottom row of the figure shows the corresponding signed distance functions of the training shapes. The shape information is then incorporated to the active contour model to segment the corpus callosum structures from images of which the shapes are not included in the training set. In particular, the active contour is used to segment the corpus callosum shapes from 20 image datasets. The extracted contours are compared with manual segmentation to show the efficiency of the proposed model.

Figure 5.8 depicts the segmentation of the corpus callosum from MR image. The top row of the figure shows the initial contour and converged

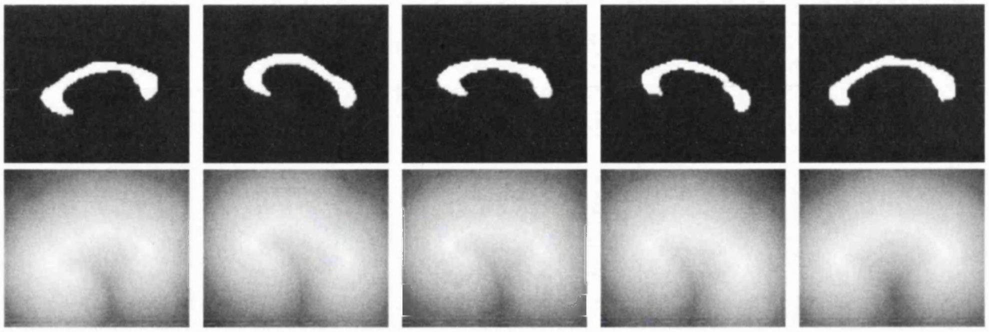

Figure 5.7: Training shapes of the corpus callosum: (top row) manually segmented images and (bottom row) corresponding signed distance functions.

contour of the Chan-Vese model, and Chan-Vese model with shape based energy. The bottom row of the figure depicts the initial contour and converged contour using the gradient vector interaction based energy, and the proposed model with shape prior. It is shown that the gradient vector interaction model is more efficient than the region based Chan-Vese model in segmenting the brain image, as the Chan-Vese model leaks out to various structures in the image. The proposed model with shape prior also provides a more accurate segmentation than the region based model with shape prior. Figure 5.9 shows another example in which the proposed method is applied to segment the corpus callosum. As shown in the figure, the active contour which uses only the image based energy, leaks out to include the fornix structure due to the similar intensity. In contrast, the proposed model with shape prior efficiently segment the shape from the image. In Figure 5.10, it is shown that the proposed active contour with shape prior is highly invariant to initializations as the active contour converged accurately to the object shape using different initializations. As shown in the figure, the active contour is initialized across different structures in the image. This makes it difficult for techniques which uses only image information to extract the geometry, as image forces generated in other structures may cause the active contour to converge to various structures with similar intensity. It is shown that the proposed active contour with shape prior can effectively overcome the image based force generated in other structures to converge to the geometry of the corpus callosum. The setting of ν is important as a ν value that is too small may cause the shape prior to have little effect on shape regularization, and a ν value that is too large may cause the shape force to be too dominant and overwhelm local shape features. Here, the magnitude of the gradient vector interaction field $G(\boldsymbol{x})$ is used as a guide to choose an appropriate ν value, since it is the dominant component in the image based gradient flow. In general, $|G|$ is much larger than the magnitude of the shape gradient flow, therefore ν is set to a relatively large value to balance the image and shape based energies. This is done by setting ν to a fraction of the ratio of $|G|_{max}$ to the maximum of the magnitude of the shape gradient flow at the initial configuration. Figure 5.11 depicts the segmentation of the corpus callosum using the proposed model with different values of the weighting parameter ν. It is shown that the active contour with different weighting parameters, $\nu = 2.0 \times 10^4$, $\nu = 3.5 \times 10^4$ and $\nu = 5.0 \times 10^4$, converged to the shape of the corpus callosum to segment the image structure accurately.

Figure 5.12 depicts the comparison of the extracted contours using the proposed model with shape prior and manual segmentation. The blue contours represent the shapes extracted manually and the orange contours represent the shapes extracted using the proposed active contour with shape prior. It is shown that the shapes segmented using the proposed model coincides closely with the manually extracted shapes. Table 5.1 presents the accuracy of the extracted contours using the proposed active contour with shape prior. It is shown that the proposed model provides accurate segmentation of the corpus callosum structures with an average foreground, background and overall accuracy of 95.7%, 99.7% and 97.7% respectively.

The proposed model is also applied in the segmentation of the knee from MR image. The training set consists of 15 shapes manually segmented from the MR image dataset. Figure 5.13 depicts some of the shapes in the training

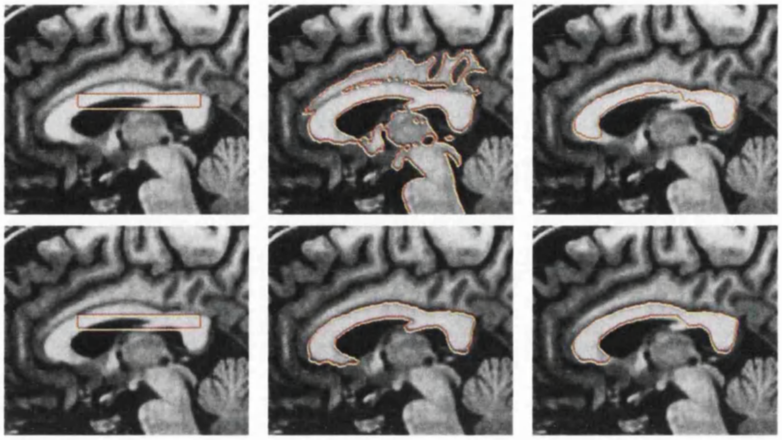

Figure 5.8: Segmentation of corpus callosum from MR image: (top row, from left to right) initial contour, Chan-Vese model, Chan-Vese model with shape prior, (bottom row, from left to right) initial contour, gradient vector interaction based energy, gradient vector interaction and shape based energy.

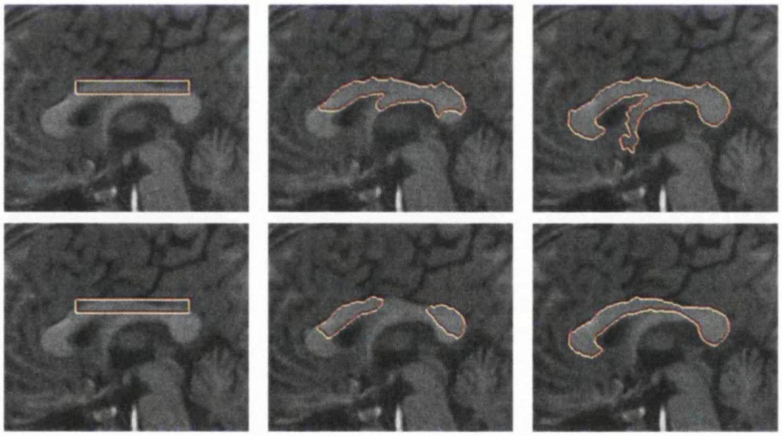

Figure 5.9: Segmentation of corpus callosum from MR image using the proposed active contour: (top row) gradient vector interaction based energy, (bottom row) gradient vector interaction and shape based energy.

Table 5.1: Comparison of the segmented corpus callosum geometries using the proposed model with manual segmentation: Foreground (FG), background (BG) and overall accuracy measured in %.

Dataset	Accuracy		Dataset	Accuracy	
1	FG (%)	97.2	11	FG (%)	99.4
	BG (%)	99.5		BG (%)	99.5
	Overall (%)	**98.3**		Overall (%)	**99.5**
2	FG (%)	92.3	12	FG (%)	96.5
	BG (%)	99.9		BG (%)	99.5
	Overall (%)	**96.1**		Overall (%)	**98.0**
3	FG (%)	98.4	13	FG (%)	98.4
	BG (%)	99.3		BG (%)	99.5
	Overall (%)	**98.9**		Overall (%)	**98.9**
4	FG (%)	97.9	14	FG (%)	93.6
	BG (%)	99.5		BG (%)	99.8
	Overall (%)	**98.7**		Overall (%)	**96.7**
5	FG (%)	94.1	15	FG (%)	95.4
	BG (%)	99.8		BG (%)	99.8
	Overall (%)	**96.9**		Overall (%)	**97.6**
6	FG (%)	96.4	16	FG (%)	93.6
	BG (%)	99.8		BG (%)	99.9
	Overall (%)	**98.1**		Overall (%)	**96.7**
7	FG (%)	89.6	17	FG (%)	97.5
	BG (%)	99.8		BG (%)	99.8
	Overall (%)	**94.7**		Overall (%)	**98.6**
8	FG (%)	96.0	18	FG (%)	90.2
	BG (%)	99.8		BG (%)	99.9
	Overall (%)	**97.9**		Overall (%)	**95.1**
9	FG (%)	95.6	19	FG (%)	97.4
	BG (%)	99.4		BG (%)	99.9
	Overall (%)	**97.5**		Overall (%)	**98.6**
10	FG (%)	98.9	20	FG (%)	96.1
	BG (%)	99.6		BG (%)	99.7
	Overall (%)	**99.3**		Overall (%)	**97.9**
FG Average (%)					**95.7**
BG Average (%)					**99.7**
Overall Average (%)					**97.7**

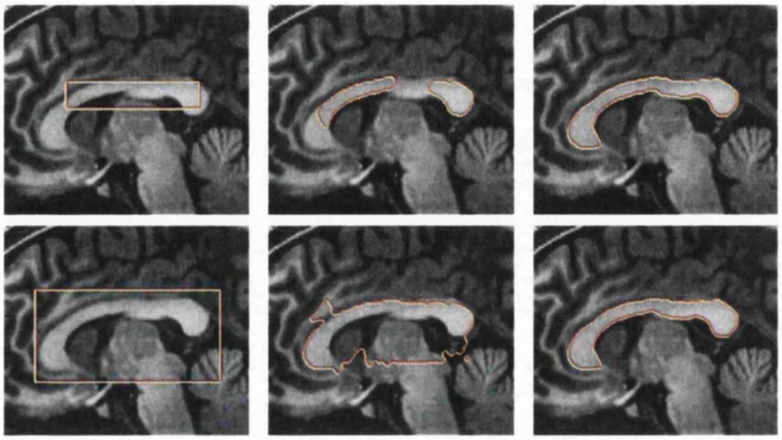

Figure 5.10: Segmentation of corpus callosum from MR image using the proposed active contour with shape prior using different initializations: (top row) initialization across boundary of object, (bottom row) initialization outside boundary of object.

set. The top row of the figure shows the shapes segmented manually from the MR images, and the bottom row of the figure shows the corresponding signed distance functions of the training shapes.

Figure 5.14 depicts the segmentation of the knee using various active contour models. The top row of the figure shows the segmentation of the knee using the Chan-Vese model and Chan-Vese model with shape prior. The bottom row of the figure shows the segmentation of the knee using the gradient vector interaction based energy, and proposed model with gradient vector interaction and shape based energy. It is shown that the gradient vector interaction based energy provides a more robust segmentation of the knee as compared to the region based energy. The incorporated shape prior information also gives a more accurate segmentation with the proposed method. Figure 5.15 shows another example in which the proposed model with shape prior is used to segment the knee from the image. As shown in the figure, the global shape based energy attracts the active contour to similar shapes in the training set while the gradient interaction based energy allows the active

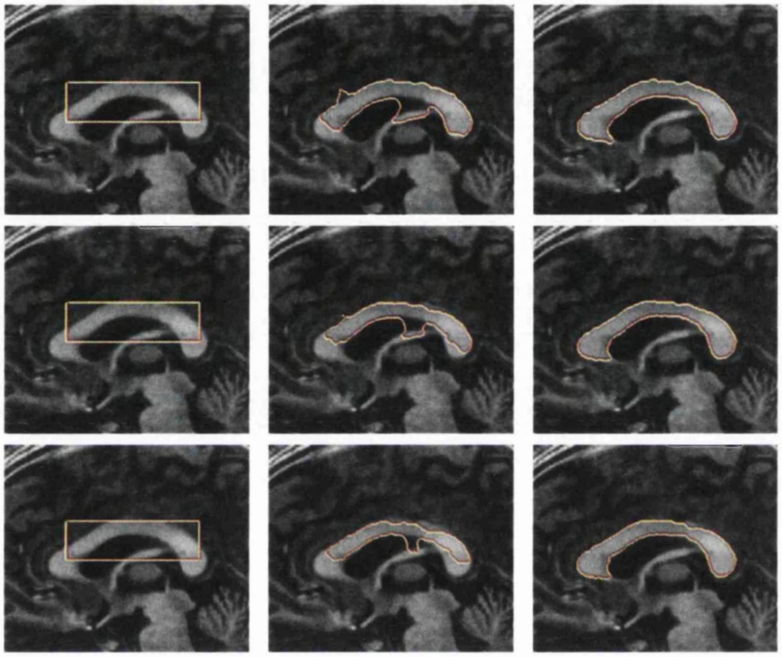

Figure 5.11: Segmentation of corpus callosum from MR image using the proposed active contour with shape prior using different parameters: (top row) $\nu = 2.0\times10^4$, (middle row) $\nu = 3.5\times10^4$ and (bottom row) $\nu = 5.0\times10^4$.

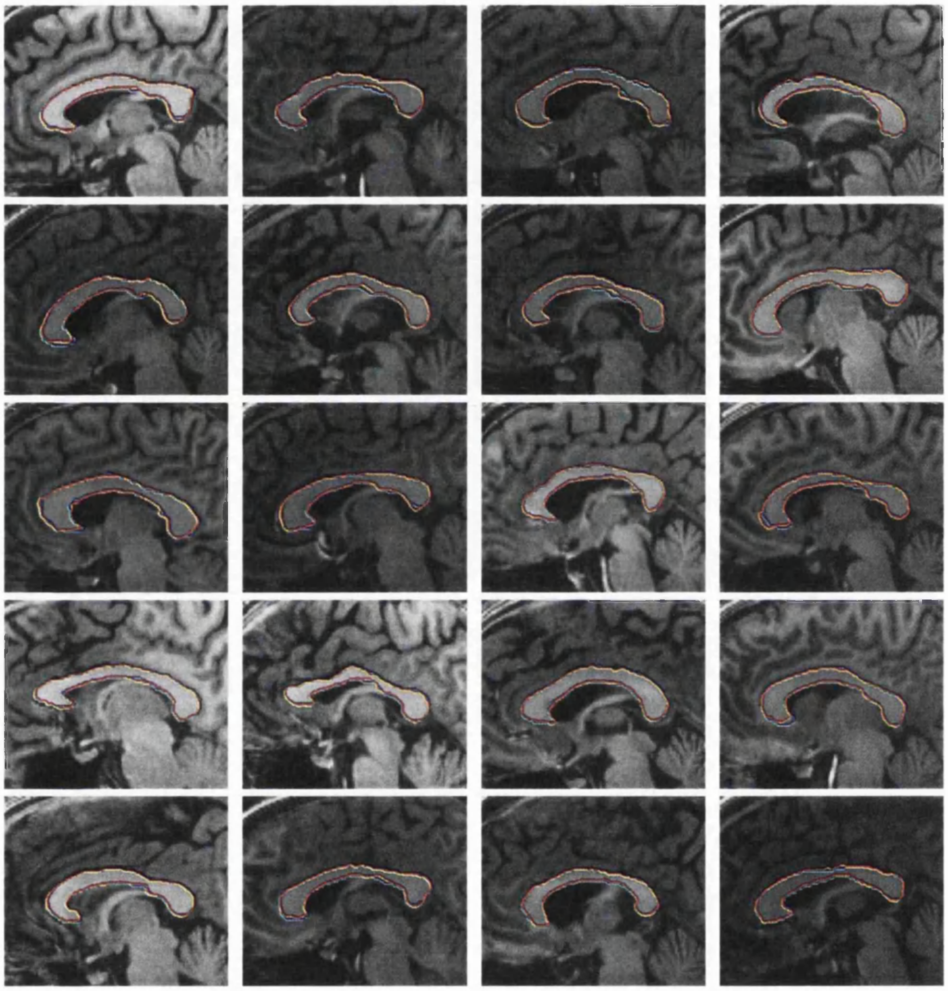

Figure 5.12: Comparison of contours extracted using the proposed active contour and manual segmentation: blue - manual, orange - proposed active contour.

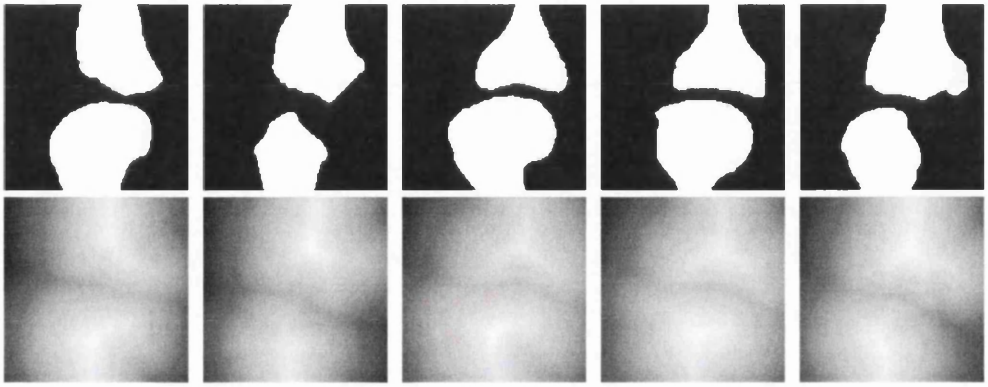

Figure 5.13: Training shapes of the knee: (top row) manually segmented images and (bottom row) corresponding signed distance functions.

contour to locate the object boundaries to segment the shapes efficiently.

Figure 5.16 depicts the segmentation of the carotid geometry from CT image using the proposed model. In this example, 20 training shapes are manually generated to model the shape distribution. Note that the image data consists of various structures such as adjacent vessels and bones, and image regions representing the carotid may often contain diffused edges and intensity inhomogeneity. Therefore, careful initializations are often required for purely image based segmentation model to extract the shape of the structure. In contrast, given an arbitrary initialization across various structures in the image as shown in Figure 5.16, the proposed deformable model with shape prior can overcome the image based forces generated by other image structures to segment the carotid geometry efficiently.

5.5 Summary

A new variational model for level set segmentation with statistical shape prior has been presented. The image based energy derived from the global interaction of gradient vectors provides a more coherent and global repre-

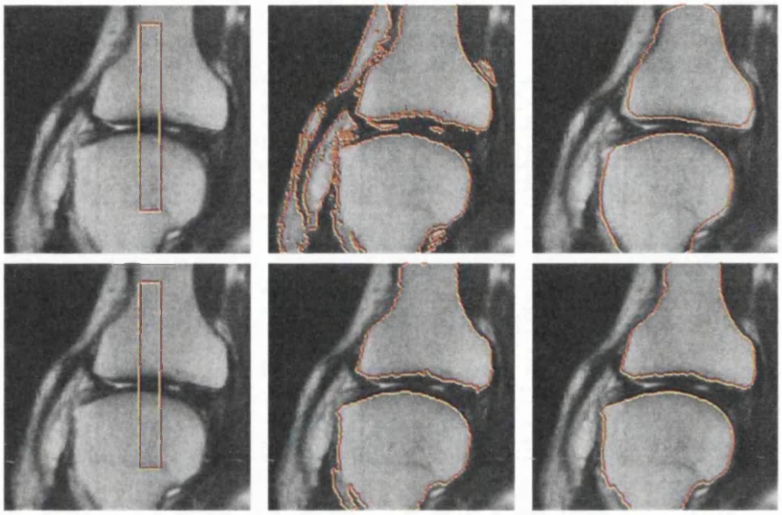

Figure 5.14: Segmentation of the knee from MR image: (top row, from left to right) initial contour, Chan-Vese model, Chan-Vese model with shape prior, (bottom row, from left to right) initial contour, gradient vector interaction based energy, gradient vector interaction and shape based energy.

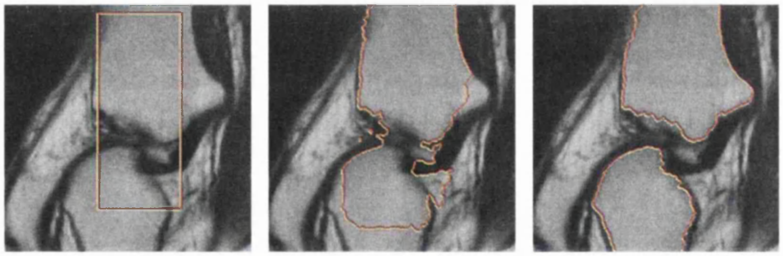

Figure 5.15: Segmentation of the knee from MR image using gradient vector interaction and shape based energy.

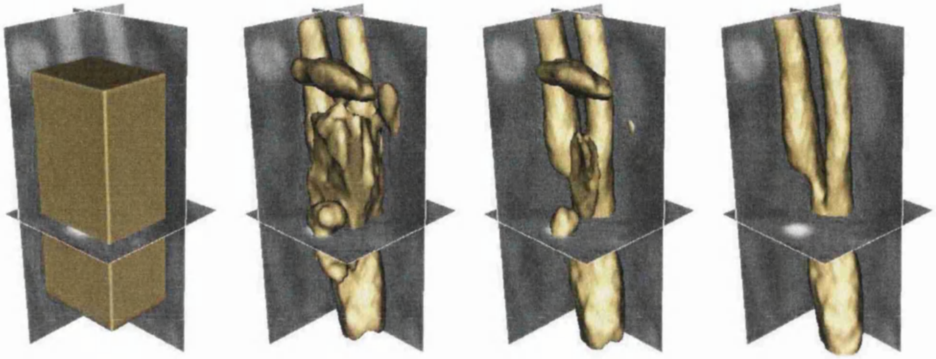

Figure 5.16: Segmentation of the carotid from CT image using gradient vector interaction and shape based energy.

sentation of the geometric configuration. The active contour model is thus more robust to image noise and weak edges, and has a strong invariance to initializations. By using kernel density estimation, the incorporated shape prior can model arbitrary shape distributions. The proposed model can thus segment complex shapes from occluded and noisy images effectively. Several examples are provided using various object shapes from synthetic and real images. It is shown that the proposed model with gradient vector interaction and shape based energy can be used to segment object shapes from various images efficiently.

Chapter 6

Conclusion and Future Work

In this thesis, new image segmentation methods based on deformable models have been presented. It is shown that the presented models can be applied to segment complex geometries from synthetic and real images accurately and efficiently. Some of the main contributions to the field of image segmentation include the derivation of a new external force field for deformable models, the design of a robust framework for the efficient segmentation of vascular geometries, and the formulation of a new deformable model with statistical shape prior.

In particular, a novel deformable model that uses an external force field known as the geometric potential force (GPF) is proposed in Chapter 3. In contrast to existing image gradient intensity based approaches, the proposed method utilizes pixel or voxel interactions across the whole image, which effectively provides a global representation of the image object. The derived geometric potential field is thus more informative and exhibits spatial and structural characteristics of image objects which are more coherent than image cues that are based solely on local edge or regional information. This makes the new model more robust towards image noise and weak object edges. The relative spatial configurations between geometries gives the proposed deformable model its distinctive bidirectionality, which facilitates the handling of arbitrary cross-boundary initializations. In addition, the new framework is equipped with a dynamic vector force field that adapts appropriately to the relative position and orientation between the geometries as the deformable model evolves. This allows the proposed deformable model to seamlessly handle complex geometries and topologies efficiently. The dynamic vector force can easily attract the deformable model into highly concave regions, and propagate the contour or surface through long thin structures. The enhancement of the geometric potential field based on regional similarity measure, can effectively remove noise interference, and yet preserve object edge information and fine details. Several comparative examples against existing edge based and region based techniques are provided using various geometries and topologies from both synthetic and real images. The comparative study clearly showed that the proposed method achieved significant improvements in convergence capability and initialization flexibility and outperformed several state-of-the-art methods. The straightforward generalization of the proposed model to higher dimensions allows the new model to be applied to N-dimensional images, and opens up to a wide range of potential applications.

A robust framework for the segmentation of vascular geometries from medical image datasets is presented in Chapter 4. The new approach consists of image denoising, optimal edge detection, and image segmentation using implicit deformable model. The image denoising is performed using vessel enhancing diffusion so as to smooth out image noise and enhance the vessel structures, and the Canny edge technique is used to detect object edges with single pixel width which is important for accurate reconstruction of complex geometries. The image gradients computed at the detected edges are then used to derive the geometric potential field which gives a global representation of the geometric configuration of the image objects. The proposed approach therefore generates a potential field which gives an accurate and coherent representation of the object boundaries of the vessels in the image.

The vessel geometries are segmented using implicit deformable model with region constraint. In particular, the region constraint is incorporated to the deformable model so as to suppress the calcified regions with considerably large image gradient magnitude. The deformable model can therefore get around the calcified regions easily for accurate segmentation of the vessel geometries. The robust framework is applied to the segmentation of carotid geometries with high accuracy.

In addition, a new deformable model with statistical shape prior using a variational approach is presented in Chapter 5. The proposed model consists of an image based energy which propagates contours towards object boundaries, and a shape based energy which attracts the model towards similar shapes represented in the shape distribution. The image based energy is derived from the interactions of gradient vectors across the whole image domain, which gives the deformable model a global representation of the geometric configuration. The deformable model is therefore more robust to image noise, diffused edges, and has a strong invariance to intializations. The shape based energy is defined using a shape distance measure with intrinsic alignment. The kernel density estimation technique is used to model the statistical shape distribution, and The incorporated shape prior can therefore model a large variation of shapes in the training set. The proposed model with shape prior can therefore be applied to segment various object shapes from synthetic and real images. The images used in the comparative analysis consist of image noise, occlusions, diffused edges and intensity inhomogeneity, and the training shapes exhibit considerable shape variation. In particular, the proposed method is applied in the segmentation of complex biomedical structures including the corpus callosum, knee joint and carotid geometries from image dataset. It is shown that the proposed model with image based energy derived from gradient vector interaction and shape based energy using statistical shape distribution, can be used to segment the various object shapes from the images efficiently.

Here, some improvements for the methods presented, and future work and directions in the area of image segmentation will be described. The geometric potential field is derived from the image gradient vector interaction across the image, which provides a global representation of geometric configuration of the image object boundaries. An attraction force field based on the global interaction of image characteristics such as regional intensity distribution can also be incorporated to the segmentation model. The deformable model will therefore be more robust as it utilizes the local edge information and regional intensity distribution, and the global interaction of the image characteristics.

The presented framework for the robust segmentation of vascular geometries uses an anisotropic diffusion filter based on the vesselness measure for image smoothing. The vesselness measure can also be incorporated in the derivation of the geometric potential field. In particular, the geometric potential field can be defined such that the magnitude takes on a larger value on object edges with higher vesselness measure. In this way, the contrast at object edges of tubular structures will be higher and image regions with other structures or image noise will be homogeneous in the derived potential field. This will allow the deformable model to accurately segment the vascular geometries.

The recent advances in medical imaging make it convenient to generate dynamic image dataset, which allows researchers to better understand the motion and function of biomedical structures. One common usage of dynamic image dataset in clinical practice is the analysis of 4D cardiac image dataset from ultrasound or MR imaging. Accurate delineation of biomedical structures from dynamic image dataset is useful for the diagnosis and computational analysis of the anatomical function. As the geometric potential force can be easily generalized to higher dimensions, the GPF deformable model can be directly applied in the dynamic segmentation of biomedical structures from 4D image dataset. Another approach for the robust segmentation of dynamic image dataset is to incorporate spatio-temporal information to the segmentation model. As biomedical structures exhibit strong temporal correlation between adjacent image frames, we can define a regularization force based on the geometric variation in the temporal direction to dynamically segment the image dataset. Image representation is important in image processing and image segmentation. A conventional way of image representation is based on image characteristics such as intensity or colours at each point of the image. However, real objects in an image are not composed of points of various intensity or colours. Different types of information such as edges, textures and shapes can be extracted from image objects at various scales. A multiscale approach can therefore be used to derive the image attraction force for the deformable models. Image edges at different spatial scales are first computed from an image smoothed using Gaussian filters of different variances. A multiscale edge representation is then derived by combining the edges detected at various scales such that image edges which exist only in fine scales are suppressed, and edges which exist at both fine and coarse scales have larger magnitudes. The multiscale edge representation can then be used to derive the image force for attracting the deformable models towards image object boundaries.

It is shown that the statistical shape information [173, 179] can be incorporated to increase the robustness of the deformable model. The prior information of the image intensity distribution can also be incorporated into the segmentation model. The intensity prior information can be used to attract the deformable model towards similar intensity distribution in the training images. The deformable model can therefore utilize the local image information and the global shape and intensity prior information to segment object shapes from images efficiently.

Appendix A

List of Parameters

GPF deformable model

$\mathcal{J}$ in Equation (3.14) – constant parameter used to control the direction of propagation of the deformable model, values set as $\mathcal{J} = \pm 1$ to give propagation in opposite directions.

α in Equation (3.16) – curvature weight parameter to control the amount of contour smoothness of the deformable model, generally set as $\alpha = 10^{-3}$.

Nonlocal smoothing of geometric potential field

$\Omega_{\boldsymbol{x}}$ in Equation (3.19) – size of search window, generally set to 21×21 for 2D images and $21 \times 21 \times 21$ for 3D images.

h and σ in Equation (3.20) – parameter to control the amount of filtering and standard deviation of Gaussian kernel respectively, generally set as $h = 1.0\sigma$ to $h = 1.5\sigma$.

$\boldsymbol{N}$ in Equation (3.20) – size of similarity neighbourhood region, generally set as $N = 7$.

Vessel enhancing diffusion

ϱ, ς and ϑ in Equation (4.2) – weighting factors to control the sensitivity of the vesselness measure, generally set as $\varrho = 0.5$, $\varsigma = 0.5$, $\vartheta = 5$.

c in Equation (4.2) – small constant to ensure smoothness of the function around the origin, set as $c = 10^{-6}$.

σ_{min} and σ_{max} in Equation (4.6) – parameters corresponding to the range of scales for vesselness measure, generally set as $\sigma_{min} = 0.5$ and $\sigma_{max} = 2.0$.

w, ε and s in Equations (4.8) and (4.9) – parameter to control strength of anisotropic diffusion, small positive constant to ensure diffusion tensor is positive definite, and parameter to sensitivity to vesselness response, generally set as $w = 25$, $\varepsilon = 10^{-2}$ and $s = 5.0$.

Optimal object edge representation

T_h and T_l – high threshold and low threshold for Canny edge detection, values of T_h and T_l depend on the type of images and the amount of noise, a smaller T_h is used if image contrast is low and a larger T_l is used if there is a large amount of noise.

GPF deformable model with region constraint

α in Equation (4.11) – curvature weight parameter to control the amount of contour smoothness, generally set as $\alpha = 10^{-4}$ to $\alpha = 10^{-3}$.

T_{max} in Equation (4.11) – threshold value for intensity gradient magnitude, value set by observing the histogram of the image gradient magnitude, generally set as $T_{max} = 350$ to $T_{max} = 420$.

Variational model with shape prior

ν in Equation (5.3) – parameter to control influence of shape based energy, value depends on the specific application and complexity of images, generally set as a fraction of the ratio of the maximum of the geometric potential field magnitude to the maximum of the shape gradient flow magnitude at initialization.

ρ in Equation (5.4) – parameter to control the smoothness of the contour, generally set as $\rho = 1.0$.

Bibliography

[1] T. Chan and L. Vese, "Active contours without edges," *IEEE Transactions on Image Processing*, vol. 10, no. 2, pp. 266–277, 2001.

[2] C. M. Smith, J. Smith, S. K. Williams, J. J. Rodriguez, and J. B. Hoying, "Automatic thresholding of three-dimensional microvascular structures from confocal microscopy images," *J. Microscopy*, vol. 225, no. 3, pp. 244–257, 2007.

[3] J. Wu, F. Ye, J. Ma, X. Sun, J. Xu, and Z. Cui, "The segmentation and visualization of human organs based on adaptive region growing method," in *Int. Conf. Comp. and Info. Tech.*, 2008, pp. 439–443.

[4] S. Ruan, C. Jaggi, J. Xue, J. Fadili, and D. Bloyet, "Brain tissue classification of magnetic resonance images using partial volume modeling," *IEEE Transactions on Medical Imaging*, vol. 19, no. 12, pp. 1179–1187, 2000.

[5] J. Hao and M. Li, "A supervised bayesian method for cerebrovascular segmentation," *WSEAS Trans. Signal Processing*, vol. 3, no. 12, pp. 487–495, 2007.

[6] J. B. Maintz and M. A. Viergever, "A survey of medical image registration," *Medical Image Analysis*, vol. 2, no. 1, pp. 1–36, 1998.

[7] Y. Boykov and G. Funka-Lea, "Graph cuts and efficient n-d image segmentation," *International Journal of Computer Vision*, vol. 70, no. 2, pp. 109–131, 2006.

[8] J. Shi and J. Malik, "Normalized cuts and image segmentation," *IEEE Transations on Pattern Analysis and Machine Intelligence*, vol. 22, no. 8, pp. 888–905, 2000.

[9] P. F. Felzenszwalb and D. P. Huttenlocher, "Efficient graph-based image segmentation," *International Journal of Computer Vision*, vol. 59, no. 2, pp. 167–181, 2004.

[10] Y. Boykov and M.-P. Jolly, "Interactive graph cuts for optimal boundary & region segmentation of objects in n-d images," in *IEEE Internaitonal Conference on Computer Vision*, 2001, pp. 105–112.

[11] V. Caselles, F. Catte, T. Coll, and F. Dibos, "A geometric model for active contours," *Numerische Mathematik*, vol. 66, pp. 1–31, 1993.

[12] R. Malladi, J. A. Sethian, and B. C. Vemuri, "Shape modelling with front propagation: A level set approach," *IEEE Transations on Pattern Analysis and Machine Intelligence*, vol. 17, no. 2, pp. 158–175, 1995.

[13] C. Xu and J. L. Prince, "Generalized gradient vector flow external forces for active contours," *Signal Processing*, vol. 71, no. 2, pp. 131–139, 1998.

[14] R. Whitaker, "Modeling deformable surfaces with level sets," *IEEE Computer Graphics and App.*, vol. 24, no. 5, pp. 6–9, 2004.

[15] N. Paragois and R. Deriche, "Geodesic active contours and level sets for the detection and tracking of moving objects," *IEEE Transations on Pattern Analysis and Machine Intelligence*, vol. 22, no. 3, pp. 226–280, 2000.

[16] N. Ray and S. Acton, "Motion gradient vector flow: An external force for tracking rolling leukocytes with shape and size constrained active contours," *IEEE Transactions on Medical Imaging*, vol. 23, no. 12, pp. 1466–1478, 2004.

[17] M. Niethammer and A. Tannenbaum, "Dynamic geodesic snakes for visual tracking," in *IEEE Conference on Computer Vision Pattern Recognition*, 2004, pp. 660–667.

[18] Y. Rathi, N. Vaswani, A. Tannenbaum, and A. Yezzi, "Particle filtering for geometric active contours with application to tracking moving and deforminb objects," in *IEEE Conference on Computer Vision Pattern Recognition*, 2005, pp. 2–9.

[19] M. Kass, A. Witkin, and T. Terzopoulos, "Snakes: Active contour models," *International Journal of Computer Vision*, vol. 1, no. 4, pp. 321–331, 1987.

[20] T. McInerney and D. Terzopoulos, "Topology adaptive deformable surfaces for medical image volume segmentation," *IEEE Transactions on Medical Imaging*, vol. 18, no. 10, pp. 840–850, 1999.

[21] H. Delingette and J. Montagnat, "Shape and topology constraints on parametric active contours," *Computer Vision and Image Understanding*, vol. 83, no. 2, pp. 140–171, 2001.

[22] J. Bredno, T. M. Lehmann, and K. Spitzer, "A general discrete model in two, three, and four dimensions for topology-adaptive multichannel segmentation," *IEEE Transations on Pattern Analysis and Machine Intelligence*, vol. 25, no. 5, pp. 550–563, 2003.

[23] J.-O. Lachaud and B. Taton, "Deformable model with a complexity independent from image resolution," *Computer Vision and Image Understanding*, vol. 99, no. 3, pp. 453–475, 2005.

[24] S. Osher and J. Sethian, "Fronts propagating with curvature-dependent speed: Algorithms based on the hamilton-jacobi formulation," *Journal of Computational Physics*, vol. 79, pp. 12–49, 1988.

[25] J. A. Sethian, *Level Set Methods and Fast Marching Methods: Evolving Interfaces in Computational Geometry, Fluid Mechanics, Computer Vision, and Material Science.* Cambridge University Press, 1999.

[26] C. Baillard and C. Barillot, "Robust 3D segmentation of anatomical structures with level sets," in *International Conference on Medical Image Computing and Computer-Assisted Intervention*, 2000, pp. 236–245.

[27] M. Law and A. Chung, "A deformable surface model for vascular segmentation," in *International Conference on Medical Image Computing and Computer-Assisted Intervention*, 2009, pp. 59–67.

[28] M. Holtzman-Gazit, R. Kimmel, N. Peled, and D. Goldsher, "Segmentation of thin structures in volumetric medical images," *IEEE Transactions on Image Processing*, vol. 15, no. 2, pp. 354–363, 2006.

[29] V. Caselles, R. Kimmel, and G. Sapiro, "Geodesic active contour," *International Journal of Computer Vision*, vol. 22, no. 1, pp. 61–79, 1997.

[30] Y. Xiang, A. Chung, and J. Ye, "An active contour model for image segmentation based on elastic interaction," *Journal of Computational Physics*, vol. 219, no. 1, pp. 455–476, 2006.

[31] R. Manniesing, M. A. Viergever, and W. J. Niessen, "Vessel enhancing diffusion: A scale space representation of vessel structures," *Medical Image Analysis*, vol. 10, no. 6, pp. 815–825, 2006.

[32] J. Canny, "A computational approach to edge detection," *IEEE Transations on Pattern Analysis and Machine Intelligence*, vol. 8, no. 6, pp. 679–698, 1986.

[33] N. Otsu, "A threshold selection method from gray-level histograms," *IEEE Transactions on Systems, Man, and Cybernetics*, vol. 9, no. 1, pp. 62–66, 1979.

[34] A. Rosenfeld and P. De la Torre, "Histogram concavity analysis as an aid in threshold selection," *IEEE Transactions on Systems, Man, and Cybernetics*, vol. 13, no. 3, pp. 231–235, 1983.

[35] M. I. Sezan, "A peak detection algorithm and its application to histogram-based image data reduction," *Computer Vision, Graphics, and Image Processing*, vol. 49, no. 1, pp. 36–51, 1990.

[36] M. J. Carlotto, "Histogram analysis using a scale-space approach," *IEEE Transations on Pattern Analysis and Machine Intelligence*, vol. 9, no. 1, pp. 121–129, 1987.

[37] Y. Zhang, Z. He, S. Fan, K. He, and C. Li, "Automatic thresholding of mirco-ct trabecular bone images," in *Int. Conf. Biomed. Eng. and Info.*, 2008, pp. 23–27.

[38] B. R. Gomberg, P. K. Saha, H. K. Song, S. N. Hwang, and F. W. Wehrli, "Topological analysis of trabecular bone MR images," *Journal of Electronic Imaging*, vol. 19, no. 3, pp. 166–174, 2000.

[39] J. R. Nanduri, F. A. Pino-Romainville, and I. Celik, "CFD mesh generation for biological flows: Geometry reconstruction using diagnostic images," *Computers & Fluids*, vol. 38, no. 5, pp. 1026–1032, 2009.

[40] C. Croce, R. Fodil, M. Durand, G. Sbirlea-Apiou, G. Caillibotte, J.-F. Papon, J.-R. Blondeau, A. Coste, D. Isabey, and B. Louis, "In

vitro experiments and numerical simulations of airflow in realistic nasal airway geometry," *Annals of Biomedical Engineering*, vol. 34, no. 6, pp. 997–1007, 2006.

[41] A. Y. T. Leung, W. S. Tsui, J. N. Xu, and J. Lo, "Nasal airflow simulations in models derived from cone beam and spiral CT scans by using CFD," *J. Applied Mathematics and Mechanics*, vol. 3, pp. 49–6, 2007.

[42] W. Niblack, *An Introduction to Image Processing.* Englewood Cliffs, N.J.: Prentice Hall, 1986.

[43] O. D. Trier and A. K. Jain, "Goal-directed evaluation of binarization methods," *IEEE Transations on Pattern Analysis and Machine Intelligence*, vol. 17, no. 12, pp. 1191–1201, 1995.

[44] N. B. Venkateswarluh and R. D. Boyle, "New segmentation techniques for document image analysis," *Image and Vision Computing*, vol. 13, no. 7, pp. 573–583, 1995.

[45] J. Bernsen, "Dynamic thresholding of gray level images," in *International Conference on Pattern Recognition*, 1986, pp. 1251–1255.

[46] A. J. Burghardt, G. J. Kazakia, and S. Majumdar, "A local adaptive threshold strategy for high resolution peripheral quantitative computed tomography of trabecular bone," *Annals of Biomedical Engineering*, vol. 19, no. 3, pp. 1678–1686, 2007.

[47] J. Kim, J. W. Fisher, A. Yezzi, M. Cetin, and A. S. Willsky, "A nonparametric statistical method for image segmentation using information theory and curve evolution," *IEEE Transactions on Medical Imaging*, vol. 14, no. 10, pp. 1486–1502, 2005.

[48] M. E. Brummer, R. M. Mersereau, R. L. Eisner, and R. R. J. Lewine, "Automatic detection of brain contours in MRI data sets," *IEEE Transactions on Medical Imaging*, vol. 12, no. 2, pp. 153–166, 1993.

[49] B. Li and S. Acton, "Active contour external force using vector field convolution for image segmentation," *IEEE Transactions on Image Processing*, vol. 16, no. 8, pp. 2096–2106, 2007.

[50] A. J. Burghardt, G. J. Kazakia, and S. Majumdar, "Image analysis using mathematical morphology," *IEEE Transactions on Pattern Analysis and Machine Intelligence*, vol. 9, no. 4, pp. 532–550, 1987.

[51] P. K. Sahoo, S. Soltani, A. K. C. Wong, and Y. C. Chen, "A survey of thresholding techniques," *Computer Vision, Graphics, and Image Processing*, vol. 41, no. 2, pp. 233–260, 1988.

[52] M. Sezgin and B. Sankur, "Survey over image thresholding techniques and quantitative performance evaluation," *Journal of Electronic Imaging*, vol. 13, no. 1, pp. 146–168, 2004.

[53] P. Gibbs, S. J. B. D. L. Buckley, and A. Horsman, "Tumour volume detection from MR images by morphological segmentation," *Physics in Medicine and Biology*, vol. 41, no. 11, pp. 2437–2446, 1996.

[54] S. Pohlman, K. A. Powell, N. A. Obuchowski, W. A. Chilcote, and S. G. Broniatowski, "Quantitative classification of breast tumors in digitized mammograms," *Medical Physics*, vol. 23, no. 8, pp. 1337–1345, 1996.

[55] Y. Tuduki, K. Murase, M. Izumida, H. Miki, K. Kikuchi, K. Murakami, and J. Ikezoe, "Automated seeded region growing algorithm for extraction of cerebral blood vessels from magnetic resonance angiographic data," in *IEEE International Conference on Engineering in Medicine and Biology Society*, 2000, pp. 1756–1759.

[56] Z. Pan and J. Lu, "A bayes-based region-growing algorithm for medical image segmentation," *Computing in Science and Engineering*, vol. 9, no. 4, pp. 32–38, 2007.

[57] M. del Fresno, M. Venere, and A. Clausse, "A combined region growing and deformable model method for extraction of closed surfaces in 3D CT and MRI scans," *Computerized Medical Imaging and Graphics*, vol. 33, no. 5, pp. 369–376, 2009.

[58] J. Yi and J. B. Ra, "A locally adaptive region growing algorithm for vascular segmentation," *International Journal of Imaging Systems and Technology*, vol. 13, no. 4, pp. 208–214, 2003.

[59] H. Sekiguchi, N. Sugimoto, S. Eiho, T. Hanakawa, and S. Urayama, "Blood vessel segmentation for head MRA using branch-based region growing," *Systems and Computers in Japan*, vol. 36, no. 5, pp. 80–88, 2005.

[60] J. K. Udupa and S. Samarasekera, "Fuzzy connectedness and object definition: Theory, algorithms and applications in image segmentation," *Graphical Models and Image Processing*, vol. 58, no. 3, pp. 246–261, 1996.

[61] S. Kobashi, Y. Hata, Y. Kitamura, and T. Yanagida, "A fuzzy rule-based region growing method for segmenting 3-D dynamic MR images," *Biomedical Soft Computing and Human Sciences*, vol. 6, no. 1, pp. 85–94, 2000.

[62] A. Abdel-Dayem and M. El-Sakka, "Carotid artery ultrasound image segmentation using fuzzy region growing," in *International Conference on Image Analysis and Recognition*, 2005, pp. 869–878.

[63] S. Beucher and F. Meyer, "The morphological approach of segmentation: the watershed transformation," in *Mathematical Morphology in Image Processing, Dougherty E. (ed.).* New York: Marcel Dekker, 1992, pp. 433–481.

[64] V. Grau, A. U. Mewes, M. Alcaniz, R. Kikinis, and W. S. K., "Improved watershed transform for medical image segmentation using prior information," *IEEE Transaction on Medical Imaging*, vol. 23, no. 4, pp. 447–458, 2004.

[65] L. Vincent and P. Soille, "Watersheds in digital spaces: An efficient algorithm based on immersion simulations," *IEEE Transactions on Pattern Analysis and Machine Intelligence*, vol. 13, no. 6, pp. 583–1598, 1991.

[66] A. R. Abdel-Dayem, M. R. El-Sakka, and A. Fenster, "Watershed segmentation for carotid artery ultrasound images," in *IEEE International Conference on Computer Systems and Applications*, 2005.

[67] S. Ding, J. Tu, C. Cheung, R. Beare, T. Phan, D. Reutens, and F. Thien, "Geometric model generation for CFD simulation of blood and air flows," in *International Conference on Bioinformatics and Biomedical Engineering*, 2007, pp. 1335–1338.

[68] J. C. Bezdek, L. O. Hall, and L. P. Clarke, "Review of MR image segmentation techniques using pattern recognition," *Medical Physics*, vol. 20, no. 4, pp. 1033–1048, 1993.

[69] G. Shakhnarovich, T. Darrell, and P. Indyk (eds.), *Nearest-Neighbor Methods in Learning and Vision: Theory and Practice.* MIT Press, 2006.

[70] J. Kim, M. Cetin, and A. S. Wilsky, "Nonparametric shape priors for active contour-based image segmentation," *Signal Processing*, vol. 87, no. 12, pp. 3021–3044, 2007.

[71] R. O. Duda, P. E. Hart, and D. G. Stork, *Pattern Classification (2nd edition).* Wiley-Interscience, John Wiley and Sons, 2000.

[72] M. W. Vannier, R. L. Butterfield, D. Jordan, W. A. Murphy, R. G. Levitt, and M. Gado, "Multispectral analysis of magnetic resonance images," *Radiology*, vol. 154, no. 1, pp. 221–224, 1985.

[73] T. Taxt and A. Lundervold, "Multispectral analysis of the brain using magnetic resonance imaging," *IEEE Transactions on Medical Imaging*, vol. 13, no. 3, pp. 470–481, 1994.

[74] W. M. Wells, W. E. L. Grimson, R. Kikinis, and F. A. Jolesz, "Adaptive segmentation of MRI data," *IEEE Transactions on Medical Imaging*, vol. 15, no. 4, pp. 429–442, 1996.

[75] T. Kapur, W. E. L. Grimson, and R. Kikinis, "Enhanced spatial priors for segmentation of magnetic resonance imagery," in *International Conference on Medical Image Computing and Computer-Assisted Intervention*, 1998, pp. 457–468.

[76] A. Zavaljevski, A. P. Dhawan, M. Gaskil, W. Ball, and J. D. Johnson, "Multi-level adaptive segmentation of multi-parameter MR brain images," *Computerized Medical Imaging and Graphics*, vol. 24, no. 2, pp. 87–98, 2000.

[77] J.-F. Aujol and T. F. Chan, "Combining geometrical and textured information to perform image classification," *Journal of Visual Communication and Image Representation*, vol. 17, no. 5, pp. 1004–1023, 2006.

[78] A. K. Jain and R. C. Dubes, *Algorithms for Clustering Data.* Englewood Cliffs, NJ: Prentice Hall, 1988.

[79] J. R. Jensen, *Introductory Digital Image Processing: A Remote Sensing Perspective (2nd edition).* Upper Saddle River, NJ: Prentice Hall, 1996.

[80] S. Ray and R. H. Turi, "Determination of number of clusters in k-means clustering and application in color image segmentation," in *International Conference on Advances in Pattern Recognition and Digital Techniques*, 1999, pp. 137–143.

[81] N. Memarsadeghi, D. M. Mount, N. S. Netanyahu, and J. L. Moigne, "A fast implementation of the isodata clustering algorithm," *International Journal of Computational Geometry and Applications*, vol. 17, no. 1, pp. 71–103, 2007.

[82] J. C. Bezdek, *Pattern Recognition with Fuzzy Objective Function Algorithms.* New York: Plenum, 1981.

[83] M. C. Clark, L. O. Hall, D. B. Goldgof, L. P. Clarke, R. P. Velthuizen, and M. S. Silbiger, "MRI segmentation using fuzzy clustering techniques," *Engineering in Medicine and Biology Magazine*, vol. 13, no. 5, pp. 730–742, 1994.

[84] S. Sahaphong and N. Hiransakolwong, "Unsupervised image segmentation using automated fuzzy c-means," in *IEEE International Conference on Computer and Information Technology*, 2007, pp. 690–694.

[85] Z. Liang, J. R. MacFall, and D. P. Harrington, "Parameter estimation and tissue segmentation from multispectral MR images," *IEEE Transactions on Medical Imaging*, vol. 13, no. 3, pp. 441–449, 1994.

[86] C. Carson, S. Belongie, H. Greenspan, and J. Malik, "Blobworld: Image segmentation using expectation-maximization and its application to image querying," *IEEE Transations on Pattern Analysis and Machine Intelligence*, vol. 24, no. 8, pp. 1026–1038, 2002.

[87] H. Lotfy, A. Elmaghraby, M. Kantardzic, and J. Hadizadeh, "Expectation-maximization framework for rock textures segmenta-

tion," in *IEEE International Workshop on Machine Learning for Signal Processing*, 2004, pp. 625–634.

[88] K. Held, E. R. Kops, B. J. Krause, W. M. Wells, R. Kikinis, and H. Muller-Gartner, "Markov random field segmentation of brain MR images," *IEEE Transactions on Medical Imaging*, vol. 16, no. 6, pp. 878–886, 1997.

[89] D. Swagatam, A. Abraham, and A. Konar, "Spatial information based image segmentation using a modified particle swarm optimization algorithm," in *International Conference on Intelligent Systems Design and Applications*, 2006, pp. 438–444.

[90] D. L. Pham, C. Xu, and J. L. Prince, "Current methods in medical image segmentation," *Annual Review of Biomedical Engineering*, vol. 2, pp. 315–337, 2000.

[91] J. S. Suri, S. Singh, and L. Reden, "Computer vision and pattern recognition techniques for 2-D and 3-D MR cerebral cortical segmentation (part i): A state-of-the-art review," *International Journal of Pattern Analysis and Applications*, vol. 5, no. 1, pp. 46–76, 2002.

[92] Z. Wu and R. Leahy, "An optimal graph theoretic approach to data clustering: Theory and its application to image segmentation," *IEEE Transations on Pattern Analysis and Machine Intelligence*, vol. 15, no. 11, pp. 1101–1113, 1993.

[93] N. Xu, N. Ahuja, and R. Bansal, "Object segmentation using graph cuts based active contours," *Computer Vision and Image Understanding*, vol. 107, no. 3, pp. 210–224, 2007.

[94] S. Wang and J. Siskind, "Image segmentation with ratio cut," *IEEE Transations on Pattern Analysis and Machine Intelligence*, vol. 25, no. 6, pp. 675–690, 2003.

[95] D. L. Collins, C. J. Holmes, T. M. Peters, and A. C. Evans, "Automatic 3-d model-based neuroanatomical segmentation," *Human Brain Mapping*, vol. 3, no. 3, pp. 190–208, 1995.

[96] D. V. Iosifescu, M. E. Shenton, S. K. Warfield, R. Kikinis, J. Dengler, F. A. Jolesz, and R. W. McCarley, "An automated registration algorithm for measuring MRI subcortical brain structures," *Neuroimage*, vol. 6, no. 1, pp. 13–25, 1997.

[97] O. Musse, F. Heitz, and J.-P. Armspach, "Fast deformable matching of 3D images over multiscale nested subspaces. application to atlas based MRI segmentation," *Pattern Recognition*, vol. 36, no. 8, pp. 1881–1899, 2003.

[98] P. Bondiau, G. Manlandain, S. Chanalet, P. Marcy, J. Habrand, F. Fauchon, P. Paquis, A. Courdi, O. Commowick, and I. Rutten, "Atlas-based automatic segmentation of MR images: Validation study on the brainstem in radiotherapy context," *International Journal of Radiation Oncology Biology Physics*, vol. 61, no. 1, pp. 289–298, 2005.

[99] X. Han and B. Fischl, "Atlas renormalization for improved brain mr image segmentatin across scanner platforms," *IEEE Transactions on Medical Imaging*, vol. 26, no. 4, pp. 479–486, 2007.

[100] G. E. Christensen, S. C. Joshi, and M. I. Miller, "Volumetric transformation of brain anatomy," *IEEE Transactions on Medical Imaging*, vol. 16, no. 6, pp. 864–877, 1997.

[101] S. Sandor and R. Leahy, "Surface-based labelling of cortical anatomy using a deformable atlas," *IEEE Transactions on Medical Imaging*, vol. 16, no. 1, pp. 41–54, 1997.

[102] F. L. Seixas, J. Damasceno, M. P. da Silva, A. S. de Souza, and D. C. M. Saade, "Automatic segmentation of brain structures based on anatomic

atlas," in *Inter. Conf. Intelligent Sys. Design and App.*, 2007, pp. 329–334.

[103] C. Xu and J. L. Prince, "Snakes, shapes, and gradient vector flow," *IEEE Transactions on Image Processing*, vol. 7, no. 3, pp. 359–369, 1998.

[104] T. McInerney and D. Terzopoulos, "Deformable models in medical image analysis: A survey," *Medical Image Analysis*, vol. 1, no. 2, pp. 91–108, 1996.

[105] C. Xu, D. L. Pham, and J. L. Prince, "Image segmentation using deformable models," in *Handbook of Medical Imaging*, M. Fitzpatrick and M. Sonka, Eds. SPIE Press, 2000, pp. 129–174.

[106] J. S. Suri, K. Liu, S. Singh, S. N. Laxminarayan, Z. Xiaolan, and L. Reden, "Shape recovery algorithms using level sets in 2-D/3-D medical imagery: A state-of-the-art review," *IEEE Transactions on Information Technology in Biomedicine*, vol. 6, no. 1, pp. 8–28, 2002.

[107] N. Paragios and R. Deriche, "Geodesic active regions and level set methods for supervised texture segmentation," *International Journal of Computer Vision*, vol. 46, no. 3, pp. 223–247, 2002.

[108] L. D. Cohen, "On active contour models and ballons," *Computer Vision Graphics and Image Processing: Image Understanding*, vol. 53, no. 2, pp. 211–218, 1991.

[109] L. D. Cohen and I. Cohen, "Finite-element methods for active contour models and ballons for 2-D and 3-D images," *IEEE Transations on Pattern Analysis and Machine Intelligence*, vol. 15, no. 11, pp. 1131–1147, 1993.

[110] T. McInerney and D. Terzopoulos, "T-snakes:topology adaptive snakes," *Medical Image Analysis*, vol. 4, no. 2, pp. 73–91, 2000.

[111] J. Pons and J. Boissonnat, "Topology-adaptive meshes based on the restricted delaunay triangulation," in *IEEE Conference on Computer Vision Pattern Recognition*, 2007, pp. 1–8.

[112] D. Adalsteinsson and J. Sethian, "A fast level set method for propagating interfaces," *Journal of Computational Physics*, vol. 118, pp. 269–277, 1995.

[113] K. Siddiqi, Y. Lauzire, A. Tannenbaum, and S. Zucker, "Area and length minimizing flows for shape segmentation," *IEEE Transactions on Image Processing*, vol. 7, no. 3, pp. 433–443, 1998.

[114] N. Paragios, O. Mellina-Gottardo, and V. Ramesh, "Gradient vector flow geometric active contours," *IEEE Transations on Pattern Analysis and Machine Intelligence*, vol. 26, no. 3, pp. 402–407, 2004.

[115] C. Li, J. Liu, and M. Fox, "Segmentation of edge preserving gradient vector flow: an approach toward automatically initializing and splitting of snakes," in *IEEE Conference on Computer Vision Pattern Recognition*, 2005, pp. 162–167.

[116] X. Xie and M. Mirmehdi, "MAC: Magnetostatic active contour model," *IEEE Transations on Pattern Analysis and Machine Intelligence*, vol. 30, no. 4, pp. 632–647, 2008.

[117] D. Cremers, M. Rousson, and R. Deriche, "A review of statistical approaches to level set segmentation: Integrating color, texture, motion and shape," *International Journal of Computer Vision*, vol. 72, no. 2, pp. 195–215, 2007.

[118] R. Kimmel, "Fast edge integration," in *Geometric Level Set Methods in Imaging, Vision, and Graphics*, 2003, pp. 59–77.

[119] X. Xie and M. Mirmehdi, "RAGS: Region-aided geometric snake," *IEEE Transactions on Image Processing*, vol. 13, no. 5, pp. 640–652, 2004.

[120] L. Vese and T. Chan, "A multiphase level set framework for image segmentation using the mumford and shah model," *International Journal of Computer Vision*, vol. 50, no. 3, pp. 271–293, 2002.

[121] D. Mumford and J. Shah, "Optimal approximations by piecewise smooth functions and associated variational problems," *Communications on Pure and Applied Mathematics*, vol. 42, no. 5, pp. 577–685, 1989.

[122] D. Gil and P. Radeva, "Curvature vector flow to assure convergent deformable models for shape modelling," in *Energy Minimization Methods in Computer Vision and Pattern Recognition*, 2003, pp. 357–372.

[123] A. Jalba, M. Wilkinson, and J. Roerdink, "CPM: A deformable model for shape recovery and segmentation based on charged particles," *IEEE Transations on Pattern Analysis and Machine Intelligence*, vol. 26, no. 10, pp. 1320–1335, 2004.

[124] R. Yang, M. Mirmehdi, and X. Xie, "A charged active contour based on electrostatics," in *Advanced Concepts for Intelligent Vision Systems*, 2006, pp. 173–184.

[125] H. K. Park and M. J. Chung, "External force of snake: virtual electric field," *Electronics Letters*, vol. 38, no. 24, pp. 1500–1502, 2002.

[126] G. Zhu, S. Zhang, Q. Zeng, and C. Wang, "Anisotropic virtual electric field for active contours," *Pattern Recognition Letters*, vol. 29, no. 11, pp. 1659–1666, 2008.

[127] X. Xie and M. Mirmehdi, "Magnetostatic field for the active contour model: A study in convergence," in *British Machine Vision Conference*, 2006, pp. 127–136.

[128] Y. Xiang, A. Chung, and J. Ye, "A new active contour method based on elastic interaction," in *IEEE Conference on Computer Vision Pattern Recognition*, 2005, pp. 452–457.

[129] J. P. Hirth and J. Lothe, *Theory of Dislocations.* John Wiley, 1982.

[130] L. D. Landau and E. M. Lifshitz, *Statistical Physics.* Pergamon Press, 1980.

[131] D. Adalsteinsson and J. Sethian, "The fast construction of extension velocities in level set methods," *Journal of Computational Physics*, vol. 148, pp. 2–22, 1998.

[132] A. Buades, B. Coll, and J. Morel, "A non-local algorithm for image denoising," in *IEEE Conference on Computer Vision Pattern Recognition*, 2005, pp. 60–65.

[133] J. Darbon, A. Cunha, T. Chan, S. Osher, and G. Jensen, "Fast nonlocal filtering applied to electron cryomicroscopy," in *IEEE Int. Symposium on Biomed. Imag.: From Nano to Macro*, 2008, pp. 1331–1334.

[134] P. Perona and J. Malik, "Scale space and edge detection using anisotropic diffusion," *IEEE Transations on Pattern Analysis and Machine Intelligence*, vol. 12, no. 7, pp. 629–639, 1990.

[135] C. Tomasi and R. Manduchi, "Bilateral filtering for gray and color images," in *IEEE Internaitonal Conference on Computer Vision*, 1998, pp. 839–846.

[136] W. E. Lorensen and H. E. Cline, "Marching cubes: A high resolution 3d surface construction algorithm," *Computer Graphics*, vol. 21, no. 4, pp. 163–169, 1987.

[137] W. Schroeder, K. Martin, and B. Lorensen, *The Visualization Toolkit An Object-Oriented Approach To 3D Graphics, 4th Edition.* Albany: Kitware Inc., 2005.

[138] J. Wang, Y. Guo, Y. Ying, Y. Liu, and Q. Peng, "Fast non-local algorithm for image denoising," in *IEEE Conference on Image Processing*, 2006, pp. 1429–1432.

[139] D. A. Steinman, "Image-based computational fluid dynamics modeling in realistic arterial geometries," *Annals of Biomedical Engineering*, vol. 30, no. 4, pp. 483–497, 2002.

[140] J. R. Cebral, M. Hernandez, and A. F. Frangi, "Computational analysis of blood flow dynamics in cerebral aneurysms from cta and 3d rotational angiography image data," in *International Congress on Computational Bioengineering*, 2003, pp. 191–198.

[141] C. A. Taylor and C. A. Figueroa, "Patient-specific modeling of cardiovascular mechanics," *Annual Review of Biomedical Engineering*, vol. 11, pp. 109–134, 2009.

[142] C. A. Taylor and D. A. Steinman, "Image-based modeling of blood flow and vessel wall dynamics: Applications, methods and future directions," *Annals of Biomedical Engineering*, 2010.

[143] S. Y. Yeo, X. Xie, I. Sazonov, and P. Nithiarasu, "Level set based automatic segmentation of human aorta," in *International Conference on Computational and Mathematical Biomedical Engineering*, 2009.

[144] I. Sazonov, S. Y. Yeo, R. Bevan, X. Xie, R. van Loon, and P. Nithiarasu, "Modelling pipeline for subject-specific arterial blood flow - a review,"

International Journal for Numerical Methods in Biomedical Engineering, in press, 2011.

[145] D. Mori and T. Yamaguchi, "Construction of the CFD model of the aortic arch based on mr images and simulation of the blood flow," in *International Workshop on Medical Imaging and Augmented Reality*, 2001, pp. 111–116.

[146] Y. Tokuda, M.-H. Song, Y. Ueda, A. Usui, A. Toshiaki, S. Yoneyama, and S. Maruyama, "Three-dimensional numerical simulation of blood flow in the aortic arch during cardiopulmonary bypass," *European Journal of Cardio-thoracic Surgery*, vol. 33, no. 2, pp. 164–167, 2008.

[147] K. C. Wang, R. W. Dutton, and C. A. Taylor, "Improving geometric model construction for blood flow modeling," *IEEE Engineering in Medicine and Biology Magazine*, vol. 18, no. 6, pp. 33–39, 1999.

[148] X. Y. Xu, Q. Long, M. W. Collins, M. Bourne, and T. M. Griffith, "Reconstruction of blood flow patterns in human arteries," *Proc Inst Mech Eng H, Journal of Engineering in Medicine*, vol. 213, no. 5, pp. 411–421, 1999.

[149] A. D. Augst, D. C. Barratt, A. D. Hughes, S. A. Thom, and X. Y. Xu, "Various issues relating to computational fluid dynamics simulations of carotid bifurcation flow based on models reconstructed from three-dimensional ultrasound images," *Proc Inst Mech Eng H, Journal of Engineering in Medicine*, vol. 217, no. 5, pp. 393–403, 2003.

[150] H. F. Younis, M. R. Kaazempur-Mofrad, R. C. Chan, A. G. Isasi, D. P. Hinton, A. H. Chau, L. A. Kim, and R. D. Kamm, "Hemodynamics and wall mechanics in human carotid bifurcation and its consequences for atherogenesis: investigation of inter-individual variation," *Biomechanics and Modeling in Mechanobiology*, vol. 3, no. 1, pp. 17–32, 2004.

[151] S. Giordana, S. J. Sherwin, J. Peiro, D. J. Doorly, Y. Papaharilaou, C. G. Caro, N. Watkins, N. Cheshire, M. Jackson, C. Bicknall, and V. Zervas, "Automated classification of peripheral distal by-pass geometries reconstructed from medical data," *Journal of Biomechanics*, vol. 38, no. 1, pp. 47–62, 2005.

[152] J. Peiro, S. J. Sherwin, and S. Giordana, "Automatic reconstruction of a patient-specific high-order surface representation and its application to mesh generation for CFD calculations," *Medical and Biological Engineering and Computing*, vol. 46, no. 11, pp. 1069–1083, 2008.

[153] H. M. Ladak, J. S. Milner, and D. A. Steinman, "Rapid three-dimensional segmentation of the carotid bifurcation from serial MR images," *Journal of Biomechanical Engineering*, vol. 122, no. 1, pp. 96–99, 2000.

[154] J. D. Gil, H. M. Ladak, D. A. Steinman, and A. Frenster, "Accuracy and variability assessment of a semiautomatic technique for segmentation of the carotid arteries from three-dimensional ultrasound images," *Medical Physics*, vol. 27, no. 6, pp. 1333–1342, 2000.

[155] D. A. Steinman, J. B. Thomas, H. M. Ladak, J. S. Milner, B. K. Rutt, and J. D. Spence, "Reconstruction of carotid bifurcation hemodynamics and wall thickness using computational fluid dynamics and mri," *Magnetic Resonance in Medicine*, vol. 47, no. 1, pp. 149–159, 2002.

[156] P. J. Yim, J. J. Cebral, R. Mullick, H. B. Marcos, and R. L. Choyke, "Vessel surface reconstruction with a tubular deformable model," *IEEE Transactions on Medical Imaging*, vol. 20, no. 12, pp. 1411–1421, 2001.

[157] J. R. Cebral, R. Lohner, O. Soto, P. L. Choyke, and P. J. Yim, "Patient-specific simulation of carotid artery stenting using computational fluid dynamics," in *International Conference on Medical Image Computing and Computer Assisted Intervention*, 2001, pp. 153–160.

[158] J. R. Cebral, M. A. Castro, R. Lohner, J. E. Burgess, R. Pergolizzi, and C. M. Putman, "Recent developments in patient-specific image-based modeling of hemodynamics," in *ENIEF04*, 2004.

[159] B. Nilsson and A. Heyden, "A fast algorithm for level set-like active contours," *Pattern Recognition Letters*, vol. 24, no. 9, pp. 1311–1337, 2003.

[160] L. Antiga, Ene-Iordache, and A. B. Remuzzi, "Computational geometry for patient-specific reconstruction and meshing of blood vessels from MR and CT angiography," *IEEE Transactions on Medical Imaging*, vol. 22, no. 5, pp. 674–684, 2003.

[161] T. Deschamps, P. Schwartz, D. Trebotich, P. Colella, D. Saloner, and R. Malladi, "Vessel segmentation and blood flow simulation using level-sets and embedded boundary methods," in *Computer Assisted Radiology and Surgery*, 2004, pp. 75–80.

[162] J. Svensson, R. Gardhagen, E. Heiberg, T. Ebbers, D. Loyd, T. Lanne, and M. Karlsson, "Feasibility of patient specific aortic blood flow CFD simulation," in *International Conference on Medical Image Computing and Computer Assisted Intervention*, 2006, pp. 257–263.

[163] L. Antiga, M. Piccinelli, L. Botti, B. Ene-Iordache, A. Remuzzi, and D. A. Steinman, "An image-based modeling framework for patient-specific computational hemodynamics," *Medical and Biological Engineering and Computing*, vol. 46, no. 11, pp. 1097–1112, 2008.

[164] A. Enquobahrie, L. Ibanez, E. Bullitt, and S. Aylward, "Vessel enhancing diffusion filter," *The Insight Journal*, 2007.

[165] A. F. Frangi, W. J. Niessen, K. L. Vincken, and M. A. Viergever, "Multiscale vessel enhancement filtering," in *International Conference on*

Medical Image Computing and Computer-Assisted Intervention, 1998, pp. 130–137.

[166] L. Ibanez, W. Schroeder, L. Ng, and J. Cates, *The ITK Software Guide, 2nd Edition.* Kitware, Inc., 2005.

[167] R. Deriche, "Using canny's criteria to derive a recursively implemented optimal edge detector," *International Journal of Computer Vision*, vol. 1, no. 2, pp. 167–187, 1987.

[168] M. Petrou and J. Kittler, "Optimal edge detectors for ramp edges," *IEEE Transations on Pattern Analysis and Machine Intelligence*, vol. 13, no. 5, pp. 483–491, 1991.

[169] S. Y. Yeo, X. Xie, I. Sazonov, and P. Nithiarasu, "Geometrically induced force interaction for three-dimensional deformable models," *IEEE Transactions on Image Processing*, vol. 20, no. 5, pp. 1373–1387, 2011.

[170] T. F. Cootes, C. J. Taylor, D. H. Cooper, and J. Graham, "Active shape models-their training and application," *Computer Vision and Image Understanding*, vol. 61, no. 1, pp. 38–59, 1995.

[171] M. Leventon, W. Grimson, and O. Faugeras, "Statistical shape influence in geodesic active contours," in *IEEE Conference on Computer Vision Pattern Recognition*, vol. 1, 2005, pp. 316–323.

[172] M. Rousson and N. Paragios, "Shape priors for level set representations," in *European Conference on Computer Vision*, 2002, pp. 78–92.

[173] D. Cremers, S. Osher, and S. Soatto, "Kernel density estimation and intrinsic alignment for shape priors in level set segmentation," *International Journal of Computer Vision*, vol. 69, no. 3, pp. 335–351, 2006.

[174] A. Tsai, A. Yezzi, W. Wells, C. Tempany, D. Tucker, A. Fan, W. E. Grimson, and A. Willsky, "Model-based curve evolution technique for image segmentation," in *IEEE Conference on Computer Vision Pattern Recognition*, vol. 1, 2001, pp. 463–468.

[175] Y. Chen, H. D. Tagare, S. Thiruvenkadam, F. Huang, D. Wilson, R. W. Briggs, and E. A. Geiser, "Using prior shapes in geometric active contours in a variational framework," *International Journal of Computer Vision*, vol. 50, no. 3, pp. 315–328, 2002.

[176] S. Chen and R. Radke, "Level set segmentation with both shape and intensity priors," in *IEEE Internaitonal Conference on Computer Vision*, 2009, pp. 763–770.

[177] S. Y. Yeo, X. Xie, I. Sazonov, and P. Nithiarasu, "Geometric potential force for the deformable model," in *British Machine Vision Conference*, 2009.

[178] S. Dambreville, Y. Rathi, and A. Tannenbaum, "A framework for image segmentation using shape models and kernel space shape priors," *IEEE Transactions on Pattern Analysis and Machine Intelligence*, vol. 30, no. 8, pp. 1385–1399, 2008.

[179] S. Y. Yeo, X. Xie, I. Sazonov, and P. Nithiarasu, "Variational level set segmentation using shape prior," in *International Conference on Mathematical and Computational Biomedical Engineering*, 2011.